

CAPITAL UNIVERSITY OF SCIENCE AND
TECHNOLOGY, ISLAMABAD



**Cavity Prediction and
Multi-variable Control of
Underground Coal Gasification
Process**

by

Syed Bilal Javed

A thesis submitted in partial fulfillment for the
degree of Doctor of Philosophy

in the

Faculty of Engineering

Department of Electrical Engineering

2021

Cavity Prediction and Multi-variable Control of Underground Coal Gasification

By

Syed Bilal Javed

(DEE153001)

Dr. Muhammad Faisal Aftab, Associate Professor

Agder University (UiA), Norway

(Foreign Evaluator 1)

Dr. Rini Akmeliawati, Associate Professor

The University of Adelaide, Australia

(Foreign Evaluator 2)

Dr. Raza Samar

(Thesis Supervisor)

Dr. Ali Arshad

(Thesis Co-supervisor)

Dr. Noor Muhammad Khan

(Head, Department of Electrical Engineering)

Dr. Imtiaz Ahmad Taj

(Dean, Faculty of Engineering)

DEPARTMENT OF ELECTRICAL ENGINEERING
CAPITAL UNIVERSITY OF SCIENCE AND TECHNOLOGY
ISLAMABAD

2021

Copyright © 2021 by Syed Bilal Javed

All rights reserved. No part of this thesis may be reproduced, distributed, or transmitted in any form or by any means, including photocopying, recording, or other electronic or mechanical methods, by any information storage and retrieval system without the prior written permission of the author.

Dedicated to My Homeland



**CAPITAL UNIVERSITY OF SCIENCE & TECHNOLOGY
ISLAMABAD**

Expressway, Kahuta Road, Zone-V, Islamabad
Phone: +92-51-111-555-666 Fax: +92-51-4486705
Email: info@cust.edu.pk Website: <https://www.cust.edu.pk>

CERTIFICATE OF APPROVAL

This is to certify that the research work presented in the thesis, entitled “**Cavity Prediction and Multi-variable Control of Underground Coal Gasification Process**” was conducted under the supervision of **Dr. Raza Samar**. No part of this thesis has been submitted anywhere else for any other degree. This thesis is submitted to the **Department of Electrical Engineering, Capital University of Science and Technology** in partial fulfillment of the requirements for the degree of Doctor in Philosophy in the field of **Electrical Engineering**. The open defence of the thesis was conducted on **May 28, 2021**.

Student Name :

Syed Bilal Javed (DEE-153001)

The Examination Committee unanimously agrees to award PhD degree in the mentioned field.

Examination Committee :

- (a) External Examiner 1: Dr. Abdul Khaliq,
Professor
Sir Syed CASE IT, Islamabad
- (b) External Examiner 2: Dr. Iftikhar Ahmed Rana,
Associate Professor
SEECs, NUST, Islamabad
- (c) Internal Examiner : Dr. Fazal ur Rehman
Professor
CUST, Islamabad

Supervisor Name :

Dr. Raza Samar
Professor
CUST, Islamabad

Name of HoD :

Dr. Noor Muhammad Khan
Professor
CUST, Islamabad

Name of Dean :

Dr. Imtiaz Ahmad Taj
Professor
CUST, Islamabad

AUTHOR'S DECLARATION

I, **Syed Bilal Javed (Registration No. DEE-153001)**, hereby state that my PhD thesis titled, '**Cavity Prediction and Multi-variable Control of Underground Coal Gasification Process**' is my own work and has not been submitted previously by me for taking any degree from Capital University of Science and Technology, Islamabad or anywhere else in the country/ world.

At any time, if my statement is found to be incorrect even after my graduation, the University has the right to withdraw my PhD Degree.



(**Syed Bilal Javed**)

Dated: May, 2021

Registration No : DEE-153001

PLAGIARISM UNDERTAKING

I solemnly declare that research work presented in the thesis titled “**Cavity Prediction and Multi-variable Control of Underground Coal Gasification Process**” is solely my research work with no significant contribution from any other person. Small contribution/ help wherever taken has been duly acknowledged and that complete thesis has been written by me.

I understand the zero tolerance policy of the HEC and Capital University of Science and Technology towards plagiarism. Therefore, I as an author of the above titled thesis declare that no portion of my thesis has been plagiarized and any material used as reference is properly referred/ cited.

I undertake that if I am found guilty of any formal plagiarism in the above titled thesis even after award of PhD Degree, the University reserves the right to withdraw/ revoke my PhD degree and that HEC and the University have the right to publish my name on the HEC/ University Website on which names of students are placed who submitted plagiarized thesis.



(Syed Bilal Javed)

Dated: May, 2021

Registration No : DEE-153001

List of Publications

It is certified that following publication(s) have been made out of the research work that has been carried out for this thesis:-

1. **S. B. Javed**, A. A. Uppal, A. I. Bhatti, and R. Samar, “Prediction and parametric analysis of cavity growth for the underground coal gasification project Thar,” *Energy*, vol. 172, pp. 1277–1290, Apr. 2019.
2. **S. B. Javed**, A. A. Uppal, R. Samar, and A. I. Bhatti, “Design and implementation of multi-variable H_∞ robust control for the underground coal gasification project Thar,” *Energy*, vol. 216, p. 119000, Feb. 2021.
3. **S. B. Javed**, V. I. Utkin, A. A. Uppal, R. Samar, and A. I. Bhatti, “Data-Driven Modeling and Design of Multivariable Dynamic Sliding Mode Control for the Underground Coal Gasification Project Thar,” *IEEE Transactions on Control Systems Technology*, pp. 1–13, 2021.

(Syed Bilal Javed)

Registration No: DEE153001

Acknowledgement

In the name of Allah, The Most Beneficent, The Most Merciful. First and foremost, I would like to express gratitude to Allah SWT, the Almighty God for the blessing, kindness, and inspiration in lending me to pursue my doctoral studies. I also extend my deepest greetings to the Holy Prophet Muhammad (PBUH), the last messenger of Allah SWT, whose life is the perfect model for all humans and whose teachings are the source of guidance in all disciplines of life.

I am indebted to all of my teachers whose teachings have brought me to this stage. Certainly its a pleasant obligation to thank my supervisor Prof. Dr. Raza Samar for his valuable guidance, strong encouragement, and kind support towards my study and research. I have not only learned from his insight, deep technical knowledge, and practical experience, but a lot of things from him as a person as well. It has been a real honor for me to work under his supervision and to attend his lectures and talks. I also like to express my gratitude to my co-supervisor Dr. Ali Arshad Uppal whose keen observance and directives helped me to develop and enhance my skills and complete my research work in time. I am particularly grateful to Prof. Vadim Ivanovich Utkin for his kind supervision, which enabled me to develop a multi-variable nonlinear robust control system for the Underground coal gasification Project Thar (UPT). I would specially like to thank Prof. Dr. Amer Iqbal Bhatti for his valuable guidance, strong encouragement and kind support towards my research and study. I am grateful to my office colleagues and friends whose valuable company always kept me focused and motivated. Especially, I recognize the valuable support from Mr. Khuram Shehzad, Mr. Noman Riaz, and Dr. Rizwan Azam.

I also acknowledge intimate support of my parents throughout my educational career. Their prayers, moral and financial support always kept me motivated towards my goal. I also appreciate my spouse and children for their cooperation, love, support and providing stress free atmosphere during my doctorate's tenure. Moreover, I am thankful to my siblings for their constant support and encouragement throughout my graduate studies.

Last but not least, I would like to thank the Lawrence Livermore National Laboratory (LLNL), USA, for providing the cavity simulation model (CAVSIM), the UPT team and control and signal processing research (CASPR) group at Capital University of Science and Technology, Islamabad for providing the technical assistance, and the support provided by the international research support initiative program (IRSIP), HEC, Pakistan and the Ohio State University (OSU), OH, USA.

(Syed Bilal Javed)

Abstract

Underground coal gasification (UCG) is a promising clean coal technology to convert unmineable and deep coal reserves into syngas, which can be used in many industrial applications. The planning commission of Pakistan has initiated UCG Project Thar (UPT) in Block V of Thar coal fields located in Sindh. In a UCG field, real time monitoring of the hydrological and geological conditions like water influx rate, cavity growth and its interaction with overburden is a challenging task. Similarly, the development of a control system for a UCG field is also a formidable task due to numerous challenges, such as lack of instrumentation, installation of sensors at different locations, underground disturbances, process nonlinearities, and lack of direct control over the process parameters. This research work deals with the cavity prediction and the design of a multi-variable control system for the UCG field.

For this purpose, a 3D axisymmetric cavity simulation model (CAVSIM) is parameterized with operating conditions of UPT and properties of Lignite B coal of Thar coal fields. For model validation, a comparison has been made between simulated and the UPT field data for the composition and heating value of syngas. The results of CAVSIM are also compared with our previous ID packed bed model, which show the superiority of CAVSIM model. Moreover, a comprehensive simulation study has been carried out to predict the cavity growth and its interaction with overburden. The effect of operating parameters of UPT on volumetric cavity growth and heating value of syngas are also investigated.

The proposed research work highlights the significance of a model-based multi-variable control system for the UCG field in general, and particularly for the UPT field. However, the CAVSIM can not be employed directly to design the model-based control system due to its its complex and multidimensional dynamics. Thus, a simple multi-variable linear model is identified by employing the subspace-based system identification (N4SID) technique. The linear model is then employed to design the multi-variable linear and nonlinear robust control techniques. In the linear approach, an H_∞ controller is designed using the S/KS method. The control

problem is formulated by using the standard approach. Moreover, the nonlinear robust control is designed by employing the sliding mode control (SMC) technique. The regular form of the linear model is formulated to design the conventional SMC and dynamic sliding mode control (DSMC). The stability of zero dynamics is shown on the approximate model of the CAVSIM. The designed controllers are implemented on the CAVSIM, and the simulation results of both the linear and nonlinear robust control techniques have been compared. It is observed that each controller has achieved the robust stability and performance in the presence of modeling inaccuracies and external disturbance. However, the performance of H_∞ deteriorates when operated outside the operating range of the linear model. While the chattering is prominent for the SMC, whereas in case of DSMC the chattering is significantly reduced due to continuous control inputs. The DSMC has also consumed lesser control energy as compared to the SMC to achieve the desired objectives.

Contents

| | |
|---|--------------|
| Author’s Declaration | v |
| Plagiarism Undertaking | vi |
| List of Publications | vii |
| Acknowledgement | viii |
| Abstract | x |
| List of Figures | xvi |
| List of Tables | xviii |
| Abbreviations | xix |
| Symbols | xxi |
| 1 Introduction | 1 |
| 1.1 Background | 1 |
| 1.2 Underground Coal Gasification | 3 |
| 1.2.1 Design Constraints in UCG | 4 |
| 1.2.2 Performance of UCG | 5 |
| 1.3 UCG Developments Worldwide | 6 |
| 1.3.1 Significance of UCG from Pakistan’s Perspective | 6 |
| 1.3.2 Challenges at the UPT Field | 9 |
| 1.4 Research Objectives | 10 |
| 1.5 Research Scope | 11 |
| 1.6 Thesis Contributions | 12 |
| 1.6.1 Cavity Prediction and Parametric Study | 12 |
| 1.6.2 Design of the Multi-variable Robust Control for the UPT Gasifier | 13 |
| 1.7 Thesis Outline | 14 |

| | | |
|----------|--|-----------|
| 2 | Literature Review | 16 |
| 2.1 | Modeling Approaches for UCG | 17 |
| 2.1.1 | Packed Bed Models | 17 |
| 2.1.2 | Coal Block Models | 19 |
| 2.1.3 | Channel Models | 20 |
| 2.1.4 | Resource Recovery Models | 22 |
| 2.2 | Control of UCG Process | 24 |
| 2.2.1 | Related Work | 25 |
| 2.3 | Gap Analysis | 27 |
| 2.4 | Selection of Model for the UPT Field | 28 |
| 2.5 | Problem Statement | 31 |
| 2.6 | Summary | 31 |
| 3 | Mathematical Model of the UPT Gasifier | 33 |
| 3.1 | Model Description | 34 |
| 3.1.1 | Water Influx Submodel | 35 |
| 3.1.2 | Flow Submodel | 36 |
| 3.1.3 | Wall Submodel | 37 |
| 3.1.4 | Roof Rubble Submodel | 39 |
| 3.1.5 | Outflow Channel Submodel | 39 |
| 3.1.6 | Cavity Growth Module | 40 |
| 3.2 | Experimental Setup | 41 |
| 3.3 | Model Validation | 43 |
| 3.3.1 | Model Parametrization | 43 |
| 3.3.2 | Results Comparison | 43 |
| 3.4 | Model Predictions | 46 |
| 3.5 | Effect of Operating Conditions on Cavity Growth | 52 |
| 3.5.1 | Effect of Inlet Gas Composition | 52 |
| 3.5.2 | Effect of Varying O ₂ Concentration | 53 |
| 3.5.3 | Effect of Varying α | 54 |
| 3.5.4 | Effect of Varying Inlet Gas Flow Rate | 57 |
| 3.6 | Summary | 57 |
| 4 | Development of Multi-variable Linear Model for the UPT Gasifier | 59 |
| 4.1 | General Work-flow of System Identification | 60 |
| 4.1.1 | Preliminary Identification Experiments | 61 |
| 4.1.1.1 | Free-run Experiment | 61 |
| 4.1.1.2 | Staircase Experiment | 61 |
| 4.1.1.3 | White Noise Experiment | 62 |
| 4.1.2 | Design of Identification Experiment | 62 |
| 4.1.3 | Model Estimation | 63 |
| 4.1.3.1 | Data Pre-processing | 63 |
| 4.1.3.2 | Determining Model Structure and Order | 64 |
| 4.1.4 | Model Validation | 64 |

| | | |
|----------|---|------------|
| 4.2 | System Identification for the UPT Field | 64 |
| 4.3 | Analysis of Linear Model | 75 |
| 4.3.1 | Plant Scaling | 76 |
| 4.3.2 | Interaction Analysis | 77 |
| 4.3.2.1 | Condition Number | 77 |
| 4.3.2.2 | Relative Gain Array (RGA) | 77 |
| 4.3.3 | Model Uncertainty | 79 |
| 4.4 | Summary | 81 |
| 5 | Design of Multi-variable H_∞ Controller for the UPT Gasifier | 83 |
| 5.1 | Introduction | 84 |
| 5.1.1 | Mixed-sensitivity H_∞ Synthesis | 85 |
| 5.2 | Problem Formulation | 86 |
| 5.3 | Design of H_∞ Controller for the UPT Field | 87 |
| 5.3.1 | Robust Stability and Performance Constraints | 91 |
| 5.3.2 | Selection of Weights | 92 |
| 5.4 | Results and Discussion | 94 |
| 5.5 | Implementation of Controller on the CAVSIM | 99 |
| 5.6 | Summary | 102 |
| 6 | Design of Multi-variable Sliding Mode Controllers for the UPT Gasifier | 104 |
| 6.1 | Introduction | 105 |
| 6.1.1 | SMC Design Procedure | 106 |
| 6.1.1.1 | Switching Surface Design | 106 |
| 6.1.1.2 | Existence of Sliding Mode | 107 |
| 6.1.2 | Chattering Problem | 108 |
| 6.2 | Sliding Mode Control Design for the UPT Field | 108 |
| 6.2.1 | Formulation of Regular Form | 109 |
| 6.2.2 | Design of Conventional SMC | 111 |
| 6.2.3 | Design of DSMC | 112 |
| 6.3 | Approximate Model of CAVSIM | 114 |
| 6.3.1 | Model Equations | 114 |
| 6.3.1.1 | Solid Phase Mass Balance | 115 |
| 6.3.1.2 | Solid Phase Energy Balance | 115 |
| 6.3.1.3 | Gas Phase Mass Balance | 116 |
| 6.3.1.4 | Gas Phase Energy and Momentum Balance | 116 |
| 6.3.1.5 | Chemical Kinetics | 117 |
| 6.3.1.6 | Outputs Equations | 118 |
| 6.3.2 | Stability of Zero Dynamics of CAVSIM | 120 |
| 6.4 | Implementation of SMC Controllers on the CAVSIM | 123 |
| 6.4.1 | SMC Implementation | 123 |
| 6.4.2 | DSMC Implementation | 124 |

| | | |
|----------|---|------------|
| 6.5 | Results and Discussions | 126 |
| 6.6 | Summary | 130 |
| 7 | Conclusion and Future Work | 131 |
| 7.1 | Conclusion | 131 |
| 7.1.1 | Cavity Prediction and Parametric Study | 131 |
| 7.1.2 | Development of a Control-oriented Model | 132 |
| 7.1.3 | Design of the Multi-variable Robust Control for the UPT Gasifier | 133 |
| 7.2 | Future Work | 134 |
| 7.2.1 | Improvements in Field Trials | 134 |
| 7.2.2 | Improved Model-based Control Design for the UPT Gasifier | 135 |
| 7.2.2.1 | Formulation of First Principle UPT Model | 135 |
| 7.2.2.2 | Parameter Estimation | 135 |
| 7.2.2.3 | Implementation at the UCG Field | 136 |
| | Bibliography | 137 |

List of Figures

| | | |
|------|--|----|
| 1.1 | World's electricity generation by fuel type in 2018 | 4 |
| 1.2 | Pakistan's electricity generation by fuel type as of June 2019 | 8 |
| 3.1 | Solution routine of CAVSIM | 40 |
| 3.2 | Process schematic diagram | 41 |
| 3.3 | Field area of the UPT | 42 |
| 3.4 | Flow rate of injected air | 45 |
| 3.5 | Model validation: (a-c) Molar Fraction of Syngas Species with Time, (d) heating value of syngas | 45 |
| 3.6 | Cavity shapes at various stages of UCG | 47 |
| 3.7 | Flow rate of injected air | 49 |
| 3.8 | Molar ratio of (a) produced char and (b) CO + H ₂ per mole of injected O ₂ | 50 |
| 3.9 | (a) Water influx rate, (b) produced species rate, (c) composition of product gas, (d) heating value of product gas | 51 |
| 3.10 | Effect of inlet gas composition | 53 |
| 3.11 | Effect of varying O ₂ concentration | 54 |
| 3.12 | Effect of varying α | 55 |
| 3.13 | Effect of varying α | 56 |
| 3.14 | Effect of varying inlet gas flow rate | 57 |
| 4.1 | Typical work-flow of system identification technique | 60 |
| 4.2 | UCG response for staircase inputs | 67 |
| 4.3 | Step response of UCG | 68 |
| 4.4 | Designed PRBS signals | 70 |
| 4.5 | Hankel singular value plots for the selection of models order | 71 |
| 4.6 | Comparison of linear and nonlinear models using simulation error method | 73 |
| 4.7 | Comparison of linear and nonlinear models using residual analysis | 74 |
| 4.8 | Frequency response of condition number | 78 |
| 4.9 | Frequency response of RGA | 79 |
| 4.10 | Step responses with uncertainty bounds | 80 |
| 4.11 | Frequency responses with uncertainty bounds | 81 |
| 5.1 | Standard control configuration without uncertainty for controller (a) synthesis and (b) analysis | 85 |

| | | |
|------|---|-----|
| 5.2 | Block diagram of the closed-loop system with performance specifications | 88 |
| 5.3 | General configuration for controller synthesis | 88 |
| 5.4 | General configurations for controller analysis | 89 |
| 5.5 | Inverse of performance weight | 95 |
| 5.6 | Frequency response of closed-loop system | 95 |
| 5.7 | Robust stability | 97 |
| 5.8 | Nominal performance | 98 |
| 5.9 | Robust performance analysis | 98 |
| 5.10 | Closed-loop transient response of scaled-linear system | 99 |
| 5.11 | Closed-loop response to input disturbance | 99 |
| 5.12 | Controller implementation scheme | 100 |
| 5.13 | Closed-loop response of nonlinear model to the reference inputs . . | 101 |
| 5.14 | Close-loop response of nonlinear model to the input disturbance . . | 101 |
| 6.1 | Block Diagram of closed-loop UCG system with DSMC | 113 |
| 6.2 | Input disturbance with time | 127 |
| 6.3 | Outputs of the closed-loop system with time | 128 |
| 6.4 | Control efforts with time | 128 |
| 6.5 | Tracking errors during closed-loop operation | 129 |
| 6.6 | Sliding manifolds for DSMC | 129 |

List of Tables

| | | |
|-----|--|-----|
| 1.1 | World's energy consumption by fuel type in 2018 | 2 |
| 1.2 | Major UCG projects launched in the 21 st century | 7 |
| 2.1 | Types of UCG models | 18 |
| 2.2 | Some important features of the reported UCG models | 24 |
| 2.3 | Control techniques for UCG | 27 |
| 3.1 | Chemical kinetics for cavity growth | 35 |
| 3.2 | Parameters used in simulation | 44 |
| 3.3 | Relative error for field and predictions of models | 46 |
| 3.4 | Composition of Injected gas | 53 |
| 3.5 | Injected gas composition (effect of O ₂ concentration) | 54 |
| 3.6 | Composition of Injected gases (effect of α) | 55 |
| 3.7 | Composition of Injected gases (effect of α) | 56 |
| 4.1 | Parameters obtained from step response | 66 |
| 4.2 | Design parameters for PRBS | 69 |
| 4.3 | Parameters obtained from transient and frequency responses of the estimated model | 81 |
| 5.1 | Robust stability margins for H_∞ controllers. | 97 |
| 5.2 | Robust performance margins for H_∞ controllers | 97 |
| 6.1 | Chemical reactions considered in the model | 118 |
| 6.2 | Performance comparison of the SMCs | 129 |

Abbreviations

| | |
|---------------|--|
| 1D | One-dimensional |
| 2D | Two-dimensional |
| 3D | Three-dimensional |
| CAVSIM | Cavity simulation model |
| CCTs | Clean coal technologies |
| CRIP | Controlled retracting injection point |
| CCS | CO ₂ capture and storage |
| CFD | Computational fluid dynamic |
| DSMC | Dynamic sliding mode control |
| IEA | International Energy Agency |
| IGCC | Integrated gasification combined cycle |
| LLNL | Lawrence Livermore National Laboratory |
| mtoe | Million tonnes of oil equivalent |
| MIMO | Multiple-input, multiple-output |
| N4SID | Numerical algorithms for subspace state space system identification |
| NS | Nominal stability |
| NP | Nominal performance |
| PDEs | Partial differential equations |
| PEM | Prediction error method |
| PLCs | Programmable logic controllers |
| PRBS | Pseudo random binary sequence |
| RCL | Reverse combustion linking |

| | |
|-----------------|--|
| RLNG | Regasified liquefied natural gas |
| RGA | Relative gain array |
| RS | Robust stability |
| RP | Robust performance |
| SMC | Sliding mode control |
| SMCs | Sliding mode controllers |
| UCG | Underground coal gasification |
| UPT | Underground coal gasification Project Thar |
| UCGSIM3D | 3D UCG simulator |

Symbols

| | |
|------------------------|---|
| A | Pre-exponential rate constant ($1/s$) |
| c_T | Total gas concentration (mol/m^3) |
| c_{eq} | Equilibrium gas concentration (mol/m^3) |
| C_s, C_g | Specific heat capacity for solid ($J/kg.K$) and gas ($J/mol.K$) |
| c_{c_r} | Carbon conversion rate (kg/s) |
| D_u | Scaling matrix of control inputs, |
| D_{d_i}, D_e | Scaling matrices of input disturbances and tracking errors |
| dp | Average particle diameter (m) |
| \mathbf{d}_i | Vector of scaled input disturbances |
| $\tilde{\mathbf{d}}_i$ | Vector of unscaled input disturbances |
| \mathbf{e} | Vector of scaled tracking errors |
| $\tilde{\mathbf{e}}$ | Vector of unscaled tracking errors |
| \mathbf{e}_Y | Vector of weighted tracking errors |
| \mathbf{e}_U | Vector of weighted control inputs |
| E | Activation energy for rate constant (J/mol) |
| $F_{H_2O(l)}$ | Volumetric flux of water (m/s) |
| F_{inj}, F_p | Flux of Injected and produced gases ($mol/m^2.s$) |
| F_c, F_{ch} | Carbon and char flux ($kg/m^2.s$) |
| ΔG^o | Standard free energy change (kJ/mol) |
| G | Scaled linear model of the UPT |
| \tilde{G} | Unscaled linear model of the UPT |
| G_{Π} | Perturbed plants |
| \hat{h} | Surface height (m) |

| | |
|--|--|
| ΔH° | Standard free enthalpy change (KJ/mol) |
| h_{r_i} | Heat of reactions (J) |
| HV_e | Experimental heating value of syngas (KJ/m^3) |
| H_i, m_{i_e} | Heat of combustion (KJ/m^3) and experimental molar fraction percentage of syngas component i |
| k_r | Reaction rate constant ($1/s$) |
| K | Designed controller |
| KS | Control sensitivity transfer function |
| m_{O_2}, m_p | Molar fraction of O_2 and produced gas (unitless) |
| M_c, M_g | Molecular weight of carbon and produced gas (kg/mol) |
| n^r | Number of bits in PRBS sequence |
| N_s | Length of PRBS sequence (samples) |
| P_o | Pressure of inlet gas (Pa) |
| p | Number of inputs |
| Pr | Prandtl no. (unitless) |
| \tilde{P} | Generalized plant |
| $\hat{Q}_{ox}, \hat{Q}_{dry}, \hat{Q}_{gf}$ | Heat flux (W/m^2) in oxidation, drying and gasification zones |
| $\hat{Q}_{H_2O(l)}, \hat{Q}_p, \hat{Q}_{ch}$ | Heat flux (W/m^2) of water influx, produced gas and char |
| R | Universal gas constant ($J/mol.K$) |
| \mathbf{r} | Vector of desired trajectories in a scaled form |
| $\tilde{\mathbf{r}}$ | Vector of desired trajectories in an unscaled form |
| r_0 | Location of cavity boundary or channel wall (m) |
| r_c | Cavity radius (m) |
| S | Sensitivity function |
| S_i, S_o | Input and output sensitivity function |
| T_o, T_w | Temperature of inlet gas and wall (K) |
| T_f, T_v, T_e | Temperature of failure, vaporization, and extinction conditions (K) |
| T^* | Wall heat transfer temperature (K) |
| T | Complementary sensitivity function |
| t | Time (s) |

| | |
|-------------------------|--|
| t_R | Rise time (s) |
| T_{sw} | Switching time (s) |
| t_s | Sampling time (s) |
| t_d | Delay time (s) |
| \mathbf{u}_c | Vector of continuous control inputs |
| \mathbf{u}_d | Vector of discontinuous control inputs |
| u_i | Control inputs, $i = 1, 2$ |
| \mathbf{u} | Vector of scaled control inputs |
| $\tilde{\mathbf{u}}$ | Vector of unscaled control inputs |
| v_w | Wall recession velocity (m/s) |
| v | Sensed outputs |
| $W_c, W_a, W_{H_2O(l)}$ | Mass fraction of carbon, ash, and water (unitless) |
| W_P | Performance weight function |
| W_U | Control inputs weight function |
| W_Δ | Multiplicative weight of input perturbation |
| w | Exogenous inputs |
| \mathbf{x} | Vector of system states |
| y_i | Outputs, $i = 1, 2$ |
| y_{ij} | Outputs ($i = 1, 2$) with respect to the corresponding inputs ($j = 1, 2$) |
| \mathbf{y} | Vector of scaled outputs |
| $\tilde{\mathbf{y}}$ | Vector of unscaled outputs |
| z_c | Cavity height (m) |
| z | Exogenous outputs |
| Υ | Hydraulic conductivity (m/s) |
| Ω | Gas injection source term |
| ψ | Function describing location of permeable ash pile surface |
| χ, χ_g | Viscosity of solid ($kg/m.s$) and gas ($mol/m.s$) |
| ρ_c | Density of carbon (kg/m^3) |
| ζ_i | Constants which are depending upon the local Reynolds number |

| | |
|-------------------------------------|--|
| ϑ | Heat transfer coefficient ($W/m^2.K$) |
| α | Steam to oxygen ratio |
| κ_a | Permeability (m^2) |
| δ | Wall layer thickness (m) |
| λ_g | Thermal conductivity ($W/m.K$) |
| ω | Angular frequency (rad/s) |
| ω_l | Lower cut-off frequency (rad/s) |
| ω_H | Higher cut-off frequency (rad/s) |
| ξ | Closed-loop response parameter |
| β | Settling-time parameter |
| τ | Time constant (s) |
| τ_l | Lowest time constant (s) |
| τ_H | Highest time constant (s) |
| γ | Condition number |
| $\bar{\sigma}$ | Maximum singular value |
| $\underline{\sigma}$ | Minimum singular value |
| Δ | Complex perturbation |
| μ | Structured singular value |
| τ_c, τ_g | Time constants of control valve and gas analyzer (s) |
| τ_{d_c}, τ_{d_g} | Time delays of control valve and gas analyzer (s) |
| $sign$ | Signum function |
| ε | Vector of conventional sliding surfaces |
| φ | Vector of dynamic sliding surfaces |
| 1D Packed bed model symbols: | |
| $a_{s_{2,1}}$ | Stoichiometric coefficient of char in coal pyrolysis reaction |
| $a_{i,j}$ | Stoichiometric coefficient of gas i in reaction j |
| B | A constant depending on the coal bed porosity and thermal conductivity of coal and char ($cal/cm/s/K$) |
| c_{p_i} | Heat capacity ($cal/g/K$), $i = 1$ for coal and $i = 2$ for char |
| C_7 | Distribution of O_2 concentration (mol/cm^3) along x |
| h | Heat transfer coefficient ($cal/s/K/cm^3$) |

| | |
|------------|---|
| H_i | Heat of combustion (kJ/m^3) of gas, $i = 1, 3, 5, 8$ represents CO, H ₂ , CH ₄ and tar |
| k_y | Mass transfer coefficient ($mol/cm^3/s$) |
| L | Length of the reactor ($2500cm$) |
| M_1, M_2 | Molecular weight for coal and char (g/mol) |
| $P,$ | Pressure of gases (atm) |
| q_i | Heat of reaction i (cal/mol) |
| R_i | Rate of a chemical reaction ($mol/cm^3/s$), $i = 1, 2, 3$ represents pyrolysis, char oxidation and steam gasification, respectively |
| T_o, T_s | Gas and solid temperature (K) |
| v_g | Velocity (cm/s) of gases |
| x_o | Variable of length (cm) |
| ρ_i | Solid density (g/cm^3), $i = 1, 2$ for coal and char |

Chapter 1

Introduction

1.1 Background

Coal is the most affordable and ubiquitous fossil fuel and continues to play a vital role in power generation and industrial sectors like cement, iron and steel and chemicals sub-sectors [1–3]. The share of coal in industrial energy use is increased by 8% over the last two decades [2]. It is reported by International Energy Agency (IEA) that the world’s energy consumption for the year 2018 is almost 14314 million tonnes of oil equivalent (mtoe) [2, 3]. The share of various fuel sources in the world’s energy mixture is shown in Table 1.1. Fossil fuels currently account for almost 81% of the world’s energy consumption in which the contribution of coal is almost 27% [3]. The combustion of fossil fuels has detrimental impacts on the environment, such as greenhouse gas emissions, global warming and air pollution. Owing to the environmental concerns related to fossil fuels, the contribution of renewable energy sources is growing rapidly in the world energy mixture [3]. However, renewable energy sources will not be able to completely replace the fossil fuels in foreseeable future due to the growing global energy demand [1].

According to the IEA, global electricity demand would rise by 2.1 percent per annum by 2040 [3]. The contribution of coal in electricity generation is the highest

TABLE 1.1: World's energy consumption by fuel type in 2018 [3]

| | Fuel type | Share (mtoe) | Share (% of total) |
|-------------|------------------|---------------------|---------------------------|
| Fossil fuel | Oil | 4501 | 31.44 |
| | Coal | 3821 | 26.7 |
| | Natural gas | 3273 | 22.8 |
| Others | Hydro | 361 | 2.5 |
| | Modern bioenergy | 737 | 5.15 |
| | Other Renewables | 293 | 2.04 |
| | Nuclear | 709 | 4.95 |
| | Solid biomass | 620 | 4.33 |

(38%) amongst all the fuel sources, as shown in Fig. 1.1. The share of coal in the electricity supply has increased significantly after the advent of integrated gasification combined cycle (IGCC) technology [1, 4]. The major advantages of coal over its counterparts like crude oil and natural gas are its low cost and relative abundance [5]. The total coal reserves of the world are approximately 1055 billion tonnes [6]. Clean coal technologies (CCTs) are opted to address the environmental concerns related to coal combustion, and utilize the coal resources in a more effective way to meet the future energy requirements [1, 4]. The CCTs are also employed to generate electricity at a large scale, like IGCC in which coal is gasified under pressure [7].

Coal gasification is a clean coal technology, and it is broadly classified as surface gasification and underground coal gasification (UCG). In surface gasification, coal is mined, refined and then gasified in a specially designed chamber [1, 8]. The surface gasification technologies include entrained flow, fluidized and moving beds. The major disparities among these techniques are related to the size of the coal particles, ash handling, gas flow configuration and process operating conditions [9]. UCG is the process in which hydrocarbon materials are converted into syngas in-situ and this technology has been evolving for the last century [10]. The lack of

direct control over the process parameters of UCG, results in a lower quality syngas as compared to the surface gasifier. However, the UCG has various advantages over surface gasification techniques, such as reduction in greenhouse gas emissions and dust pollution. It also eliminates the coal mining and ash handling, which increases the workers' safety and health [11]. Moreover, UCG is the only feasible option for the unmineable, deeply located and low-rank coal reserves [12, 13].

1.2 Underground Coal Gasification

UCG is a promising clean coal technology to convert unmineable and deep coal reserves into syngas [8, 12–14]. The syngas can be burnt to produce electricity, heat and also used in the manufacturing of chemicals such as ammonia and fertilizer [15]. The major attributes of the UCG are: to utilize unmineable coal reserves, production of syngas at a competitive and low cost, efficient carbon capture handling and the elimination of safety and health hazards of conventional coal mining[1]. UCG is a highly complex process and requires the enriched knowledge of multi-disciplinary fields, such as drilling, exploration, hydrology, mechanical geology, mass and heat transport phenomena, chemical kinetics and thermodynamics [16].

In the simplest form of UCG, two wells (injection and production) are drilled from the surface to the coal seam. Then a permeable channel is created to link both the wells. A number of linking techniques have been reported in the literature, such as forward combustion linking, reverse combustion linking (RCL), hydraulic-fracturing, electro-linking, in-seam linking, explosive fracture, two-stage UCG, long and large tunnel gasification and controlled retracting injection point (CRIP) [17, 18]. Once a permeable link is developed, the coal gasification process begins by injecting a suitable oxidant like air or a mixture of steam and oxygen at the high flow rate and pressure into the inlet well. However, before the gasification process, the coal seam is ignited to set the initial temperature of the UCG reactor, which is crucial for the successful operation of the UCG field.

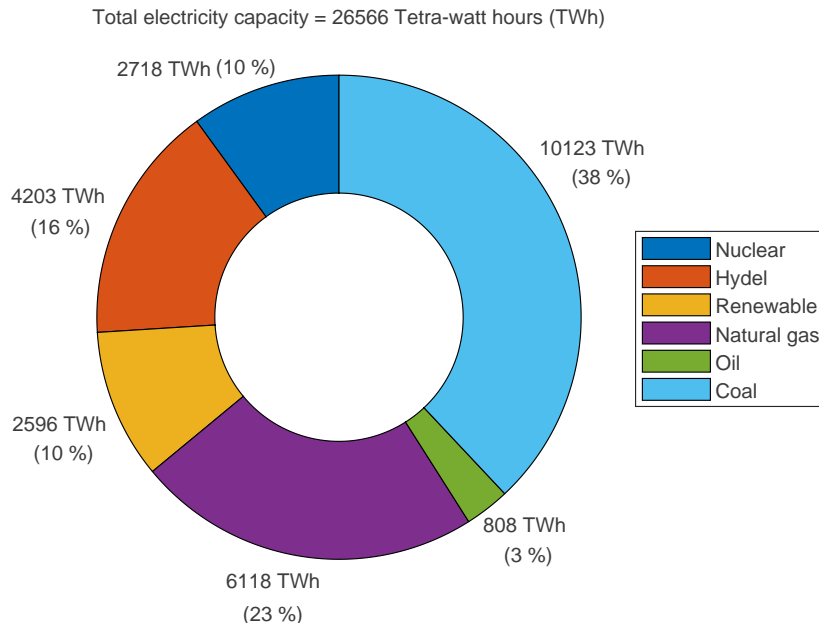


FIGURE 1.1: World's electricity generation by fuel type in 2018 [3]

In the gasification process, a bulk of coal consumes and produces combustible gas mixtures. The raw dry gas is collected at the outlet well, and it mainly consists of CO , H_2 , CO_2 . While a small amount of CH_4 , higher hydrocarbons, traces of tars and pollutants are also present. The important chemical reactions that take place during coal gasification are drying, pyrolysis, combustion and gasification. These chemical reactions have different activation energies, hence requiring a certain temperature to occur. The cavity begins to evolve as the gasification process proceeds, and water influx into the cavity from the surrounding aquifers. This water contributes in the gasification reactions and also affects the temperature of the UCG reactor. After the completion of the process, the cavity is flushed with steam and/or water to eradicate pollutants [1, 9].

1.2.1 Design Constraints in UCG

The design of a UCG process is a challenging task, as it occurs in-situ and lacks direct control over the process parameters like reactor size, heat and mass losses, coal steam and coal feed rates. There are numerous design constraints involved in the designing of a successful UCG setup. The major challenges are the selection of a UCG site, drilling and linking of inlet and outlet wells, prevention of injection

and production wells failure from spalling of overburden rock and reduction in the detrimental impacts on the environment. Moreover, the control of water influx from the aquifers, selection of inlet gas composition, flow rate and temperature, minimization of excessive gas and heat losses and assurance of a relatively constant gas quality are the important factors to be considered in a UCG design [9, 19].

Over the years, several UCG designs have been developed to address the aforesaid issues. The important UCG designs include linked vertical wells, CRIP and steeply dipping coal seams. These designs mainly differ in the drilling method, placement and linking techniques of the process wells [9].

1.2.2 Performance of UCG

The cavity growth is an important phenomenon in the UCG process, as it directly affects the critical economic and environmental factors involved in the success of the process [9, 13, 15, 20]. The prediction of size, shape and growth rate of the cavity are important aspects to determine the resource recovery and the post-burn subsidence behavior of the overburden strata [21–23]. This analysis mainly includes the selection of inlet and outlet well positions for the next gasification cycle. It also provides information about the spalling of overburden and water influx from surrounding aquifers. The cavity size depends on the coal combustion rate, while the flow pattern of heat, gas and mass inside the cavity affects its shape. Thus, the monitoring of cavity growth is essential to determine the overall performance of a UCG site.

In power plant applications, the energy output per unit time is an important performance metric to quantify the performance of a UCG site, which depends on the heating value and the mass flow rate of syngas [24, 25]. Hence, a multi-variable control system is required to achieve the desired performance of the UCG site. The composition and flow rate of syngas varies widely with the composition and flow rate of oxidant, coal bed properties, the behavior of surrounding strata and the hydrological conditions [9, 19]. Moreover, the composition and flow rate of injected gas are the only tuning knobs to control the process parameters.

1.3 UCG Developments Worldwide

Presently, global warming, greenhouse gas emissions and air pollution are the most important environmental concerns for the entire world. The coal contribution in the emission of CO₂ and other greenhouse gases is largest amongst all the fossil fuels [3]. Despite the current environmental challenges, the world is relying on coal and employing CCTs to meet its energy demands [1, 26–28]. Table 1.2 shows the number of UCG-based industrial scale projects, which are developed in the 21st century worldwide. It can be observed that UCG has become a potential process worldwide to utilize the unmineable coal reserves with the advent of IGCC and carbon capture and storage (CCS) technologies.

Since the beginning of the 21st century, most of the recent developments in UCG technology have emanated from Europe, Australia, Canada and South Africa. USA revived its UCG program in the year 2000 due to the increasing and more variable gas prices. This program is primarily based on the research work conducted in the Lawrence Livermore National Laboratory (LLNL), USA from 1960-1980. Now the UCG technology is rapidly growing in various countries of Asia, particularly in China. Around 15 UCG trials have been conducted in China and ENN, a Chinese company is working in collaboration with Australia, USA, Uzbekistan, EU and South African energy companies with an objective to utilize the UCG syngas in the chemical industry. In India, several UCG projects have been launched at a commercial scale in dedicated coal blocks. Pakistan has also started a UCG project in the Thar coal field aiming to build a UCG based power plant.

1.3.1 Significance of UCG from Pakistan’s Perspective

Despite being blessed by enormous energy resources, Pakistan has faced a severe energy crisis during the years 2008-17, . All the economic sectors of the country were badly affected directly and indirectly by this energy crisis. The massive power plants were incorporated during the years 2013-18 and added a cumulative capacity

TABLE 1.2: Major UCG projects launched in the 21st century [27, 29, 30]

| Countries | Year | Organization | Objectives |
|--------------|------|--|--|
| South Africa | 2017 | Eskom (also Africary) | Power Generation |
| Europe | 2016 | Tops | Coupled UCG - CO ₂ capture and storage (CCS) Site Characterization and risk |
| China | 2011 | UCG Research Centers (Beijing) Seamwell, ENN Group, China Energy Conservation and Environmental Protection Corporation Zhengzhou Coal Industry Co., Ltd. | Power Generation H_2 for fuel cells. |
| Canada | 2011 | Swan Hills Synfuels LP | Clean and competitive power generation. |
| Pakistan | 2009 | Thar Coal & Energy Board | Power Generation |
| Australia | 2007 | Linc Energy company | UCG-IGCC Power Generation, UCG-CCS |
| Poland | 2007 | Central Mining Institute of Poland | Safety and environmental concerns of UCG process |
| U.S.A. | 2005 | LLNL Linc Energy, Carbon Energy and Ergo | Energy natural gas liquefaction, development of 3D simulator to predict cavity growth simulators |
| India | 2005 | Neyvell Lignite Corporation Limited Central Mine Planning and Design Institute Limited Central Coalfields Ltd., Western Coalfields Ltd. | Power Generation Study and evaluate the calorific value of the gas generated |

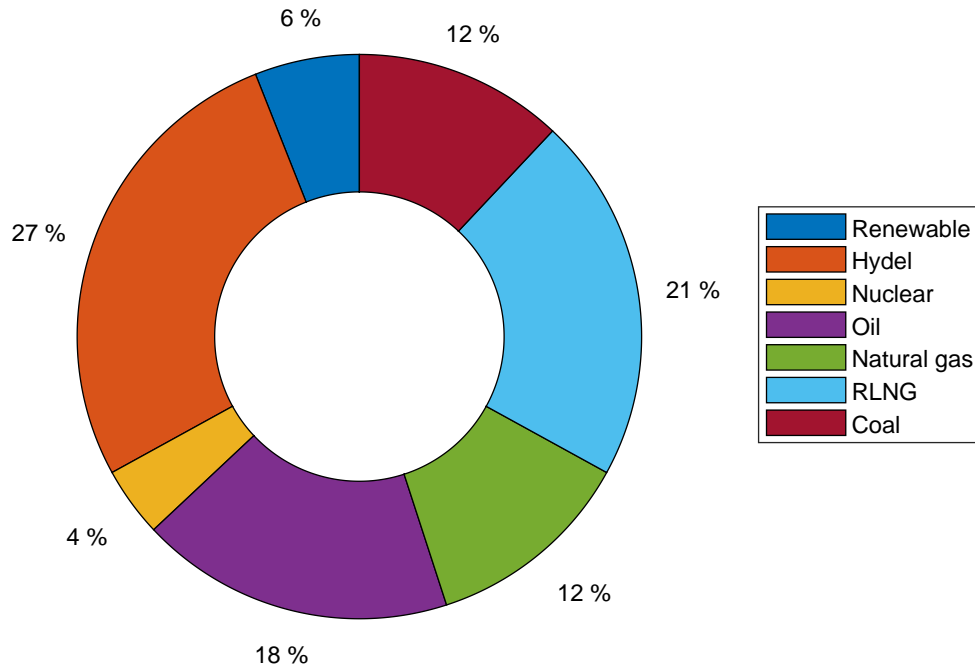


FIGURE 1.2: Pakistan's electricity generation by fuel type as of June 2019 [33]

of 12,230 MW in the national grid, which significantly reduced the energy demand and supply gap [31]. Although the energy crisis has been resolved to some extent, but the price of electricity has been increased and will also rise in the future, as a result of such aggressive capacity additions.

The share of various fuel sources in the electricity generation capacity of Pakistan is shown in Fig. 1.2. The contribution of fossil fuels is the highest (63%) [31] amongst all the fuel sources. Natural gas is a local product and its resources are quickly depleting with the increase in its demand. Pakistan spends billions of USD every year to import most of the crude oil and regasified liquefied natural gas (RLNG) for fulfilling its energy demands. The consumption and local production of crude oil is widening, therefore, its import will further increase in the future. According to [32], the oil and gas reserves of Pakistan will be depleted in the next 13 and 16 years, respectively [32].

The overall coal reserves in Pakistan are almost 185.17 billion tonnes [5], of which

175 billion tonnes of Lignite B coal deposits are located in Thar desert [34]. In spite of large coal reserves, Pakistan has not used this fuel resource effectively in electricity production. Thar coal reserves can be utilized to produce 20,000MW of electricity for the next 40 years [5]. The UCG is a viable option for the Thar coal deposits due to the low-rank nature of coal, variation in coal seam thickness and depths, loose formation and geological positioning of the aquifers [19]. The calorific value of Thar coal is less than 12 MJ/kg and the volatile matter is greater than 20%, which also favors the gasification of coal in-situ [35]. Moreover, the contamination of potable water aquifer is not possible at the UPT site due to its geological conditions, which is a major environmental concern related to any UCG site [1, 13]. In Thar coal block-V, two aquifers are present above the coal seam and one is underneath the coal seams. According to the Litho-log of a wellbore, these aquifers lie at an average depth of 55 – 59m, 105 – 109m and 195 – 250m, respectively. The depth and thickness of the coal seam range from 122m to 180m and 0.3m to 42m, respectively [36, 37]. The dug wells are being used to meet the drinking water requirements of the local community, which relies on the first aquifer. The potable water aquifer cannot be contaminated in the UPT field area, as it is 100m above the area of the UCG reactor. The quality of second and third water aquifers is not suitable for drinking and the risk of contamination is eliminated by adopting the controlled operational practices during the test burn [38].

The planning commission of Pakistan has started the R&D-based UCG Project Thar (UPT) in Block V of Thar coal field [34]. The fundamental objective of the project is to develop a UCG based power plant to produce 100 MW of electricity at a low cost. This project has a huge significance to utilize the coal deposits and to address the energy crisis of Pakistan.

1.3.2 Challenges at the UPT Field

UCG has many potential benefits over the existing coal gasification techniques, and many research studies have been carried out on the UCG process. However, it has not been able to commercialize at a large scale as surface gasification due to

the lack of real time monitoring and control of the process [1, 15, 19, 27]. The real time monitoring of a UCG process parameters is a formidable task due to the complex geological conditions, water influx from surrounding strata, high temperature and humidity. Like other UCG fields, UPT has the necessary instrumentation to measure the process parameters like composition, flow rate, pressure and temperature of injected and product gases. But it lacks a real time monitoring system to measure the hydrological and geological conditions, such as water influx rate, cavity growth and its interaction with overburden. In [13], based on various UCG field trials reports of the USA, it has been reported that there is not a single method which can provide complete details about the real time evolution of the cavity.

For any UCG site, the development of a control system is a challenging task due to numerous challenges like lack of instrumentation, installation of sensors at different locations, underground disturbances, process nonlinearities, limited tuning knobs and limited access to the process parameters. The composition and flow rate of inlet gas are the only tuning knobs to develop the closed-loop control system for UCG.

1.4 Research Objectives

As described above, a plethora of challenges are involved in the monitoring and development of a control system for a UCG site, in general, and particularly for the UPT field. Hence, the prime objectives of this research work are to:

- Predict the cavity growth, its interaction with overburden and water influx for the UPT field.
- Develop an approximate control-oriented model to design a model-based control system.
- Design multi-variable linear and nonlinear robust control techniques to maintain the heating value and flow rate of syngas at their desired levels.

- Implement the designed controllers on the actual high fidelity nonlinear model.

1.5 Research Scope

The scope of this study is to perform cavity prediction and devise a multi-variable control system for the field-scale UCG setup. For any UCG site, the real time monitoring of cavity growth is a formidable task. The prediction of multidimensional phenomena of cavity growth is essential for the necessary technical, environmental, and economic feasibility analysis [13]. The energy output per unit time is an important performance metric of a UCG gasifier, which is a function of the heating value and flow rate of syngas [25]. Hence, the cavity prediction and the development of a multi-variable closed-loop system are essential to achieve the desired performance of a UCG gasifier.

A comprehensive UCG process model and a simulation environment to investigate the important phenomena occurring in-situ are required to achieve the desired research objectives. The overall methodology employed in this study is depicted below:

1. The model selection has paramount importance to achieve the desired research objectives. A trade-off is involved in the prediction capabilities of the model and the ease in control design. The model is selected by performing a comprehensive literature review about the modeling and control strategies for the UCG field.
2. Subsequently, the model is parameterized with the Lignite B coal bed properties and operating conditions of the UPT field. The operating parameters mainly include composition, flow rate, temperature and pressure of injected gas. The model is validated with the UPT field data by comparing the composition and heating value of syngas.

3. The model selected in step 1 is not suitable to design a model-based control law due to its complexity. Therefore, a linear multi-variable model for the UPT field is developed by employing the N4SID system identification technique. The identified model is used to design the linear and nonlinear multi-variable robust controllers for the UPT field.

1.6 Thesis Contributions

The major contributions of this thesis are the prediction and parametric study of the cavity growth, and the development of a multi-variable robust closed-loop system for the UPT field. The following individual contributions lead to these objectives.

1.6.1 Cavity Prediction and Parametric Study

- a) The UCG process model is parameterized with the operation parameters of the UPT field and properties of Lignite B coal of Thar coal fields.
- b) The model has been validated with the UPT field data and used for the prediction of essential process parameters like water influx, cavity growth and its interaction with the overburden strata.
- c) Finally, the effect of various operating parameters of the UPT field on the cavity growth and the calorific value of the syngas have been investigated.

The contribution stated above has resulted in the following journal publication:

- **S. B. Javed**, A. A. Uppal, A. I. Bhatti, and R. Samar, “Prediction and parametric analysis of cavity growth for the underground coal gasification project Thar,” *Energy*, vol. 172, pp. 1277–1290, Apr. 2019.

1.6.2 Design of the Multi-variable Robust Control for the UPT Gasifier

- a) A simple control-oriented, multi-variable model is developed by employing the subspace-based (N4SID) system identification technique.
- b) The identified linear model is employed to design the model-based multi-variable robust controllers. The S/KS method is used to design the H_∞ controller and a standard control configuration is used to formulate the problem.
- c) The multi-variable nonlinear controllers are also designed using SMC technique. A conventional SMC has been designed by formulating the regular form of the linear model. To mitigate the chattering phenomena in the conventional SMC, a dynamic sliding mode control (DSMC) has been designed to obtain smooth and continuous control signals.
- d) The designed controllers are implemented on the actual nonlinear model. The performance and the robustness of each controller has been shown in the presence of modeling inaccuracies and external disturbance.

The aforementioned contribution has lead to the following research publications:

- **S. B. Javed**, A. A. Uppal, R. Samar, and A. I. Bhatti, “Design and implementation of multi-variable H_∞ robust control for the underground coal gasification project Thar,” *Energy*, vol. 216, p. 119000, Feb. 2021.
- **S. B. Javed**, V. I. Utkin, A. A. Uppal, R. Samar, and A. I. Bhatti, “Data-Driven Modeling and Design of Multivariable Dynamic Sliding Mode Control for the Underground Coal Gasification Project Thar,” *IEEE Transactions on Control Systems Technology*, pp. 1–13, 2021.

1.7 Thesis Outline

The rest of the thesis is organized in the following manner.

- Chapter 2 accounts for the literature review related to mathematical modeling and control techniques for the UCG process. A comprehensive literature survey has been carried out on the modeling approaches of the UCG process. The intent of the literature review is to select a suitable model for the prediction of cavity growth and its interaction with overburden. The challenges involved in the control design of a UCG field, in general, and specifically for the UPT is discussed. Moreover, earlier studies carried out in this area are also presented. It has been observed that there is a trade-off between the model prediction capabilities and the ease in control design. Based on the gap analysis, the problem statement has been formulated.
- In Chapter 3, the model has been described in detail. The model is parameterized and validated with the experimental data of the UPT field. After model validation, it is used to predict various process phenomena like cavity growth and its interaction with overburden, water influx and produced gas species flow rates. The parametric study is also performed to investigate the effect of operating parameters on the cavity growth and the heating value of syngas.
- Chapter 4 is dedicated to explain the formulation of a control oriented, multi-variable linear model for the UPT field. The model has been identified by using the system identification technique, which mainly relies on the input-output data. An identification experiment has been designed to estimate the model and the estimation data is generated by the CAVSIM. The model validation methods are discussed which are followed by the analysis of the linear model.
- In Chapter 5, the identified model is employed to design a multi-variable H_∞ controller using the S/KS mixed sensitivity method. The robust stability

and performance of the designed controller have been shown in the presence of input disturbance and uncertainties. Finally, the H_∞ controller is implemented on the CAVSIM. The simulation results show that the closed-loop system achieves the desired control objectives.

- Chapter 6 presents the design of a model-based multi-variable nonlinear control system for the UPT field. The regular form of the linear model is formulated to design the SMC and the DSMC. Moreover, the boundedness of zero dynamics has been proved by an approximated one-dimensional (1D) model of the CAVSIM. The designed controllers are implemented on the CAVSIM. The simulation results are shown and a comparison is made between the performance and robustness of the linear and nonlinear robust controllers.
- Finally, the conclusive remarks about the thesis and the future recommendations are presented in Chapter 7.

Chapter 2

Literature Review

UCG is one of the clean coal technologies, generally applicable for low-grade, deep and un-mineable coal reserves. The UPT has been launched in Block V of Thar coal field, located in Sindh, by the planning commission of Pakistan [34]. The main objective of the UPT project is to produce electricity at a low cost by developing a UCG based power plant. The essential technical, environmental and economic feasibility analysis of any UCG field is based on the prediction of cavity growth and it requires a comprehensive UCG model [9, 13, 15, 20, 39, 40]. Moreover, in industrial applications like IGCC, energy output per unit time is an important performance metric to determine the potential of a UCG for electricity production [24, 25]. The development of a closed-loop system to achieve the desired energy output per unit time has paramount importance in improving the performance of a UCG site. Hence, the literature survey aims to explore the details of work done in both the areas i.e., the modeling approaches and the control techniques for the UCG process.

The chapter begins with the literature review of UCG models in section 2.1. The related work of existing control design techniques for the UCG process is discussed in section 2.2. The gap analysis is presented in section 2.3, followed by the selection of model in section 2.4. The research problem has been formulated in section 2.5, and finally the chapter is summarized in section 2.6.

2.1 Modeling Approaches for UCG

Despite the conduction of various UCG field trials worldwide, limited information about the UCG process is available [9, 41, 42]. The monitoring and controlling of all essential operating parameters of the UCG process are formidable tasks [41]. Moreover, The conduction of field trials are highly expensive and time consuming. Several laboratory-scale trials have been performed on various coal blocks to describe the process details [14, 39, 43–45]. However, the laboratory-scale experiments are not sufficient to reflect the actual UCG field [13]. Thus, the limitations involved in the conduction of UCG field trials, real time data acquisition and controlling of the UCG process lead to the development of quantitative UCG models to investigate various aspects of the process.

The modeling of a UCG process must incorporate various physical and chemical phenomena, such as chemical reactions, water influx, spalling, geo-mechanical responses, heat and mass transfer, cavity growth and its interaction with overburden, and hydrology. The development of a comprehensive UCG model to describe all these physical processes is a challenging task. Thus, most of the UCG models have been developed to investigate the various aspects of the process separately by employing simplifying assumptions. Over the years, various types of UCG models have been developed and they are mainly classified into packed bed models, coal block models, channel models, and resource recovery models [9, 15, 41]. Table 2.1 presents the key objectives and the typical formulation of each type of UCG model and the detailed discussion is given as follows.

2.1.1 Packed Bed Models

Initially, the UCG models are developed by considering the process as a packed bed reactor with uniform particle size. A permeable link is created between the injection and production wells by RCL or by using chemical explosives or pressurized air which causes fractures in coal seam. The appropriate gases are injected

TABLE 2.1: Types of UCG models [46]

| Type | Key objectives | Typical formulation |
|-------------------|--|-------------------------------|
| Packed bed | Modeling of packed bed gasifier and interpretation of experimental results | 1D packed bed; time dependent |
| Coal block | Modeling the gasification process in terms of coal blocks and validation of laboratory-scale experiments | 1D block; time dependent |
| Channel | Estimation of the composition and amount of syngas | 1D channel; steady-state |
| Resource recovery | Prediction of the amount of consumed coal, flow rate and quality of syngas | 2D/3D; time dependent |

to ignite and then gasify the permeable zone. This modeling approach is used for medium and low-rank coals like sub-bituminous and lignite have higher permeability. These coal seams can be gasified by creating a permeable channel between the inlet and outlet wells rather than establishing any physical channel.

In [47], authors have proposed a linear 1D model for the forward combustion of UCG process. The optimum operating conditions are determined such as flow rate, air/steam ratio and preheating of injected air. The model has been validated with the field data of Wyoming near Hanna. Thorsness et al. [48, 49] have proposed a 1D packed bed model in which heat and mass transport phenomena, transient Darcy flow and reaction chemistry with suitable reaction rates are considered. The product gas composition and reaction front propagation rate are determined against the process operating parameters and coal bed properties. The model results show a good match with the experimental data obtained from a packed bed combustion tube. In [50], Winslow has developed a time dependent computational model in which multi-dimensional simulations can be performed. The simulation results are in good agreement with the experimental data of Wyoming sub-bituminous coal. In [51], authors have proposed a two-dimensional (2D) general packed bed model to study the various aspects of the process occurring at

the wall of cavity. The partial differential equations (PDEs) are used to formulate energy, mass and momentum conservation laws. The simulations are performed to investigate the behavior of UCG reactor for various physical conditions like a regression of wall during gasification, wall drying, and water influx inside the UCG gasifier. Abdel Hadi and Hsu [52] have developed a 2D computational model for the multi-dimensional simulations of a fixed bed UCG. The model has been used to predict coal consumption, gas composition, temperature and pressure both in space and time.

In [53], Khadse et al. have used the model of [49] to develop a 1D pseudo transient model. The composition and temperature profiles for the solid and gas phases are simulated for different operating parameters. The simulations are performed for two various coal types and the results are in a good match with the literature. Uppal et al. [54] have developed a 1D packed bed model for the UPT field, which is based on the model of [49]. The heating value and composition of syngas are found as a function of coal bed properties and various operating parameters. The results of the solved model are compared with the field data of UPT. The authors have improved the parameter estimation in [55], by formulating a relatively large scale optimization problem. Moreover, the supertwisting SMC algorithm is implemented to obtain the desired heating value of product gas.

The packed bed models are suitable to represent the UCG process at a laboratory-scale, but not feasible for the field-scale UCG process. Most of the work is based on 1D geometry and ignores some important phenomena, such as water influx from the surrounding aquifer, cavity evolution and its interaction with overburden.

2.1.2 Coal Block Models

In coal block models, a semi-infinite coal block is dried and gasified. In this modeling technique, coal seam can be considered either wet or dry slab of coal having low permeability than packed bed models. The coal slab is categorized into various regions due to slow heating rate of the UCG process, such as ash

layer, gas film, and wet and dry coal regions. The process is depicted by the movement of these regions normal to the flow of injected blast gas. In [56], the coal block modeling approach is initially used, in which a cylindrical shaped sub-bituminous coal block is considered. The heat and mass transfer, locations of drying and pyrolysis fronts, concentration and temperature of various volatiles are investigated in different regions of the coal block. Massaquoi and Riggs [57, 58] have extended Tsang's 1D model, in which simultaneous drying and combustion of a wet coal slab are considered. The model results for the position and temperature of flame, combustion rate and temperature of coal surface have been validated with the experimental data.

In [59], Park and Edgar have extended the work of [57, 58], and proposed an unsteady state 1D coal block model. The model is capable to predict the lateral cavity growth and drying front. The simulation results have been compared with the experimental results of Texas lignites. In [60], Perkins and Sahajwalla have extended Tsang's study and proposed a 1D model, which includes random pore and multi-component diffusion model to consider the disparity of reaction rates with conversion. The model is used for the prediction of cavity growth, location of drying front and temperature profile of the coal block. In [61], authors have enhanced their work by incorporating water influx and ash layer. The effect of coal bed properties and operating parameters on the cavity growth are investigated.

Mostly, the earlier described coal block models are developed under atmospheric conditions. While these conditions vary considerably in UCG field trials, for instance, the pressure is much larger than the atmospheric pressure. Similar to the packed bed models, coal block models also ignore the cavity evolution due to thermo-mechanical failure.

2.1.3 Channel Models

In channel models, a physical link is created between the inlet and outlet wells to permit the gas flow through the coal seam. This modeling method is feasible

for high-rank coal seams which have low permeability. A cylindrical geometry is assumed for the coal seam, while the cavity is considered as a rectangular or cylindrical channel growing within the coal seam. Moreover, the channel diameter can be kept variable or constant and all the heterogeneous reactions occur on the surface of cavity walls.

Magnani and Farouq Ali [62] have proposed a 1D, steady state model for the UCG process. The model comprises five coupled differential equations, solved analytically to develop closed-form expressions for the significant parameters of gasification process. The process sensitivity to the input variables is evaluated by using the proposed model. In [63, 64], 2D models have been developed, which are based on the 1D model of [62]. The model in [63] is used to investigate the impact of process variables on the net heat recovery of the UCG process. In the model of Pasha and Ali [64], an unsteady state flow of gases is assumed, and the model is used to show the change in diameter of the channel in a time domain.

In [65], Dinsmoor et al. have determined the underlying reasons for the unsuccessful field trials and identify the essential operating parameters of UCG. The cavity growth and its ultimate size are also identified by this model. Kuyper et al. [66] have proposed a 2D model to study the influence of geometrical aspects of a channel on mass transfer and natural convection flow rates. A simple model of gasification process in a rectangular channel is also developed. The simulation results of product gas composition are in a close match with the field data of Price-town I. Perkins and Sahajwalla [67] have proposed a pseudo-1D channel model to determine the product gas composition. The model includes a zero-dimensional steady state submodel of cavity evolution. The mass transfer equations are formulated through convection, heat transfer, reaction rates, characteristics of fluid flow and physical properties. The model results show a good agreement with the field data of Centralia, USA. In [68], Seifi et al. have developed an analytical steady state channel model for 1D coal seams. The model has been used to determine the effect of various operating parameters, such as oxidant injection rate, steam/oxygen ratio and channel length on the product gas composition.

The consideration of transport phenomena by natural convection played an important role in the development of channel modeling. It is found that channel models are better for the calculation of sweep efficiency. Moreover, these models are capable to investigate the cavity growth rate and the product gas composition of high-rank coal seams. In contrary to the coal block models, drying and pyrolysis phenomena are ignored in most of the channel models.

2.1.4 Resource Recovery Models

In literature, most of the models are simplified and are not capable to depict the complete UCG process. A comprehensive model of UCG is yet to be developed due to many factors. These include the complexity of a process which involves many interdisciplinary fields, most of the research in this field is not integrated and only focused to achieve local objectives, and conduction of field trials are expensive and time consuming. However, many approaches have been opted to develop a comprehensive model of UCG over the last few decades. These approaches are briefly discussed below.

Batenburg and Bruining [69] have opted a unique probabilistic simulation technique to formulate a 2D UCG model. This model has a limited scope, as the temperature and composition of gases are assumed constant in each region. In [70], authors have applied the same approach to develop an integrated three-dimensional (3D) model for UCG. This model is used to study the evolution of cavity in a UCG gasifier. In this model, the mass transport and reactive heat effects are combined with the properties of thermo-mechanical failure of overburden.

Britten and Thorsness have developed a comprehensive UCG resource recovery model to predict the cavity growth and water influx [22, 23, 40, 71–76]. The CAVSIM developed by Britten and Thorsness is a generalized cavity simulation model in which any flow schedule and composition of injected gases can be used. It is capable to simulate the UCG process for a wide range of overburden and coal compositions. The model mechanistically calculates cavity surface recession

rates from mass and energy balances. Moreover, it is capable to simulate the cavity growth for the entire life of UCG. It also integrates the results of different submodels, describing the dispersion of injected reactants and water influx from the surrounding aquifer. Moreover, it also incorporates the degradation of rubble-covered coal sidewalls due to thermal stress and chemical reactions, the recession of cavity surfaces due to radiation-driven spalling and gasification, and also calculates the growth of outflow channel. In [77, 78], authors have proposed a 3D UCG simulator (UCGSIM3D), which provides few advances over the CAVSIM like flexible 3D geometry, customized geological parameters, multiple rock strata and coal seams. UCGSIM3D is defined as a full-scope UCG simulator, as it is helpful in making the engineering decisions related to UCG, including site selection, module geometry, composition and flow rate of inlet gas, groundwater pumping wells location and extraction rates, and environmental monitoring plan.

Samdani et al. [25, 85] have proposed computational fluid dynamic (CFD) models for the vertical and lateral cavity growth by using the compartment modeling approach. The experimental data of spalling, kinetics and Indian lignite coal bed parameters are used to solve the model equations. The cavity growth is predicted by using the proposed models of the void, rubble and roof zones, and the outflow channel. The models are used to determine the performance of a lignite coal reserve of Vastan, India. The model results for the heating value and composition of syngas are compared with the experimental results obtained from a laboratory-scale UCG setup. In [86], authors have presented a numerical approach to perform a sequentially coupled 3D flow-geomechanical simulation in order to investigate the integrity of bedrock and cap-rock under different operational conditions and at different time instants. The simulations are performed for Swan Hills, Alberta, Canada with the aid of available commercial software to predict pressure and temperature profiles, cavity growth, variation in porosity and permeability, deformation and stress in rock and coal layers.

The various types of UCG models reviewed in this section are summarized in Table 2.2. It is seen that the packed bed, channel and coal block models are less complex and mostly used at laboratory-scale. Moreover, these models are not

TABLE 2.2: Some important features of the reported UCG models

| Author/s | Year | Model formulation | | Heat transfer | | | Mass diffusion | Fluid flow ² | Cavity Evolution | | | Interaction with environment | | |
|---------------------------------|------|-------------------|------------------------------|---------------|------------|-----------|----------------|-------------------------|--------------------|--------------------------|---------------|------------------------------|-----------|-----------|
| | | Dimension | Time dependence ¹ | Conduction | Convection | Radiation | | | Chemical reactions | Thermomechanical failure | Bulk collapse | Water influx | Heat loss | Mass loss |
| Packed bed models | | | | | | | | | | | | | | |
| Gunn & Whitman [47] | 1976 | 1D | PS | ✓ | | | ✓ | | ✓ | | | ✓ | | |
| Winslow [50] | 1977 | 1D | T | ✓ | ✓ | | | D | ✓ | | | | | |
| Thorsness et al. [48, 49] | 1978 | 1D | T | ✓ | ✓ | | | D | ✓ | | | | | |
| Thorsness & Kang [79] | 1985 | 2D | T | ✓ | ✓ | | ✓ | D | ✓ | ✓ | | | | |
| Abdel Hadi & Hsu [52] | 1987 | 1D | T | ✓ | ✓ | | ✓ | | ✓ | | | | | |
| Khadse et al. [53] | 2006 | 1D | PS | ✓ | ✓ | | | D | ✓ | | | | | |
| Uppal et al. [54] | 2014 | 1D | PS | ✓ | ✓ | | | D | ✓ | | | | | |
| Channel models | | | | | | | | | | | | | | |
| Magnani & Ali [62] | 1975 | 1D | | ✓ | ✓ | | | | | | | | | |
| Pasha et al. [64] | 1978 | 2D | T | ✓ | ✓ | | | | ✓ | | | | | |
| Dinsmoor et al. [65] | 1978 | 1D | T | ✓ | ✓ | ✓ | | P | ✓ | ✓ | | ✓ | ✓ | |
| Eddy et al. [80] | 1983 | 1D | T | ✓ | ✓ | ✓ | ✓ | M | ✓ | | | ✓ | | |
| Kuyper & Van [81] | 1994 | 2D | T | ✓ | ✓ | ✓ | ✓ | NS | ✓ | | | ✓ | | |
| Batenburg [82] | 1995 | 1D | SS | ✓ | ✓ | ✓ | | D | ✓ | | | | ✓ | |
| Pirlot et al. [83] | 1998 | 2D | S | ✓ | ✓ | | ✓ | D | ✓ | | | ✓ | | |
| Perkins & Sahajwalla [67] | 2008 | 2D | T | ✓ | ✓ | ✓ | ✓ | M | ✓ | | | ✓ | ✓ | |
| Luo et al. [84] | 2009 | 2D | T | ✓ | ✓ | ✓ | ✓ | | ✓ | | | | | |
| Seifi et al. [68] | 2013 | 1D | S | ✓ | ✓ | | ✓ | P | ✓ | | | | | |
| Coal block models | | | | | | | | | | | | | | |
| Tsang [56] | 1980 | 1D | T | ✓ | ✓ | ✓ | ✓ | | ✓ | | | | | |
| Massaquoi & Riggs [57, 58] | 1983 | 1D | S | ✓ | | | | D | ✓ | | | | ✓ | |
| Park & Edgar [59] | 1987 | 1D | T | ✓ | ✓ | | | D | ✓ | | | | | |
| Perkins & Sahajwalla [60] | 2005 | 1D | PS | ✓ | ✓ | ✓ | ✓ | NS | ✓ | ✓ | | ✓ | ✓ | |
| Resource recovery models | | | | | | | | | | | | | | |
| Britten & Thorsness [22] | 1989 | 2D | T | ✓ | ✓ | ✓ | ✓ | M | ✓ | ✓ | | ✓ | ✓ | ✓ |
| Biezen et al. [70] | 1996 | 3D | PS | | | | | D | ✓ | ✓ | | | | |
| Nitao et al. [77, 78] | 2011 | 3D | T | ✓ | ✓ | ✓ | | M | ✓ | ✓ | ✓ | ✓ | ✓ | ✓ |
| Samdani et al. [25, 85] | 2016 | 2D | T | ✓ | ✓ | ✓ | | M | ✓ | ✓ | | ✓ | ✓ | |
| Akbarzadeh et al. [86] | 2016 | 3D | T | ✓ | ✓ | | ✓ | D | ✓ | ✓ | | ✓ | | |

T=Transient, S=Steady state, PS=Pseudo-steady state, SS=Semi-steady state, D=Darcy flow, M=Mixed and NS=Navier Stokes.

capable to predict the cavity growth due to thermo-mechanical failure phenomena for a field-scale UCG site. Contrarily, the resource recovery models are more comprehensive and some of the models have been applied at the field-scale for the prediction of cavity growth. But these models have high complexity due to the incorporation of 2D and/or 3D geometry.

2.2 Control of UCG Process

The design of UCG control system is a formidable task, as the process occurs in-situ and it involves slowly varying disturbances, uncertainties of in-situ environment

and lack of direct control over the process parameters. Moreover, the installation of sensors at various locations in the UCG reactor is in itself a challenging task [19]. Thus, it is not possible to measure all the essential hydrological and geological parameters of the UCG process. Most of the UCG fields have real time data acquisition system to measure the temperature, composition, pressure and flow rate of injected and product gases [13, 87]. In industrial applications like IGCC, the heating value and flow rate of syngas are important performance indicators for any UCG site [24]. The only tuning knobs to attain the desired heating value and flow rate of syngas are the inlet gas flow rate and composition. Few studies have been reported about the design of a closed-loop system for the UCG field.

2.2.1 Related Work

In the literature, UCG control system is designed by employing model-free and model-based control techniques. Numerous model-free control design techniques have been reported in the literature. In [88], authors have designed a multi-variable adaptive model predictive control (AMPC) for the laboratory-scale UCG setup. A black-box method called multi-variate adaptive regression splines (MARS) is employed to formulate a model. The model is validated with the experimental data acquired during laboratory gasification. An ex-situ reactor is created to measure the process variables and to assess the possibility of control in UCG. A monitoring system is proposed to record the experimental data, such as inlet gas volumetric flow, the concentration of produced gas species, and temperature of syngas, overburden, underburden and inside the gasifier. The syngas heating value and underground temperature are controlled by manipulating the outlet relative pressure, flow rate of O_2 and air. The proposed multi-variable control design is not applicable at the field-scale UCG, as the real time monitoring of underground temperature is not possible at the UCG site. In [89–91], various controllers, such as proportional summing (PS), bang-bang and proportional integral (PI) have been implemented for the laboratory-scale UCG setup. The controllers are employed to control the temperature, concentrations and heating value of syngas. In [92],

authors have designed an optimal controller for the similar UCG setup, in which the amount of CO is maximized. The idea of UCG control system based on lab-scale setup cannot be employed on the actual UCG field [19, 93].

One of the methodologies to design a UCG control system for the actual field is the selection of a suitable model, then a model-based control technique can be used to achieve the required objectives [93]. The model-based control technique has been used for UCG to maintain the heating value of syngas. In [94], Uppal et al. have designed an equivalent control based SMC [95] for the simple UCG model comprising of ordinary differential equations. The model is based on the assumption that all the states are measurable, which is not possible at the actual site. In [54], authors have proposed a sophisticated control oriented 1D packed bed UCG model comprising of partial differential equations. The syngas composition and heating value are determined as a function of coal bed properties and different operating parameters. Moreover, a constrained nonlinear optimization technique is implemented to optimize three stoichiometric coefficients of coal pyrolysis reaction. In [55, 96], authors have proposed the design of super-twisting and conventional sliding mode controllers (SMCs), respectively, which are based on the model of [54]. Moreover, the state measurements are not required for the implementation of controllers and the calorific value of syngas is maintained at the desired level. In [97, 98], authors have employed the simple UCG model of [94] to design an integral sliding mode control (ISMC) and dynamic integral mode control (DISMC) for maintaining the desired heating value trajectory. A gain-scheduled modified Utkin observer has been designed to reconstruct the unknown states. It has also been shown that the proposed nonlinear control and estimation techniques exhibit robustness against parametric uncertainties, an input disturbance and measurement noise.

In the above-mentioned literature [54, 55, 94, 96–98], nonlinear process models have been employed to design various SMCs for the development of UCG control system. The design of such a control system is highly complex and it requires large computational resources and cost [99]. On the contrary, the complexity of the control design task can be reduced by using a linear model, which sufficiently

retains the system's dynamics [93, 99]. Chaudhry et al. [93] has linearized the simple UCG model proposed by [94]. The linear model is used to design a robust multi-objective H_2/H_∞ controller. The heating value of syngas is maintained at the desired level by manipulating the inlet gas flow rate. The model-free and model-based control techniques for UCG are summarized in Table 2.3.

2.3 Gap Analysis

For any UCG site, the information about the multi-dimensional phenomena of cavity growth has a paramount importance to perform the essential technical, environmental and economic feasibility analysis of a UCG field [9, 13, 15, 20]. Like other UCG fields, UPT has real time data acquisition system to measure the chemical process parameters, such as composition, flow rate, pressure and temperature of injected and product gases. While UPT lacks such instrumentation to monitor the hydrological and geological conditions like water influx rate, cavity growth and its interaction with overburden. An intensive real time monitoring system is required to measure these process details. While the installation of such a monitoring system in itself is a challenging task. Hence, a detailed simulation study is required to address the real time monitoring issues related with the UPT field. The simulation studies already available in the literature are also not applicable to the UPT field, as the cavity growth itself is a function of the operating conditions

TABLE 2.3: Control techniques for UCG

| Controller | Model Type | Manipulating Variables | Control Objectives |
|----------------------|--------------|--|---|
| AMPC [88] | Model-free | O ₂ and air flow rates and outlet relative pressure | Syngas heating value and UCG gasifier temperature |
| PID [89–91] | | Inlet gas flow rate | Concentrations, temperature and heating value of syngas |
| Optimal control [92] | | Inlet gas flow rate. | Maximization of CO content in syngas |
| SMC [94] | ODE | Inlet gas flow rate | Syngas heating value |
| SSMC [54] | PDE | | |
| SMC [96] | PDE | | |
| ISMC [97] | ODE | | |
| DSMC [98] | ODE | | |
| H_2/H_∞ [93] | Linear model | | |

and coal bed properties of any UCG site. In Table 2.2, it can be observed that only the resource recovery models are capable to predict the multi-dimensional cavity growth phenomena and water influx for a field-scale UCG system. Hence, an appropriate resource recovery model needs to be selected to achieve the desired research objectives.

The potential of a UCG site to produce electricity is determined by energy output per unit time, which relies on the heating value and the mass flow rate of syngas. [24, 25, 85]. The model-free control designs presented in Table 2.3 are applicable only for a laboratory-scale UCG setup. However, the laboratory-scale experiments are not sufficient to reflect the actual UCG field [13] In [88–92], so these control designs can not be implemented at the actual UCG site. Table 2.3 also highlights various model-based control techniques that have been designed for a field-scale UCG setup. It is observed that the heating value of syngas is considered only as a key indicator to determine the performance of a UCG field. In the literature, a single control objective is considered, in which the heating value of syngas is maintained at the desired level by varying the flow rate of inlet gas. While the authors have ignored the flow rate of syngas, which has also a significant role to determine the potential of a UCG site to produce electricity. Moreover, most of the control designs are based on nonlinear process models, resulting in a highly complex control system that requires large computational resources and cost. Hence, it is essential to design a multi-variable, model-based control system for the UPT field. In model-based control design, the controller expressions are derived from the model, therefore, a relatively simple model is required for the design of a model-based control system.

2.4 Selection of Model for the UPT Field

The selection of a model has an important role in the design of model-based control technique. The capabilities of the model to predict the essential process parameters and ease of control design are important factors in the selection of

model, but there is always a trade-off involved in it. As described in section 2.3, a comprehensive resource recovery model is required to predict the essential process parameters of the UPT field. Thus, it is important to highlight the capabilities and shortcomings of these models more in detail.

Numerous resource recovery models are developed to study the cavity growth in UCG [20, 25, 40, 70, 78, 85, 100]. In [70], Beizen et al. have applied the probabilistic simulation approach to develop an integrated 3D channel model for UCG. In this model, the mass transport and reactive heat effects are combined with the properties of thermo mechanical failure of overburden to study the evolution of cavity. This modeling method is not feasible for low-rank coal seams, having high permeability. Najafi et al. [100] have developed a simple empirical model-based on nonlinear regression analysis. The proposed model is capable to predict the cavity growth rate for the given operating parameters of UCG site. This models does not account for the cavity shape, spalling of overburden and water influx rate. In [25, 85], authors proposed a CFD model to simulate the UCG process. The reaction kinetics, mass and heat transfer, permeability limits and the spalling of coal due to thermo-mechanical failure are investigated in an integrated manner. This model is only applicable to laboratory-scale UCG setup. In [20], authors have proposed a simple statistical model to predict the cavity shape and volume, based on data obtained from Daggupati et al. experiment [101]. This model is applicable to commercial scale only if the UCG site has similar coal bed properties and operating parameters as considered in initial experiment. The coal bed properties and operating parameters of UPT field have large disparity as compared to the parameters considered in that model. Thus, this model is not applicable to the UPT field.

Similarly, the research work in the area of UCG conducted at the LLNL, USA resulted in the development of CAVSIM and 3D UCG simulator (UCG-SIM3D) models [40, 78]. The essential chemistry, gas transport, heat transfer, water influx, spalling of overburden and coal and accumulation of rubble within the cavity are considered in the formulation of CAVSIM. The major attribute of this

model is that it is formulated on the basis of understanding and analysis experienced during various field trials [13]. In UCGSIM3D, the phenomena similar to CAVSIM have been modeled. It is a complex model, providing few advances over the CAVSIM like flexible 3D geometry, including multiple seams and rock strata, dip and spatially-varying properties of the geological materials.

A number of UCG models have been reported in the literature which are capable to predict cavity growth rate [20, 25, 70, 85, 100]. However, most of these models have been applied only at a laboratory-scale UCG setup. The models developed by LLNL i.e. UCGSIM3D and CAVSIM serve as a benchmark for a UCG process, and the sophisticated simulators of these models are also available [1, 13]. Although UCGSIM3D provides few advances over CAVSIM but the sideward and upward growth of cavity in coal seam and overburden is considered by spalling in both CAVSIM and UCGSIM3D models. The development of UCGSIM3D ended prior to its commercialization as a benchmark tool for non-experts [13]. In contrary to CAVSIM, UCGSIM3D is a complex model, requires high computational platforms and also a very limited literature is available regarding the formulation of UCGSIM3D. Moreover, the major attribute of CAVSIM is that it is formulated on the basis of understanding and analysis experienced during various field trials [13].

In this work, the CAVSIM is preferred over the UCGSIM3D due to the aforesaid reasons. As the CAVSIM is applicable only to the non-swelling coal seams of a modest thickness (6 – 9m), lying at modest depths (lower than 152.4 m) [21]. These coal deposits have low-rank nature of coal and large variation in coal seam thickness (0.3m to 42m) and depths (122m to 180m) [36, 37]. It has a very low free swelling index range from 0 to 1.5 [36]. The field test has been performed on a coal seam at the depth of 144m and having a thickness of about 7.62m. It can be seen that these parameters are within the acceptable range of CAVSIM, hence this model can be used for the UPT field. However, CAVSIM is not feasible from the control design perspective due to its complexity. While the trade off between the model prediction capabilities and the ease in control design can be mitigated by developing an approximate control-oriented model of CAVSIM, which retains the fundamental dynamics of the UCG process.

2.5 Problem Statement

As discussed in section 2.3, the real time monitoring of the cavity growth is a formidable task at the UCG site. Moreover, the development of a multi-variable closed-loop system has paramount importance to improve the performance of any UCG site, and particularly for the UPT field. Thus, the fundamental objective of this research work is two-fold:

1. Prediction of essential process parameters, such as cavity growth and its interaction with overburden, and water influx for the UPT field. Moreover, perform a comprehensive simulation study to investigate the effect of operating parameters of UPT on volumetric cavity growth and heating value of syngas.
2. Design of model-based multi-variable linear and nonlinear robust control techniques for the UPT field. The control objective is to maintain the desired levels of heating value and flow rate of syngas by manipulating the steam to oxygen ratio and inlet gas flow rate. Moreover, the designed control laws must be capable to cater the effect of external disturbance and the modeling inaccuracies.

2.6 Summary

In this chapter, a detailed literature review is presented about the modeling approaches and the design of a closed-loop system for the UCG process. The research openings are identified in the modeling and the control design for the UCG field. Moreover, a suitable model is selected for the prediction of parameters which are not possible to measure at the UPT site. Finally, the research problem has been formulated.

In the next chapter, the description of CAVSIM is presented. The CAVSIM parameterization and validation with the UPT field data have also been discussed. Moreover, the parametric study has been performed to investigate the effect of operating parameters on the cavity growth and the heating value of syngas.

Chapter 3

Mathematical Model of the UPT Gasifier

This chapter gives a detailed description of the CAVSIM, which has been selected to predict the cavity growth and other process details that are not measurable at the UPT site. The CAVSIM is parameterized with operating conditions of the UPT and properties of Lignite B coal of Thar coal fields. The model is validated with the field data of the UPT by comparing the composition and heating value of the syngas. The results are also compared with our previous 1D packed bed model [54], which shows that the predictions of CAVSIM are much closer to the actual data. Moreover, a comprehensive simulation study has been carried out to predict the cavity growth and its interaction with overburden. The parametric study is also carried out to investigate the effect of operating parameters on the cavity growth and the syngas heating value.

This chapter is organized in the following manner. The description of the model is given in Section 3.1. The experimental setup of the UPT field is presented in Section 3.2. The model parametrization and validation with the UPT field data is presented in section 3.3. In Section 3.4, model predictions are discussed in detail, followed by the parametric study in section 3.5. Finally, the chapter is concluded in section 3.6.

3.1 Model Description

The CAVSIM is a generalized model that can simulate the UCG process for a wide range of coal and overburden compositions and stratigraphy [21, 23, 40, 71–76]. Almost any flow schedule and composition of injected gases can be used in this model. It is applicable to flat-seam sub-bituminous or low-rank coals in which the oxidant injection point is considered at the bottom of the coal seam. An axisymmetric cavity geometry about an injection point is assumed to simplify the 3D growth into 2D. Although all apparent geometrical and thermo-physical symmetries have been exploited to simplify the problem, but it retains sufficient details to depict the main factors contributing to the cavity growth.

The model is capable to simulate the cavity growth for the entire life of UCG, and it mechanistically calculates cavity surface recession rates from mass and energy balances. It also integrates the results of interacting submodels, describing dispersion of injected reactants in a rubble bed, water influx from the coal aquifer, recession rates of coal sidewalls caused by thermal stress and chemical reactions, and the cavity evolution due to the radiation-driven spalling and gasification. It also calculates the rate of produced gas species and the growth of outflow channel. The model considers four solids: wet and dry coal, char (carbon) and ash. The complexity of the model is reduced by lumping $\text{CO}_2 + \text{H}_2\text{O}$ and $\text{CO} + \text{H}_2$ into two pseudo species such that only five gas-phase species are considered: O_2 , reactant agent $\text{R} = \text{CO}_2 + \text{H}_2\text{O}$, gasification product $\text{P} = \text{CO} + \text{H}_2$, CH_4 and inert I . The chemical reactions considered in this model are shown in Table 3.1. The simplification of reaction chemistry is justified by taking the similar stoichiometry of reactions R_2 and R_3 , and assuming that water-gas shift reaction (R_4) is in equilibrium at cavity temperature. Therefore, the relative amounts of CO_2 and H_2 can adjust instantaneously to the local thermal environment. In this model, the reaction rates of $\text{CO}_2 + \text{C}$ and $\text{H}_2\text{O} + \text{C}$ are taken similar, and the heat of reaction of R_2 is defined in terms of inlet gas composition. The CAVSIM consists of various interacting submodels and global cavity simulator model, which are briefly described in the following sub-sections.

TABLE 3.1: Chemical kinetics for cavity growth

| |
|---|
| $R_1 : O_2 + C \rightarrow CO_2$ $\Delta H^o = -393.51(kJ/mol), \quad \Delta G^o = -394.36(kJ/mol)$ Reaction rate ($mol/m^3.s$) [102]: $k_r(c_T - c_{eq})$, where, $k_r = A \exp^{-E/RT_o}$ |
| $R_2 : CO_2 + H_2O + 2C \rightarrow 3CO + H_2$ $\Delta H^o = 303.5(kJ/mol), \quad \Delta G^o = 211.5(kJ/mol)$ Reaction rate ($mol/m^3.s$) [102]: $k_r(c_T - c_{eq})$, where, $k_r = A \exp^{-E/RT_o}$ |
| $R_3 : O_2 + CO + H_2 \rightarrow CO_2 + H_2O$ $\Delta H^o = -524.8(kJ/mol), \quad \Delta G^o = -485.8(kJ/mol)$ Reaction rate ($mol/m^3.s$) [103]: $4.75 * 10^5 [CO][H_2O] \left[\frac{17.5 * \frac{[O_2]}{c_T}}{1 + 24.7 * \frac{[O_2]}{c_T}} \right] \exp(-8050/T_o)$ |
| $R_4 : H_2O + CO \rightleftharpoons H_2 + CO_2$ $\Delta H^o = +41.2(kJ/mol), \quad \Delta G^o = -28.62(kJ/mol)$ Reaction rate ($mol/m^3.s$) [104]: $568RT \left(0.5 - \frac{P}{2.53 * 10^7}\right) ([CO] - [CO]_{eq}) \exp(-13971/T)$ |

3.1.1 Water Influx Submodel

This model accounts for the flow rate of water in a UCG reactor. In UCG reactor, water can influx in various ways: injection of steam from the surface, drying and thermal decomposition of coal and rock, and flow of free water from the surrounding aquifers. The water entering due to drying and thermal decomposition of coal and rock is accounted by treating recession of these surfaces. While injected steam is prescribed by the steam flow rate in the model, and free water influx is computed by a simple model of saturated and unsaturated flow in the coal seam.

The free water influx is assumed homogeneous and determined by two mechanisms: gravity drainage and pressurizing the coal seam [40, 73].

The problem of computing gravity drainage of water is simplified by using Dupuit approximation which assumes that volumetric flux of water across any vertical plane can be approximated as [105]

$$F_{\text{H}_2\text{O}(l)} = -\Upsilon \frac{d\hat{h}}{dr_c}, \quad (3.1)$$

where $F_{\text{H}_2\text{O}(l)}$, Υ , \hat{h} , and r_c are the volumetric water flux (m/s), hydraulic conductivity (m/s), free surface height (m), and cavity radius (m), respectively. The dimensionless form of (\hat{h}) is determined by using (3.1) and applying conservation of mass

$$\begin{aligned} \nabla \cdot (\hat{h} \nabla \hat{h}) &= \frac{\partial \hat{h}}{\partial t}, & (3.2) \\ \hat{h} &= 1, \quad \text{for } r_c \geq r_0(0), \quad \text{and } t = 0, \\ \hat{h} &= 0, \quad \text{for } r_c = r_0(t), \quad \text{and } t \geq 0, \\ \hat{h} &\rightarrow 1, \quad \text{for } r_c \rightarrow \infty, \quad \text{and } t \geq 0. \end{aligned}$$

(3.2) along with initial and boundary conditions is solved numerically by finite difference method using standard Livermore solver for ordinary differential equations [106]. The de-pressurization mechanism is included in the Dupuit formulation by matching the drainage solution of (3.2) for the unsaturated and fully saturated region.

3.1.2 Flow Submodel

This submodel calculates the flow of injected gases through the distinct regions of ash rubble boundary. The boundary of ash pile is defined as the wall (ash–coal interface), the outer bed (char–ash rubble interface) and the inner bed (ash–void or ash–rock rubble interface). The model is formulated on the assumption that a region between the rubble and cavity wall is highly permeable relative to the

rubble [40, 72]. The flow distribution is found by solving compressible form of Darcy's law, represented in cylindrical coordinates as

$$\begin{aligned} \frac{\partial^2 P_o^2}{\partial z_c^2} + \frac{1}{r_c} \frac{\partial}{\partial r_c} \left(r_c \frac{\partial P_o^2}{\partial r_c} \right) + \frac{2RT_o\Omega\chi}{\kappa_a} &= 0, \\ \frac{\partial P_o^2}{\partial z_c^2} \Big|_{z_c} = \frac{\partial P_o^2}{\partial r_c^2} \Big|_{r_c} &= 0, \quad P_o^2(r = \psi(z_c, t)) = P_o^2 \text{sink}, \end{aligned} \quad (3.3)$$

where P , T_o are the pressure (Pa) and temperature (K) of inlet gas, respectively. R is the universal gas constant ($J/mol.K$), χ represents the viscosity of solids ($kg/m.s$), and κ_a is the ash permeability (m^2). While Ω represents the source strength of injection flow, which is nonzero only at the origin. ψ is a function describing location of permeable ash pile surface, and $z_c(m)$ is the cavity height. A finite difference algorithm is used to discretize 3.3 at each node, and then pressure at every node is computed by direct solution of the linear system in P^2 .

3.1.3 Wall Submodel

A thin, highly permeable wall layer of thickness $\delta(m)$ is assumed to exist between the ash pile and coal wall. This layer is filled by char and moves from left to right at a calculated speed, driven by thermally-induced rubblization of the coal wall on the right. The wall recession rate is determined by the heat flux which causes the break down of the wall into rubble [40, 72, 74, 75]. The relationship between temperature T_ω and recession rate v of the wall layer is obtained by the balancing of net energy around a wall segment j

$$\hat{Q}_{ox} = \hat{Q}_{dry} + \hat{Q}_{gf} + \hat{Q}_{H_2O(l)} + \hat{Q}_{p_{j-1}} + \hat{Q}_{ch}. \quad (3.4)$$

(3.4) can be written as:

$$F_{inj} [m_{O_2} h_{r_3} - C_g(T_\omega - T_o)] = v_\omega \rho_c \hat{Q}_c + [F_{ch} W_c + v_\omega \rho_c W_c] \frac{h_{r_2}}{M_c} + \quad (3.5)$$

$$F_{H_2O(l)} \hat{Q}_{H_2O(l)} + F_{p_{j-1}} C_g(T_\omega - T_{\omega_{j-1}}) + F_{ch} W_a C_s(T_o - T_\omega), \quad (3.6)$$

where \hat{Q}_i (W/m^2), F_i ($kg/m^2.s$ for solids, m/s for liquid, $mol/m^2.s$ for gases) are

the heat and material flux, respectively. $T_i(K)$, $h_{r_i}(J)$, C_i ($J/mol.K$ for gases, and $J/kg.K$ for solids) represent the temperature, heat of i^{th} reaction, and specific heat capacities, respectively. m_{O_2} is the molar fraction of O_2 , W_i is the weight fraction, v_ω (m/s) is the wall recession velocity, and ρ_c (kg/m^3) is the carbon density. The subscripts: *ox*, *dry*, *g_f*, $H_2O(l)$, *p*, *ch*, ω , **c**, *a*, *s*, and *inj* represent oxidation, drying, gasification, water, produced gas, char, wall, carbon, ash, solids, and injected gas, respectively.

The expression of convective heat transfer from the product gas to the cold coal wall relates the recession rate and reaction zone temperatures [74, 75]. The thickness $\delta(m)$ in terms of wall temperature (T_ω) is given by rearranging the equations given in [74, 75]

$$\delta = \left[\frac{\zeta_1 P_r^{1/3} \lambda_g \left(\frac{F_p d_p M_g}{\chi_g} \right)^{\zeta_2}}{\vartheta d_p} \frac{\ln \left(1 + \frac{T_\omega - T_f}{T^* + T_f - T_v} \right)}{F_{H_2O(l)} C_g + \rho_c v_\omega [W_{H_2O(l)} C_g + (1 - W_{H_2O(l)}) C_s]} \right]^{\zeta_3}, \quad (3.7)$$

where P_r is Prandtl number, ζ_i , $i = 1, 2, 3$ represent Constants which are depend upon the local Reynolds number, $\lambda_g(W/m.K)$, is the thermal conductivity of gas, $d_p(m)$ is the average particle diameter, $\vartheta(W/m^2.K)$ is the heat transfer coefficient, $\chi_g(mol/m.s)$ and $M_g(kg/mol)$ are the produced gas viscosity and molecular weight, respectively. T^* represents the wall heat transfer temperature (K), T_f, T_v, T_e are the temperatures (K) of failure, vaporization, and extinction conditions.

The mass balances around each segment give the product gas composition and flow rate as a function of injected gas rate and T_ω of segment. The effective extinction temperature (T_e) of the steam-char reaction in a packed bed is used to determine T_ω [76]. The solution of wall layer model is based on the assumption that gasification reactions quickly utilize the heat produced by oxidation reaction, such that product gas exits the segment at T_e .

3.1.4 Roof Rubble Submodel

The behavior of coal, char, and rock rubble pile surfaces around the void region of cavity is described in the model. The model is based on the assumption that side-wall material and roof spalling are major parameters in determining the behavior of the surface. When rock surfaces and coal are exposed to high temperature, spalling of material occurs due to thermally induced stresses. The heat transport from hot rubble bed surface to the spalling rock and coal surface, enclosing the void space is accounted by radiant heat [40, 72, 76]. The dynamics of char bed are described by assuming 1D packed bed model. The product gas composition, flow rate, and carbon conversion rates are derived as a function of temperature T_e . The molar fraction of product gas is given below

$$m_p = 2 \frac{T_e}{T_{inj}} \left[\frac{1 - \frac{M_c C_s m_{O_2}}{C_g W_c} - \frac{h_{r1} m_{O_2} T_{inj}}{C_g (T_e - T_{inj}) T_e}}{\frac{M_c C_s T_e (1 - m_{O_2})}{T_{inj} C_g W_c} - \frac{h_{r2} + h_{r1} m_{O_2}}{C_g (T_e - T_{inj})}} \right]. \quad (3.8)$$

The product gas flux and carbon conversion rate are given by

$$F_p = \frac{2F_{inj}}{2 - m_p}, \quad (3.9)$$

$$c_{c_r} = F_{inj} \left(m_{O_2} + \frac{m_p}{2 - m_p} \right). \quad (3.10)$$

The system is solved by an efficient modification to Newton's method in which the inverse Jacobian Matrix is calculated [107].

3.1.5 Outflow Channel Submodel

In this submodel, the interaction of product gas which dries, pyrolyzes and rubblizes the coal surrounding the bore-hole is estimated. This submodel is not effectively coupled with the main cavity model in a way that its presence does not affect the cavity growth, which means there is no feedback from the channel to the

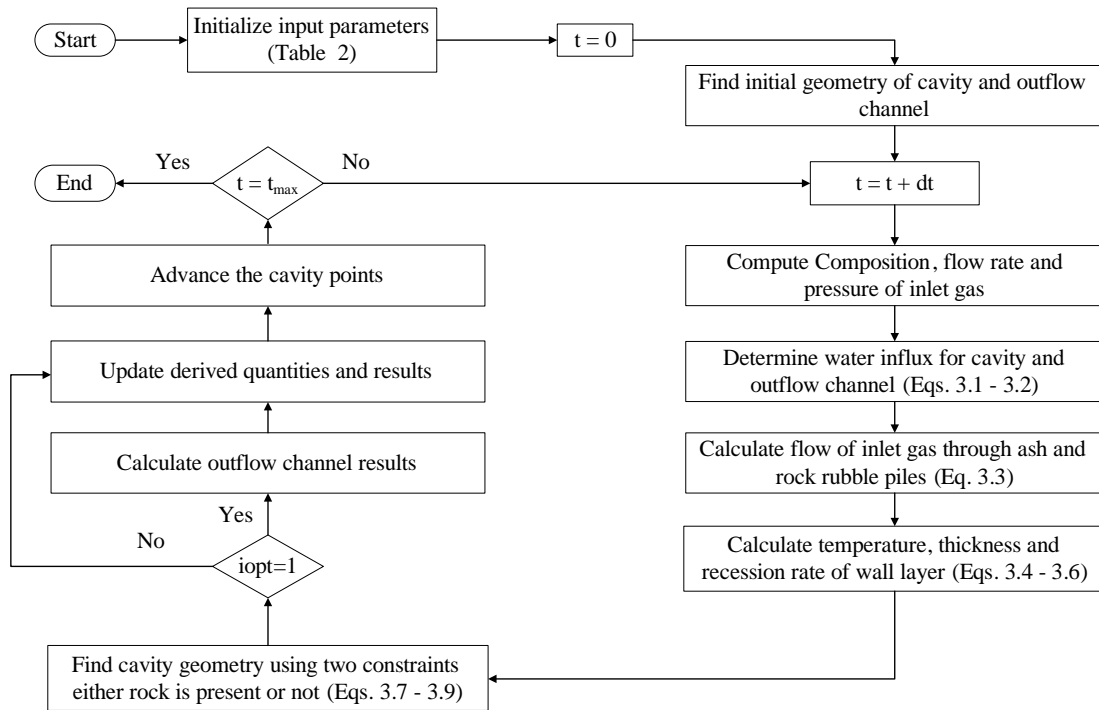


FIGURE 3.1: Solution routine of CAVSIM [40]

cavity. This submodel combines all the gas source terms to determine the composition and temperature of a product gas leaving the cavity. It determines the flow rate of produced gas species individually from the lumped species by using carbon balances and invoking water-gas-shift equilibrium. The amount of coal pyrolysis and material balances give the amount of hydrocarbon (CH_4) and inert gas (N_2), respectively.

3.1.6 Cavity Growth Module

It is the main module that obtains the results of submodels described above and uses them to calculate the boundaries of ash, char, and rock rubble pile. Initially, half of a right circular cylinder is used to define the cavity geometry. It is divided into a series of segments by points equally spaced along the boundary. Initial size of char rubble pile is also specified. The submodels described previously, use the geometrical data to calculate recession rates, temperatures, and rates of chemical reactions for different surface segments. This module uses a control segment to find the new location of cavity points and computes tentative cavity boundaries and

amounts of rubble. A distinctive shape of the cavity is determined by considering different situations like, whether the cavity is interacting with overburden rock or it is confined in the coal seam. The solution routine of CAVSIM is briefly described in Fig. 3.1.

3.2 Experimental Setup

The important components of the UPT experimental setup include UCG field, compressors, gas analyzer and control room. The schematic of the process is shown in Fig. 3.2.

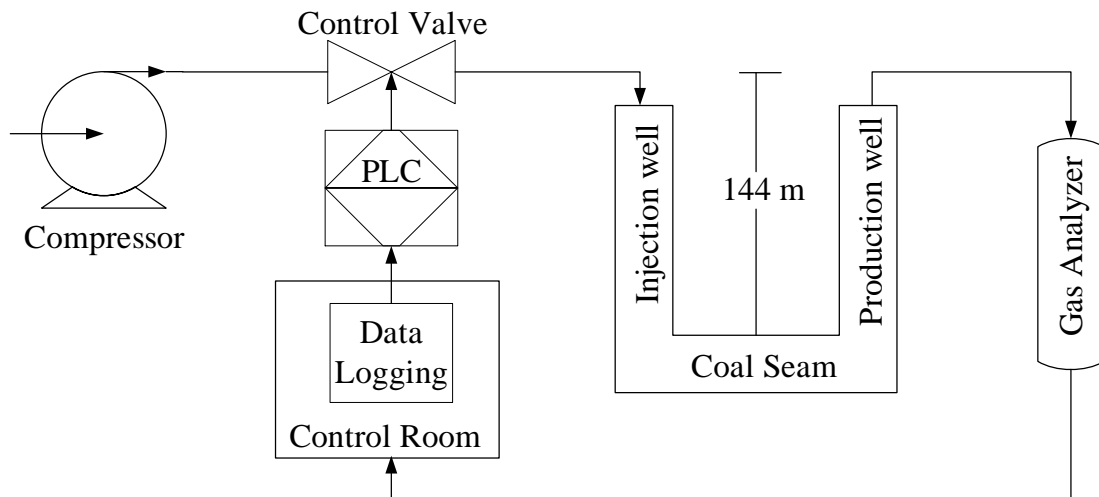


FIGURE 3.2: Process schematic diagram

The UPT field is shown in Fig. 3.3, and it consists of a network of pipes and wells, spanning an area of 18750 m². There are many UCG design concepts, which are mainly classified on the basis of drilling methods, placement of process wells and their linking techniques [9]. Linked vertically wells technique is used in the design of the UPT field. In a single gasifier, a pair of injection and production wells is necessary. The purpose of injection well is to supply compressed oxidants to the coal seam while production well transports the product gas to the gas analyzer. Air at a specific flow rate and pressure is supplied to the injection well through blue pipes, while the red pipes carry syngas from the production well to the gas

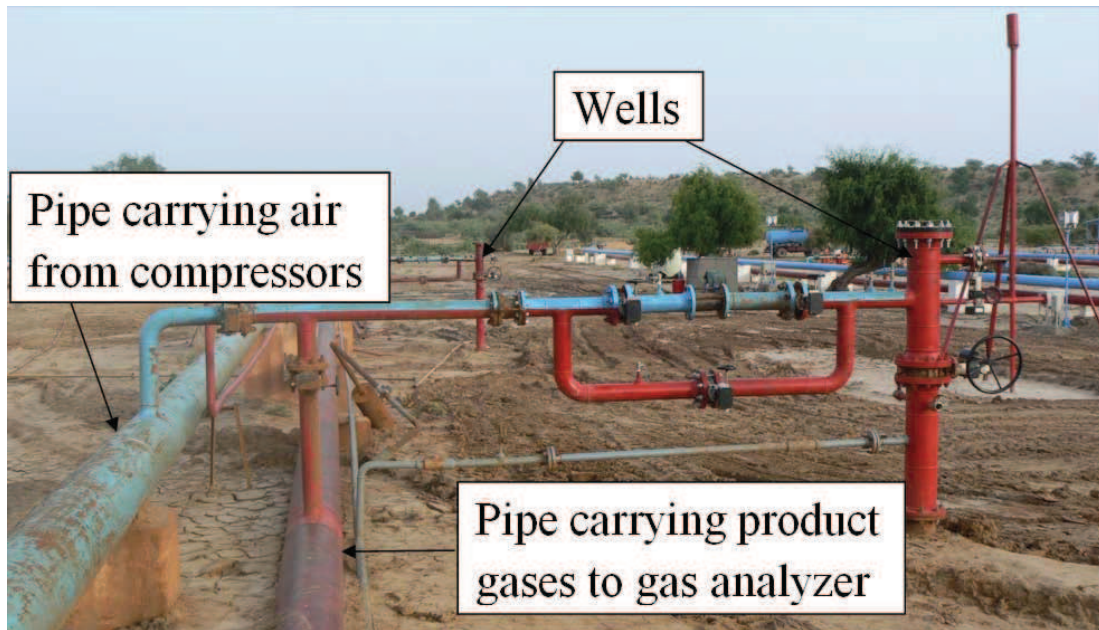


FIGURE 3.3: Field area of the UPT [54]

analyzer. In a commercial UCG process, a number of coal seams are gasified concurrently, therefore, having multiple production wells to recover the product gas. However, this experiment was conducted for a single coal seam located at the depth of 144 m from the surface.

The permeability of coal seam is low, therefore, the RCL technique is used to establish a permeable channel between the wells. In RCL, oxidants are injected in one well while coal seam is ignited from other well. The idea is to establish low hydraulic resistance path between the wells by propagating combustion front towards the oxidant source. During the link establishment, air is supplied to the coal seam through the high pressure compressors. The low pressure compressors are used to supply air to the already ignited coal seam during gasification process.

The flow rate of injected air is set by the control valve. The percentage opening of the control valve is controlled by the programmable logic controllers (PLCs). The product gases are sent to the gas analyzer after removing steam. The coal gas analyzer [108] is used to measure the molar fraction of syngas and then heating value of gas mixture is calculated. A dual beam non dispersive infrared (NDIR) detectors are used to measure the molar fraction of CO_2 , CO , CH_4 and C_nH_m .

The molar fraction of O₂ and H₂ are measured by galvanic fuel cell and thermal conductivity detector (TCD), respectively. While the molar fraction of N₂ is calculated by using the measured values of other gases. The heating value of syngas is determined by (3.11).

$$HV_e = m_{CO_e} H_{CO} + m_{CH_4_e} H_{CH_4} + m_{H_2_e} H_{H_2} + m_{C_n H_m_e} H_{C_n H_m}, \quad (3.11)$$

where HV_e represents the experimental heating value of syngas (KJ/m^3), H_i and m_{i_e} are the heat of combustion (KJ/m^3) and experimental molar fraction percentage of syngas component i , respectively.

3.3 Model Validation

The simulation results of CAVSIM have been validated with the field trials carried out at the UPT gasifier. The details of parametrization and comparison of simulated and experimental data are given in the following subsections.

3.3.1 Model Parametrization

The process of UCG is sensitive to the operating conditions and coal bed properties. The operating conditions include composition, temperature, pressure and flow schedule of injected gas mixture. The parametrization of CAVSIM has been carried out by the data obtained from the UPT field. The detail of the parameters is given in Table 3.2.

3.3.2 Results Comparison

The simulations are performed for 1.5 days with a step size of an hour to compare the experimental and simulated results. Air is used as an oxidizing agent. The time profile of air flow rate is shown in Fig. 3.4. In Fig. 3.5, the composition

TABLE 3.2: Parameters used in simulation

| Parameters | | Values |
|------------|---|-------------------------|
| Solid | Coal Type | Lignite B |
| | Density of Coal (kg/m^3) | 1250 |
| | Molecular weight of Coal (kg/mol) | 0.02 |
| | Initial particle diameter (m) | 0.01 |
| | Adjacent coal open or flow porosity | 0.005 |
| | Coal Permeability (m^2) | $1.97e^{-13}$ |
| | Ash Permeability (m^2) | $2.96e^{-12}$ |
| | Rock Permeability (m^2) | $2.96e^{-12}$ |
| | Coal weight fraction | 0.2822 |
| | Ash weight fraction | 0.1892 |
| | Moisture weight fraction | 0.3682 |
| | Volatile Matter | 0.3824 |
| | Heat capacity ($J/kg/K$) | 1650 |
| | Constant thermal conductivity ($w/m/K$) | 1.0 |
| | Coal failure temperature (K) | 700 |
| | Coal roof failure length (m) | 0.01 |
| Gas | Composition of injected gas | Dry air |
| | Injection flow (mol/s) | Actual UPT field data |
| | Pressure of gas at the inlet (Pa) | $6.18e+6$ |
| | Temperature of gas at the inlet (K) | 430 |
| | Ambient temperature (K) | 285 |
| | Steam temperature (K) | 373 |
| | Heat source temperature (K) | 1000 |
| | Constant roof temperature (K) | 1000 |
| | Viscosity functions ($kg/m/s$) | $4.0e^{-6}, 2.93e^{-8}$ |
| | Heat capacity ($J/mol/K$) | 45 |
| | Pyrolysis gas molecular weight (kg/mol) | 0.02 |
| Cavity | Initial cavity geometry | Right circular cylinder |
| | Initial cavity height and radius (m) | 3.62, 1.82 |
| | Cavity pressure (Pa) | $3.05e+5$ |

and heating value of syngas predicted by CAVSIM and by 1D packed bed model of [54] are compared with the UPT field data. It can be seen that the CAVSIM predictions are much better than the results produced by [54]. In Table 3.3, the relative errors (3.12) of field data (y_{exp}) and simulation results (y_{sim}) are shown for both models.

$$\|e_{rel}\|_2 = \frac{\|y_{sim} - y_{exp}\|_2}{\|y_{exp}\|_2}. \quad (3.12)$$

Therefore, a comprehensive simulation study is carried out in the subsequent sections to predict the cavity growth and its impact on the UCG process. Furthermore, the effect of operating parameters on cavity growth and heating value of product gas are also studied.

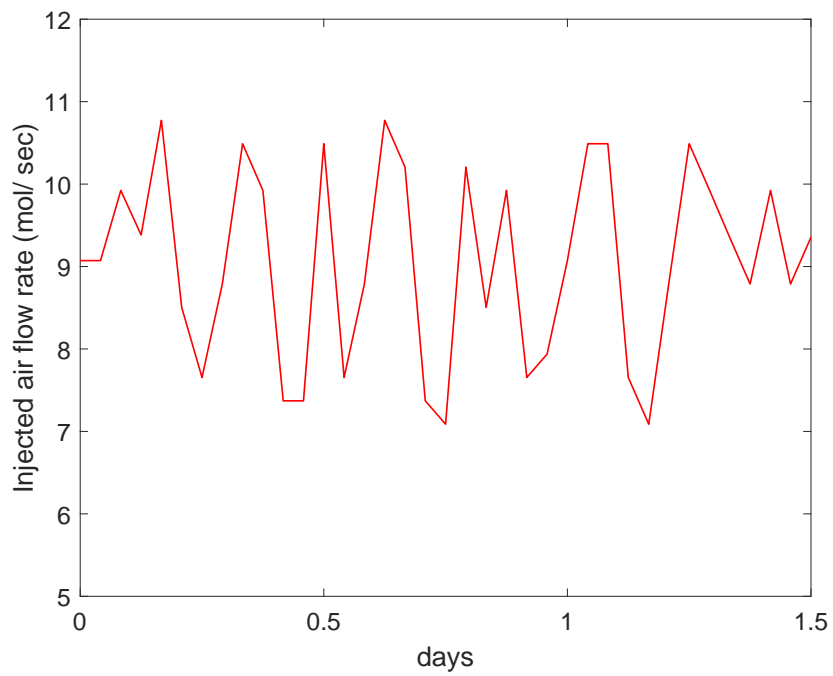


FIGURE 3.4: Flow rate of injected air

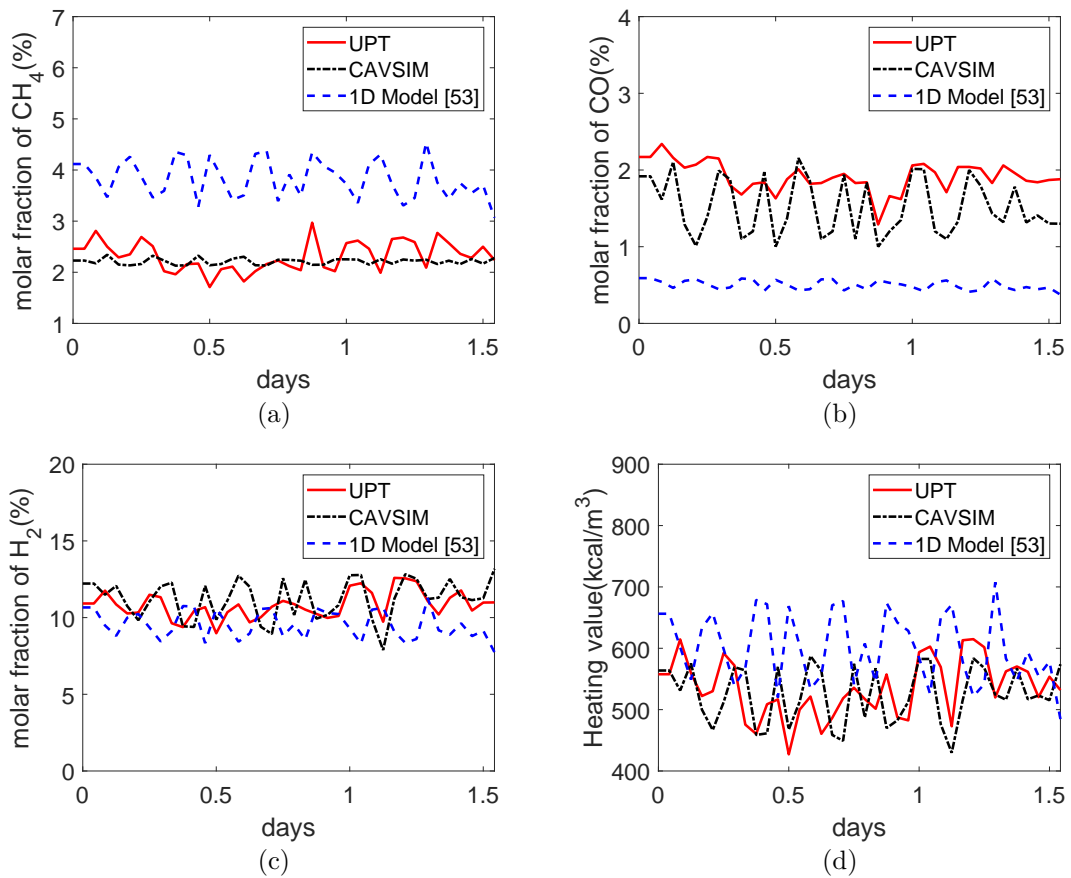


FIGURE 3.5: Model validation: (a-c) Molar Fraction of Syngas Species with Time, (d) heating value of syngas

TABLE 3.3: Relative error for field and predictions of models

| Parameter | % Relative error (CAVSIM) | % Relative error (1D Model [54]) |
|-----------------|------------------------------|-------------------------------------|
| CH ₄ | 13.67 | 68.39 |
| CO | 26.23 | 74.44 |
| H ₂ | 9.12 | 14.59 |
| Heating value | 9.49 | 20.13 |

3.4 Model Predictions

In this section, CAVSIM is used to predict the important UCG phenomena for the UPT field trials. The simulations are performed to predict the cavity growth and its interaction with the overburden. Moreover, the effect of cavity growth on char production, water influx and produced species flow rates, molar fraction and heating value of the product gas are studied.

The simulations are performed for 45 days to investigate the evolution of cavity in the UPT field. Fig. 3.6 shows the prediction results of cavity growth at various stages of the process. The flow rate of injected air reaches a distinct region of the cavity as shown in Fig. 3.7. The geometry of the rubble region is characterized with points a , b , c and d , as show in Fig. 3.6. It can be seen that different points are coincident in time due to appearing and disappearing of various rubble materials. The top of ash pile is defined by points b and c , and angle γ of line which joins these points. This angle is used to approximate a somewhat rounded ash rubble pile. The char pile top is defined by points a and d , and the top of rock rubble is defined by point a . The line between points a and d makes an angle ω , which is a model parameter used to represent the angle of repose of char rubble. γ and ω are measured in radians from the horizontal defining the slope of the top of the outer portion of the ash bed and the slope of the top of the char bed, respectively. The wall region is defined as the cavity boundary extending downwards to the bottom of cavity from point c . The material balances and angles γ and ω are used to determine the location and evolution of these points.

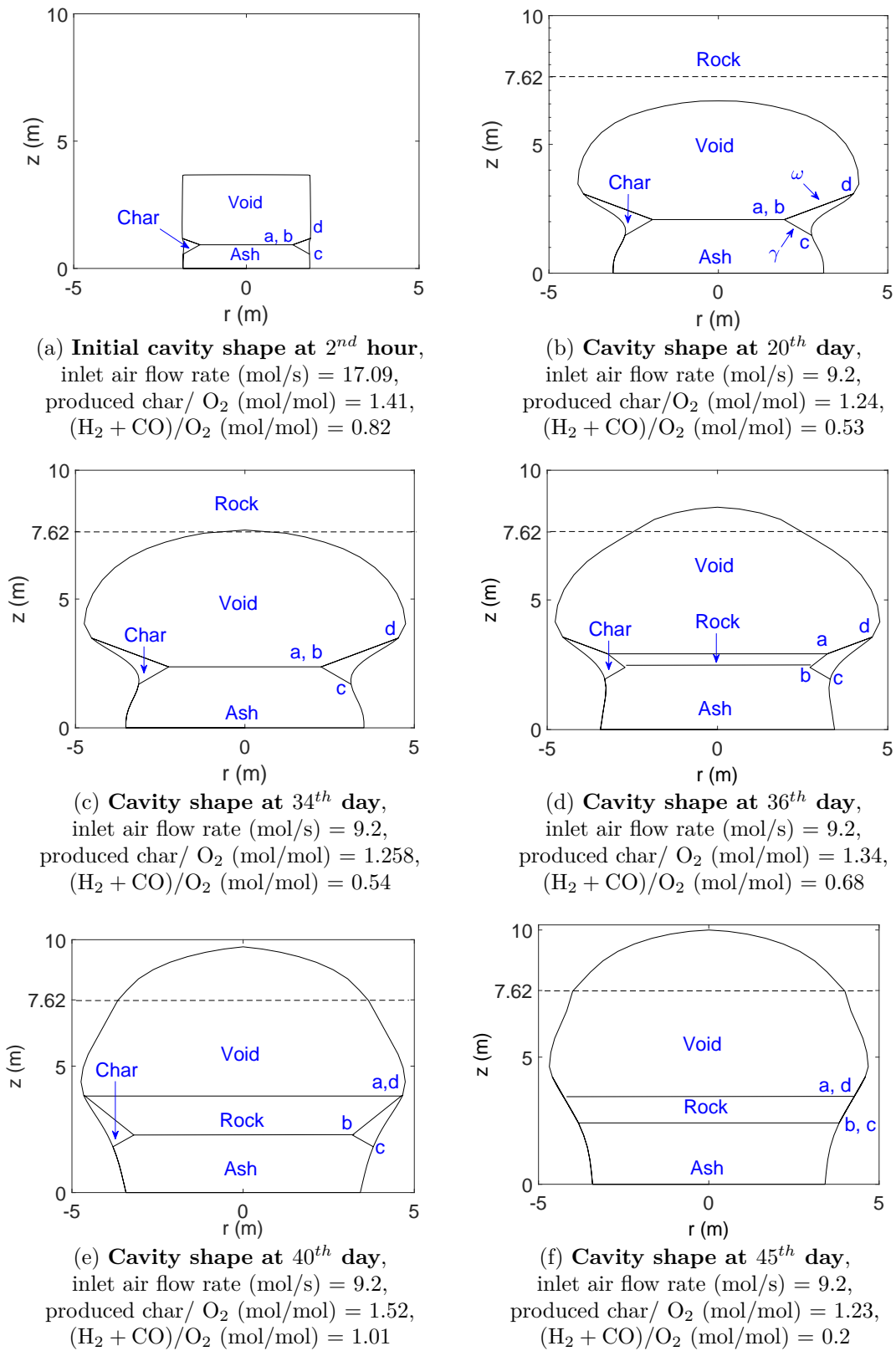


FIGURE 3.6: Cavity shapes at various stages of UCG

The rubble pile top (rubble–void interface) is divided into outer and inner bed. The outer bed is represented by points a and d , while points a and b characterize the inner bed, as shown in Fig. 3.6d. The char accumulates onto the outer bed due to spalling of roof and rubblization of adjacent coal side wall. The rubblization of wall takes place in accordance to the heat transfer mechanism, explained in section (3.1.3) [40]. The outer bed loses char due to the number of factors which include: reaction with injected gases, fraction of char rolls off onto the inner bed where it is consumed by various chemical reactions and settling of char along the wall zone. The inner bed is in the middle of the rubble surface where no net char accumulation is allowed. There exists a condition according to which char can only be present in the inner bed as a thin quasi-steady layer. When enough amount of char is present in this region to consume all the injected O_2 , the endothermic gasification reaction is balanced with the heat loss from the bed by radiation. This balance determines the ultimate composition of product gas and temperature reaching the void. Contrarily, for the insufficient char, it is assumed that void space is well-mixed such that gas species 'P' in a void space react with excess O_2 , which causes heat radiation to the remaining surfaces enclosing the void.

The cavity geometry is initially assumed as a right circular cylinder with radius, $r = 1.82\text{m}$ and height, $z = 3.62\text{m}$. The initial cavity shown in Fig. 3.6a is rectangular due to the assumption of axisymmetric cavity growth around the injection point which simplifies the 3D growth into 2D. The cavity shape for the situation when cavity lies within the coal seam is determined by taking into account the amount of char falling in the inner ash rubble surface, which determines the upward growth of that surface, distribution of temperature in the enclosure and amount of char left in the rubble bed. Thus, only one solution exists for the char appeared on ash–void interface represented by the position of point b in Fig. 3.6b and Fig. 3.6c, which simultaneously satisfies both ash and char material balances. This solution is determined by performing iterations on α and uses golden section algorithm. It is observed in Fig. 3.6b and Fig. 3.6c that the cavity grows smoothly in all directions and its rate of lateral and upward growth relatively remains constant when the cavity is confined to the coal seam. It is also observed that the

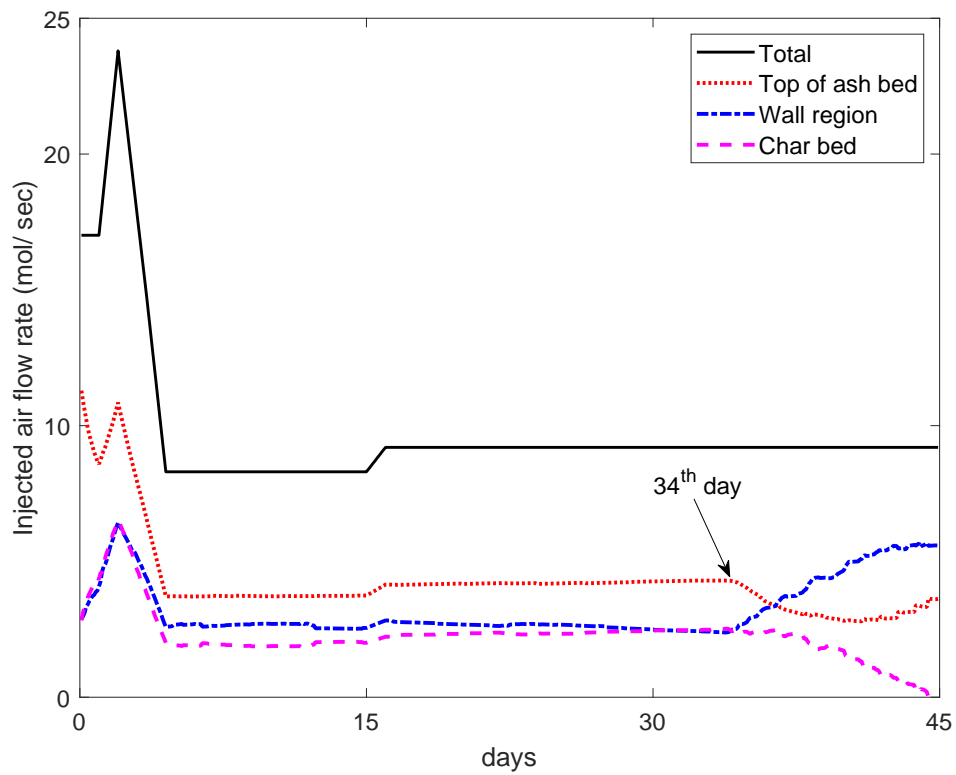


FIGURE 3.7: Flow rate of injected air

amount of unburned char increases in proportion to the cavity volume.

When the cavity includes rock, it can be observed in Figs. 3.6c-3.6f that the ash pile controls the injected gas flow distribution, stops to grow upward and its height becomes constant. Thus, the location of point *b* is determined by only the ash mass balance, while point *a* is fixed at a place where char and rock rubble material balances are simultaneously satisfied. Fig. 3.6e shows the situation when char region is completely covered by the rock rubble and represented by the coincidence of points *a* and *d*. Finally, the char depletion situation is described in Fig. 3.6f, where point *b* moves radially and coincides with point *c* at a constant height due to the char material balance.

In Fig. 3.7, the dispersion of inlet air inside the UCG gasifier during various stages of cavity evolution is presented. It is observed that the flow rate of inlet air increases towards the wall region when the cavity interacts with the overburden rock on the 34th day. At the same time, the flow of inlet gas towards the other regions is decreasing. The molar ratios of produced char and produced gas ($P = \text{CO} + \text{H}_2$)

to the rate of injected O_2 is shown in Fig. 3.8, which are important quantities to measure the performance of a gasifier. The behavior of molar ratios follow the same trend as the rate of injected O_2 till 34th day. In Fig. 3.8, the change in behavior of molar ratios near the 34th day is due to the interaction of cavity with the overburden rock. When the overburden rock is included in the cavity, the flow rate of injected air increases towards the wall region as shown in Fig. 3.7. This increases the molar ratios of produced char and produced gas. It can be seen that the molar ratios decrease abruptly after 40th day, as the char region is completely covered by the overburden and char begins to deplete from the cavity as discussed previously.

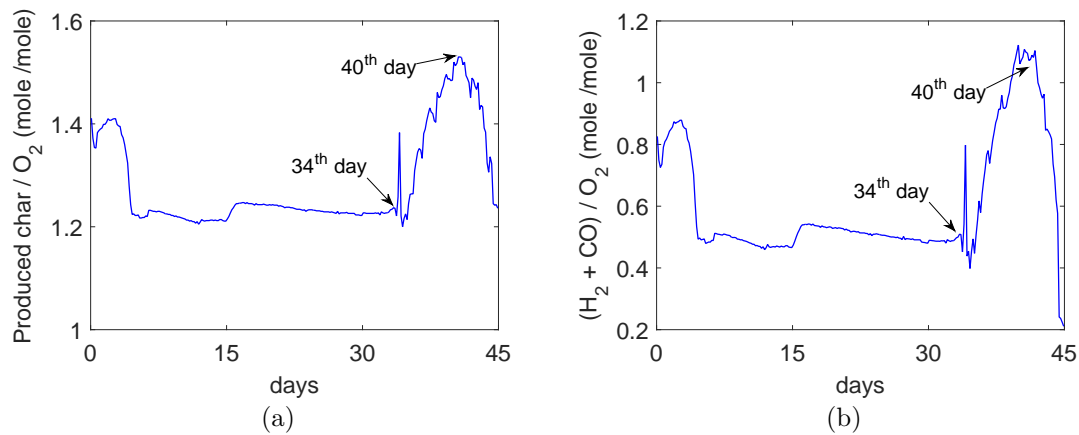


FIGURE 3.8: Molar ratio of (a) produced char and (b) $CO + H_2$ per mole of injected O_2

The water influx rate, molar fraction, flow rate and heating value of produced species are shown in Fig. 3.9. The water influx rate of outflow channel is an important parameter in a real system. In Fig. 3.9a, the model predicts that the ratio of cavity and channel water influx begins with 1:1 at the early stage of simulations, and tends to be greater than 2:1 for mature cavity. It can be observed in Fig. 3.9a that rock water increases as the cavity interacts with overburden at 34th day, which increases the total water influx rate. The increase in water influx favors steam gasification ($C + H_2O \rightarrow H_2 + CO$) and water gas shift reactions ($CO + H_2O \rightarrow H_2 + CO_2$), which increase the flow rate of H_2 and CO_2 as shown in Fig. 3.9b. However, the amount of CO remains constant as CO is acting as

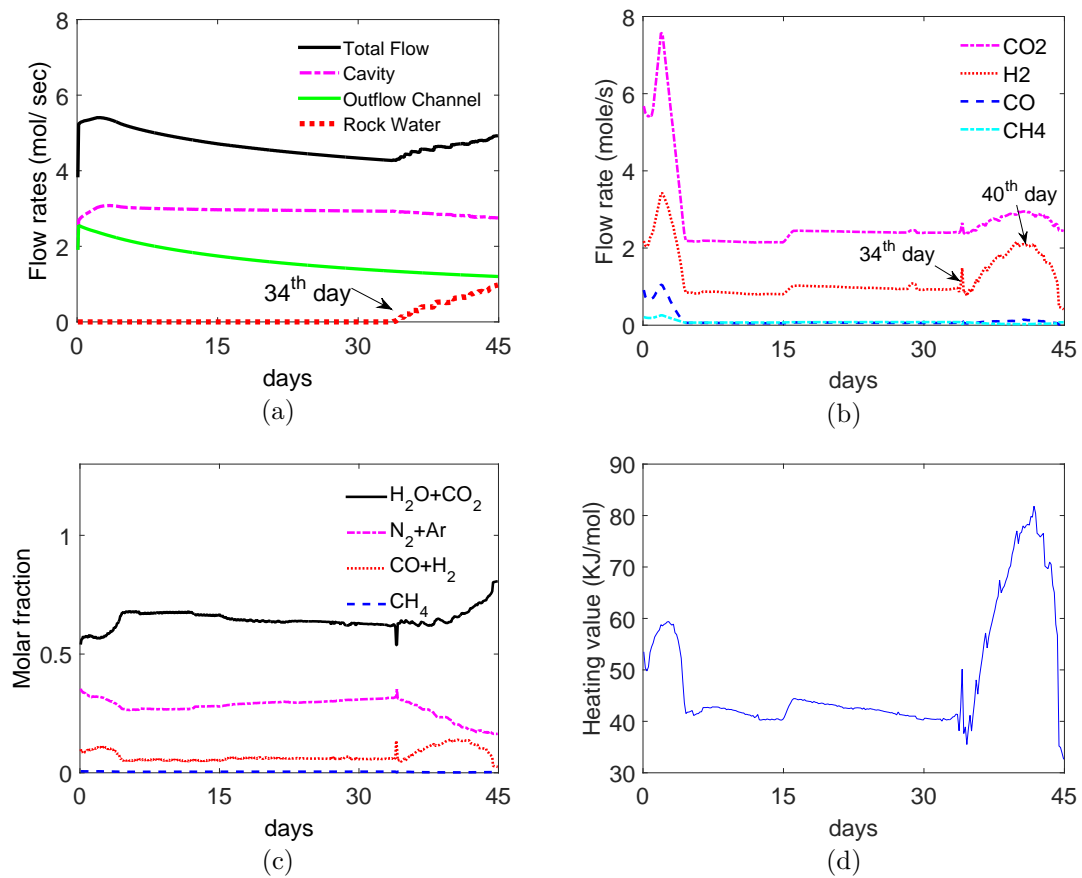


FIGURE 3.9: (a) Water influx rate, (b) produced species rate, (c) composition of product gas, (d) heating value of product gas

a reactant in the latter reaction. As the cavity grows further, char is completely covered by rock and begins to deplete at 40th day, causing reduction in the flow rate of produced gas species. The molar fraction and heating value of the product gas have similar trends as the flow rate of gasification product (H₂ + CO) as shown in Fig. 3.9c and Fig. 3.9d, respectively. The decrease in flow rate, molar fraction and heating value of the product gas near the day 05 is observed, which is due to the lower injection rate of air, which can be seen in Fig. 3.7.

It is observed that the deterioration in heating value of syngas is due to the interaction of cavity with overburden. In Fig. 3.9a, it is observed that total water influx begins to increase at 34th day and at this time the cavity interacts with overburden, as shown in 3.6c. The increase in water disrupts the operation of UCG gasifier and reduces its temperature. Therefore, the decrease in temperature results in the deterioration of heating value.

In this section we have seen that the major factors contributing in the UCG process are the function of cavity growth. Therefore, the prediction of cavity growth has a significant role in determining the overall performance of UCG process. Thus, the parametric study is essential to improve the performance of the UPT field.

3.5 Effect of Operating Conditions on Cavity Growth

In this section, the effect of operating parameters of the UPT field on the volumetric cavity growth and heating value of the product gas has been investigated. The effect of inlet gas composition, O₂ concentration, steam/O₂ ratio (α) and flow rate of injected gas is studied here.

3.5.1 Effect of Inlet Gas Composition

The composition of injected gas is an important parameter in the UCG process. The details of inlet gas composition are given in Table 3.4. In Fig. 3.10a, it can be observed that the cavity growth rate is higher when the injected gas comprises of steam and O₂ instead of dry air. With the inclusion of steam in the injected gas, the amount of N₂ reduces which causes an increase in the concentration of reactant gases. Thus, resulting in a high consumption rate of char. The heating value of product gas for various inlet gas compositions is compared in Fig. 3.10b. It can be seen that the mixture of steam and O₂ in the injected gas gives high heating value as compared to the dry air. The presence of steam in an inlet gas enhances the gasification reaction, resulting in a higher heating value of the product gas. The variation in heating value near the 10th day is due to the cavity interaction with overburden, as explained in the previous section.

It has been shown that the composition of injected gas has significant effect on the heating value of product gas. The mixture of steam and O₂ is best suited to

TABLE 3.4: Composition of Injected gas

| Sr. No. | Injected gas species | Mixture of steam and O ₂ | Dry air |
|---------|----------------------|-------------------------------------|---------|
| 1. | O ₂ | 20% | 21% |
| 2. | H ₂ O | 60% | 0 |
| 3. | N ₂ | 20% | 79% |

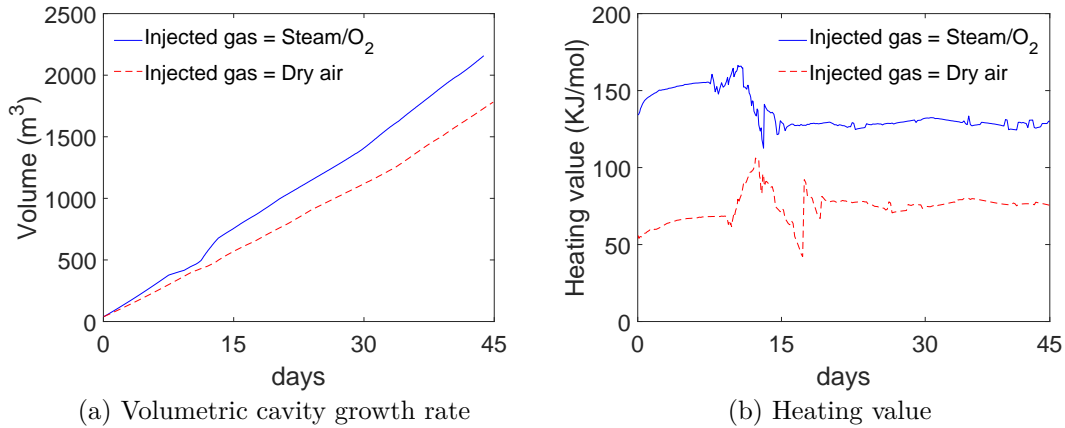


FIGURE 3.10: Effect of inlet gas composition

obtain high heating value from the UCG process. However, an optimum value of steam to O₂ ratio is required.

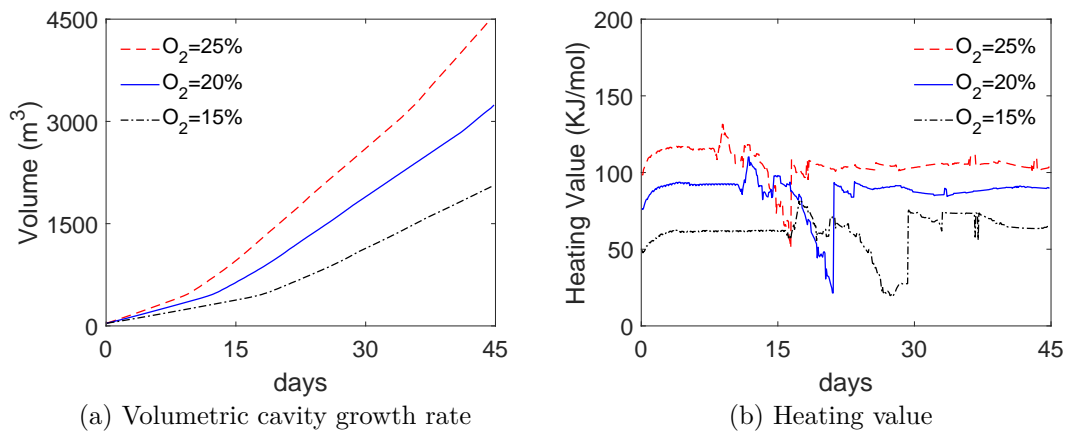
3.5.2 Effect of Varying O₂ Concentration

The effect of injected O₂ concentration with constant steam to oxygen ratio (α) on the volumetric cavity growth and heating value is explored here. The injected gas composition is shown in Table 3.5. The results are illustrated for three different cases in which concentration of O₂ is 25%, 20% and 15%, respectively. To keep α constant, the steam concentration is also varied in accordance with the amount of O₂.

The increase in concentration of O₂ increases the rate of exothermic oxidation reaction, which rises the temperature of the UCG reactor. Besides this, the amount of H₂O also increases, resulting in a higher concentration of reactants. With the increase in total amount of reactants, volumetric cavity growth is expected to increase, which is depicted in Fig. 3.11a. The rise in temperature along with the

TABLE 3.5: Injected gas composition (effect of O₂ concentration)

| Sr. No. | Injected gas species | Case-I | Case-II | Case-III |
|---------|----------------------|--------|---------|----------|
| 1. | O ₂ | 15% | 20% | 25% |
| 2. | α | 1 | 1 | 1 |
| 3. | H ₂ O | 15% | 20% | 25% |
| 4. | N ₂ | 70% | 60% | 50% |

FIGURE 3.11: Effect of varying O₂ concentration

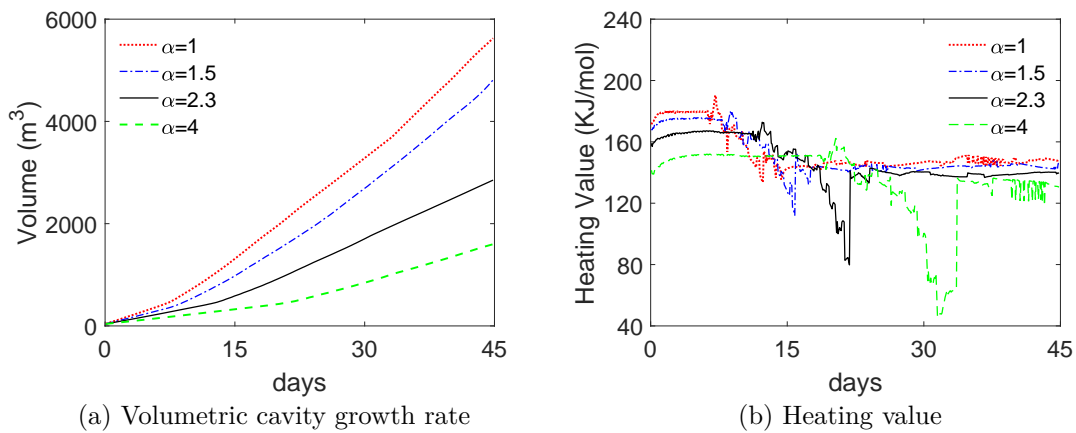
increased concentration of H₂O favors the endothermic gasification and water gas shift reactions, which increases the amount of CO and H₂. Moreover, it can be seen that with decrease in amount of N₂ which is an inert gas, the concentration of reactant gases: O₂ and H₂O increase. Therefore, the decrease in N₂ increases the chemical reactions within the UCG reactor, resulting in the higher heating value of syngas, cf. [19, 53, 109, 110]. Similarly, for lower O₂ concentration the coal conversion and heating value decrease. It can be seen that for the higher concentration of O₂, cavity reaches overburden rock more quickly. In Fig. 3.11b, the effect of cavity interaction with overburden is seen at almost 16th day for case-I, while for the other cases it happens at 11th and 8th day, respectively.

3.5.3 Effect of Varying α

In this section, α is varied to investigate its effect on the volumetric cavity growth and heating value of the product gas. The variation in α can be carried out in two ways [24]:

TABLE 3.6: Composition of Injected gases (effect of α)

| Sr. No. | Injected gas species | Case-I | Case-II | Case-III | Case-IV |
|---------|----------------------|--------|---------|----------|---------|
| 1. | O ₂ | 50% | 40% | 30% | 20% |
| 2. | H ₂ O | 50% | 60% | 70% | 80% |
| 3. | N ₂ | 0% | 0% | 0% | 0% |
| 4. | α | 1 | 1.5 | 2.3 | 4 |

FIGURE 3.12: Effect of varying α

- Keeping the inlet gas flow rate constant, and varying the amount of O₂ and H₂O in inlet gas, as shown in Table 3.6.
- The inlet gas flow rate and amount of O₂ are kept constant, and the amount of H₂O is varied only, as shown in Table 3.7.

Firstly, the analysis is performed for the former case. With the increase in α , concentration of O₂ decreases and amount of H₂O increases. As O₂ is decreased the temperature of the UCG reactor drops, which slows down the rate of endothermic gasification reactions. Hence, it reduces the coal consumption rate, which is shown in Fig. 3.12a. Subsequently, with the increase in α the heating value of syngas also reduces, as shown in Fig. 3.12b, cf. [24, 53].

Now, the analysis is carried out for the second case in which α is varied by changing the amount of H₂O, while amount of O₂ and flow rate are kept constant. As the concentration of O₂ remains constant, therefore, the rate of oxidation reaction does not change. Which in turn maintains a constant temperature of the UCG reactor, therefore, the coal consumption rate is also constant, as shown in

TABLE 3.7: Composition of Injected gases (effect of α)

| Sr. No. | Injected gas species | Case-I | Case-II | Case-III |
|---------|----------------------|--------|---------|----------|
| 1. | O ₂ | 15% | 15% | 15% |
| 2. | H ₂ O | 15% | 30% | 45% |
| 3. | N ₂ | 70% | 55% | 40% |
| 4. | α | 1 | 2 | 3 |

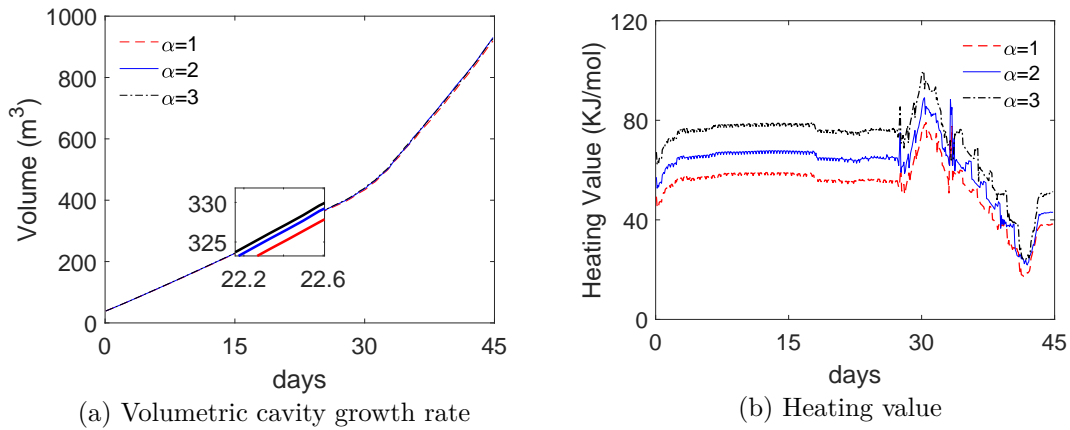
FIGURE 3.13: Effect of varying α

Fig. 3.13a. Moreover, the concentration of H₂O increases with the increase in α , which enhances the water gas shift and gasification reactions, resulting in a higher heating value as shown in Fig. 3.13b, cf. [19, 24, 53]. Moreover, it can also be seen that with the increase in concentration of N₂, the molar fractions of the reactant gases: O₂ and H₂O reduce. The decrease in the amount of reactant gases reduces the chemical reactions within the UCG reactor, resulting in the deterioration of the heating value as observed in Fig. 3.13b. It can also be seen that the cavity interacts with overburden at the same time for all the cases, due to constant coal consumption rate. It is pertinent to mention that the aforementioned phenomena hold for the concentration of steam not exceeding a certain value.

In UCG, steam and O₂ both are the reactant agents and have key role in obtaining the desired heating value of the product gas. A certain amount of H₂O is required for the gasification reaction while on the other hand, excess steam drops the temperature of the reactor due to the endothermicity of the steam gasification reaction. Therefore, an optimal value of α must be chosen to obtain the desired heating value.

3.5.4 Effect of Varying Inlet Gas Flow Rate

The evolution of cavity is also a function of the flow rate of injected gas. To study the effect of flow rate on cavity growth and heating value of product gas, the concentrations of $O_2 = 25\%$ and $\alpha = 3$ are kept constant. The results are discussed for different flow rates of inlet gas. Fig. 3.14 shows that the volumetric cavity growth and heating value of the product gas are directly proportional to the inlet gas flow rate.

The above parametric study shows that the volumetric cavity growth and heating value of the product gas are sensitive to the operating conditions of UCG field. Thus, the operating parameters have vital role in determining the overall performance of UCG process. It can be concluded from the parametric studies that the optimal values of above mentioned operating parameters are required to obtain higher heating value of the product gas for a longer period of time.

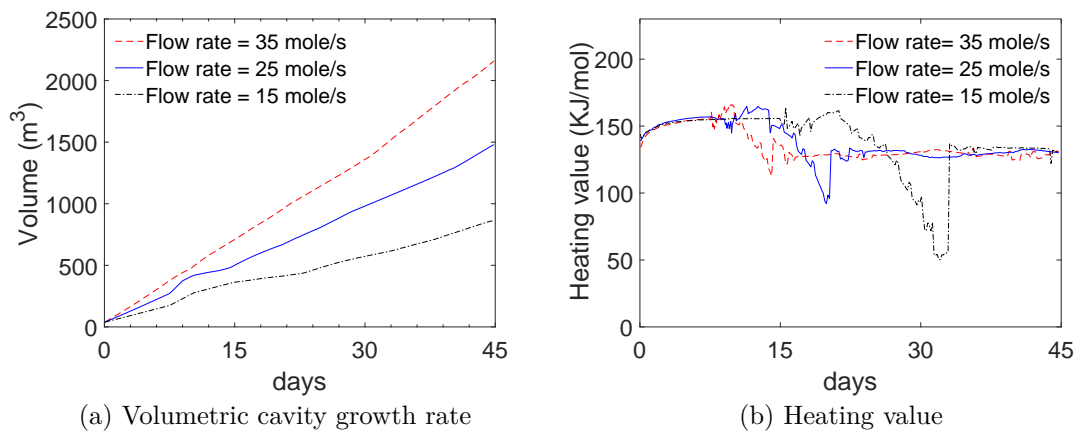


FIGURE 3.14: Effect of varying inlet gas flow rate

3.6 Summary

In this chapter, CAVSIM has been described in detail and used for the UPT field to predict various hydrological and geological conditions such as water influx rate, cavity growth and its interaction with overburden. CAVSIM has been parameterized with the operating parameters of the UPT field and the properties of Lignite

B coal of Thar coal fields. The composition and heating value of syngas predicted by CAVSIM and 1D packed bed model have been compared with the field data of the UPT gasifier. It has been shown that CAVSIM results are better and show a good match with the field data. The cavity evolution at various stages of the UCG process has also been explored. It has been observed that the essential UCG phenomena like char production, water influx, and produced species flow rates and heating value of syngas are greatly affected by the cavity growth. Moreover, the simulation studies have been carried out to investigate the effect of various operating conditions on the volumetric cavity growth and heating value of the product gas. It is concluded that the volumetric cavity growth and heating value of the product gas are sensitive to the various operating parameters of the UPT field.

As CAVSIM is an accurate, comprehensive UCG model, and has already been applied to many UCG fields to predict various complex physical and chemical phenomena of the process. But the complexity of CAVSIM is a major limitation in the design of a model-based control system for the UCG field. Thus, to design a model-based control for the UPT field, a relatively simple UCG model has been formulated which reflects the fundamental dynamics of CAVSIM. The system identification has been used to identify the model, and it is discussed in detail in the next chapter.

Chapter 4

Development of Multi-variable Linear Model for the UPT Gasifier

This chapter accounts for the development of a control-oriented, multi-variable linear model for the UPT field. The selection of a model has a significant importance in the design of a model-based control technique. The capabilities of a model to predict the essential process parameters and ease of control design are important factors in the selection of a model, but there is a trade off involved in it [19]. As described in chapter 3, the CAVSIM is as an essential simulation tool for the UPT field and it is used for the prediction of important process parameters which are not measurable at the site. However, the complexity of the CAVSIM is a major challenge in the designing of a model-based multi-variable control system for the UPT field. Thus, an approximate control-oriented model having sufficient dynamics of the process is required in order to design a model-based control system for the UCG field. In the proposed work, a system identification technique is employed to identify a control-oriented model for the UPT field, which relies on the input-output data of the CAVSIM.

The general work-flow of the system identification approach is discussed in section 4.1. The procedure of system identification technique for the UPT field is discussed in section 4.2. The identified model is analyzed in section 4.3, and finally the chapter is summarized in section 4.4.

4.1 General Work-flow of System Identification

System identification is a mature research area which is mostly based on classical statistical theory. In this technique, the input-output data is used to build the mathematical models of dynamic systems. System identification is a vast subject and it depends on the class of the model to be estimated like nonlinear, linear, parametric, nonparametric and hybrid [111].

The typical work-flow of system identification is illustrated in Fig. 4.1. The process of building a model comprises three main steps; acquiring experimental data, model estimation and validation with the independent data [113]. The data acquired for system identification must reflect the fundamental dynamics of the process. Hence, a careful design of the identification experiment is essential, in which the sampling time and an input signal with suitable spectrum are chosen. It is also necessary to perform some preliminary experiments to acquire the information about the characteristic parameters of systems. After acquiring the data,

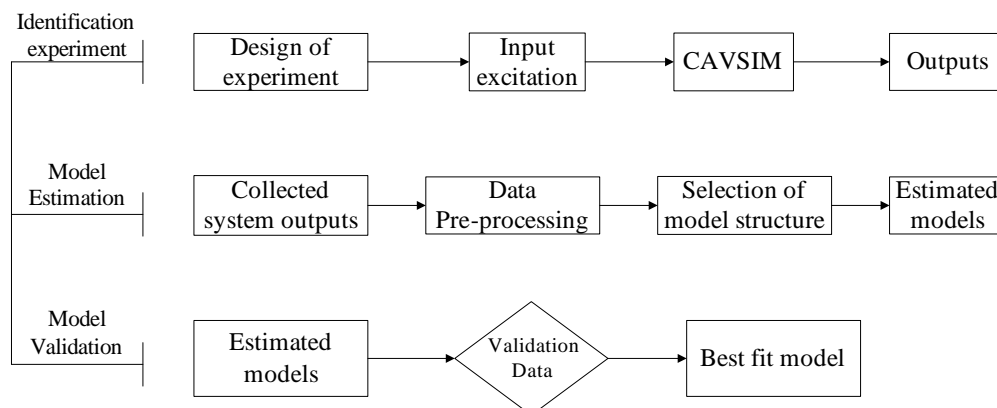


FIGURE 4.1: Typical work-flow of system identification technique [112]

the most challenging task in model estimation is the selection of an appropriate model structure, which includes the selection of variables, model type and order of the model. Moreover, it is often necessary to pre-process the data in order to remove trends, offsets and outliers from the acquired data. Finally, the estimated model is validated with another data to finalize the model [113]. These steps are explained in the subsequent sections

4.1.1 Preliminary Identification Experiments

Prior to design an identification experiment, the information about operating range and the parameters of nonlinear plant such as delays, time constants, static gains and bandwidth is gathered by performing few preliminary experiments [112–114]. The preliminary experiments are briefly discussed as follows:

4.1.1.1 Free-run Experiment

In this experiment, the process is operated in an open-loop configuration without activating input signals. The data acquired from this experiment is used to determine the statistical parameters of output disturbance. The running time is considered long enough such that the statistical properties do not vary significantly. This experiment is primarily based on the measurement of process outputs, and usually conducted on the actual plant [114]. When the input-output data is generated through simulations in which noise is not a concern then this test is not required.

4.1.1.2 Staircase Experiment

This type of experiment has been performed to infer about the linear operating range and static gains. Staircase signals are applied at each input channel individually and outputs are observed. The time interval of each input signal is chosen such that the output must reach to the steady state value. The static

gains are calculated at each step as a ratio of settled output to the input. The selection of operating points has a key role in the identification process, and it is determined by performing series of staircase experiments. The information about system parameters like delays and time constants are obtained by performing step experiments. These experiments are usually the part of staircase experiments.

4.1.1.3 White Noise Experiment

In this experiment, mutually independent white noise signals are applied at each input channel in order to determine the process bandwidth and time delays.

4.1.2 Design of Identification Experiment

After acquiring certain characteristics of a model, the subsequent step is to design and conduct an identification experiment. The input-output data sets are generated by this experiment, which are required for model estimation and validation. The data acquired for system identification must reflect the fundamental dynamics of the process. Hence, a careful design of the identification experiment is essential, which mainly includes the selection of an excitation signal with the design parameters like switching time, experiment length and sampling time. The input signal must satisfy the property of persistent excitation i.e. its bandwidth should cover the range of all frequencies of interest [112–114]. The perturbed signals such as step, random binary sequence (RBS), pseudo random binary sequence (PRBS), white noise, multi-sine and swept sin (chirp) are typically used for the identification of unknown systems. These excitation signals have flat power spectrum band within the user specified frequency band. In [115], authors have shown that the construction of advanced dedicated signals is a challenging task, and the most commonly used signals for system identification are step and PRBS signals. In the identification process, the data acquisition from an actual plant is the foremost challenge due to the experimental and economical constraints associated with the conduction of field trials [113, 116, 117].

4.1.3 Model Estimation

The selection of model structure is an important step in model estimation, which includes the selection of variables, model type and order of model [113]. However, it is often necessary to remove outliers, trends and offsets from the estimated data prior to perform model estimation.

4.1.3.1 Data Pre-processing

In this section, various data pre-processing techniques are briefly discussed below.

1. Removal of Outliers

In an industrial process loose electrical contacts, power failure, sensor noise and other imperfections cause unexpected peaks in the measured outputs. The spikes can have large amplitude and energy contents as compared to the actual signals, therefore, they may have a considerable impact on the model estimation. The outliers are removed by clipping the peaks and interpolation is used to replace the output slots.

2. Trend correction

The drifting of output is a general phenomena in an industrial process, in which the output tends to drift slowly with time. Although it can be easily compensated by a feedback controller but it affects the accuracy of identified model. The removal of such trends is called de-trending and it can be performed in two ways. The first approach is to use a low-pass filter in order to estimate the trends. The selection of cut off frequency is based on the process knowledge. In the second approach a band-pass filter is used with a bandwidth of the process. The presence of trends and drifts in the estimated data may result in a poor estimation of the model, as they do not average out due to their low frequency behavior. Thus, this data preprocessing operation helps in identifying a more accurate linear model.

3. Offset correction

The offset is present in the acquired data, as the system identification has been performed around a certain operating point. In order to capture the dynamics of the process, these biases have been removed by subtracting the mean of signals.

4.1.3.2 Determining Model Structure and Order

There are variety of linear model structures available, such as transfer function, state-space, process, impulse and frequency response models. Although these model structures are equivalent to each other and can be transformed from one form to another, but the quality of an identified model is strongly influenced by the selection of a model structure. As each model structure has distinct estimating algorithms and methods to represent the relationship between inputs, outputs and non-deterministic processes. The commonly used estimation algorithms are prediction error minimization (PEM) and N4SID. The model order can be determined by using a Hankel singular value plot.

4.1.4 Model Validation

After the model estimation, the next step is to validate the model with different data sets that is not used in the model estimation and this process is called cross validation. The simulation error and residual analysis are the most commonly used methods for model validation. It is quite often to use the confidence interval to show that the validation results are within the acceptable range or tolerance.

4.2 System Identification for the UPT Field

It is a common practice to use an approximated linear model for the given nonlinear process. In industry, the nonlinear model formulation of a plant is a challenging

task, and in some cases, it is even not possible to drive the nonlinear model of the plant. The two most commonly used methods to determine the nonlinear model are the first-principle based models and data-driven modeling techniques. The first-principle based models are based on the physical laws involved in the industrial process, and it is a highly expensive process in terms of cost and time. Even, if the nonlinear model is formulated successfully, it would be highly complex and cannot be readily used for the development of a closed-loop system. While the snag in data-driven modeling approaches like bilinear identification or neural networks lies in the lack of user oriented identification techniques and generality. Most of the control designs based on nonlinear process models, resulting in a highly complex control system that requires large computational resources and cost. On the contrary, the low cost and control oriented linear models can be easily obtained by employing well established linear model identification techniques. Hence, a multi-variable linear model is identified to develop a control system for the UPT field.

The conduction of identification experiment on the actual plant is a formidable task due to the experimental and economical constraints associated with the conduction of field trials [113, 116, 117]. In practice, there are some limitations on the operating range of the plant, input signals and the resulting outputs, and it is time consuming as well. UCG is a very slow process and the process variables like inlet gas flow rate, pressure and H_2O/O_2 have to be maintained within the safe operating range. Therefore, practically, it is not feasible to perform identification experiments at the UPT site. For this purpose, CAVSIM simulator is used which has already been validated with the field data of UPT, as described in chapter 3. The steps followed in employing the system identification technique to determine a multi-variable linear model for the UPT field are explained below.

- i) Initially, some preliminary experiments like staircase and step experiments are performed to infer about the linear operating range, static gains and delays. In UCG process, various physical phenomena are occurring over a wide range of characteristic time and length scales. These phenomena are

highly complex and nonlinear, therefore, the linear model for UCG field can only be valid along a certain operating points. The selection of operating points outside the linear range of the process may cause large modeling errors, resulting in a poor estimation of the model [114]. The linear operating range of UCG is determined by a series of staircase experiments. For any UCG site, the available manipulating variables are only the inlet gas flow rate and steam to oxygen ratio ($\text{H}_2\text{O}/\text{O}_2$). As described in section 3.5.3, the $\text{H}_2\text{O}/\text{O}_2$ can be varied by either varying the concentration of O_2 and H_2O simultaneously or only the concentration of H_2O is varied while amount of O_2 is kept constant. Here, in all the identification experiments, O_2 is kept constant and the concentration of H_2O is varied. The heating value and the flow rate of syngas are the only measurable outputs at the UPT field. After performing a series of staircase experiments, the linear operating range of inputs and outputs is indicated in Fig. 4.2. The linear operating range is determined by calculating the change in outputs for the corresponding step-change in inputs, and is given as

$$\begin{aligned} 0.33 \leq u_1 \leq 1, \quad 6.5 \leq u_2 \leq 7.5, \\ 82 \leq y_1 \leq 112, \quad 16 \leq y_2 \leq 18, \end{aligned} \quad (4.1)$$

where u_1 (steam to oxygen ratio ($\text{H}_2\text{O}/\text{O}_2$)) and u_2 (inlet gas flow rate (mol/s)) represent inputs of the system. While y_1 , y_2 are the outputs i.e. heating value (KJ/mol) and flow rate (mol/s) of syngas, respectively.

The step responses of UCG are shown in Fig. 4.3, and it is found that there is no time delay between the input and output. The rise times and time constants determined by the step responses are summarized in Table 4.1.

TABLE 4.1: Parameters obtained from step response

| Inputs | Outputs | Time constant $\tau(s)$ | Rise time $t_R(s)$ |
|--------|---------|-------------------------|--------------------|
| u_1 | y_1 | 20.83 | 34.5 |
| | y_2 | 19.03 | 31.1 |
| u_2 | y_1 | 20.03 | 30.3 |
| | y_2 | 21.04 | 31.6 |

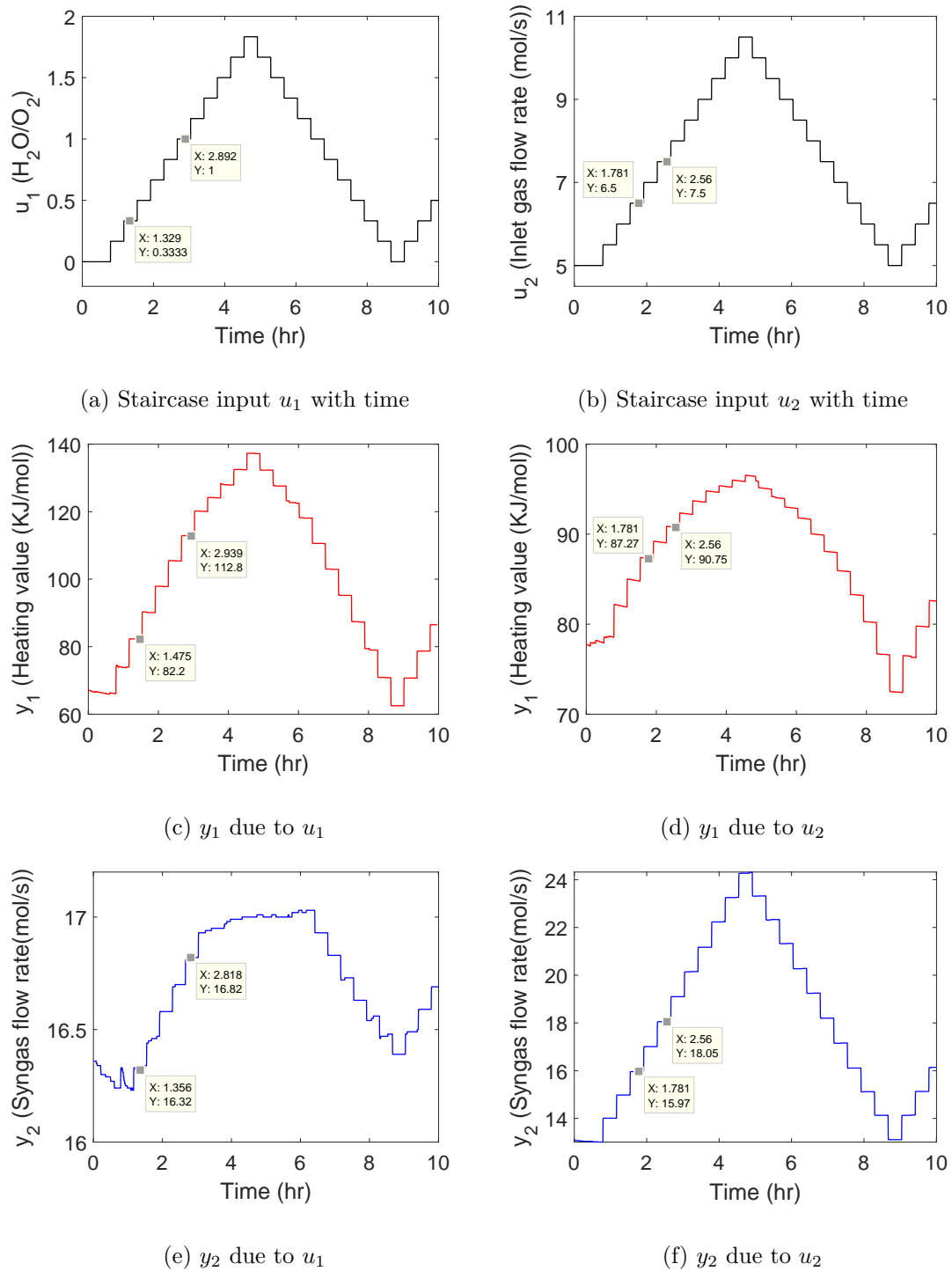


FIGURE 4.2: UCG response for staircase inputs

- ii) A PRBS signal has been used as an excitation signal and the design procedure is described in Table 4.2. A PRBS is a periodic signal, which switches in a certain fashion between two levels L_- and L_+ , within a user specified frequency band. The bandwidth $[\omega_l \ \omega_H]$ of input signal for multi-variable

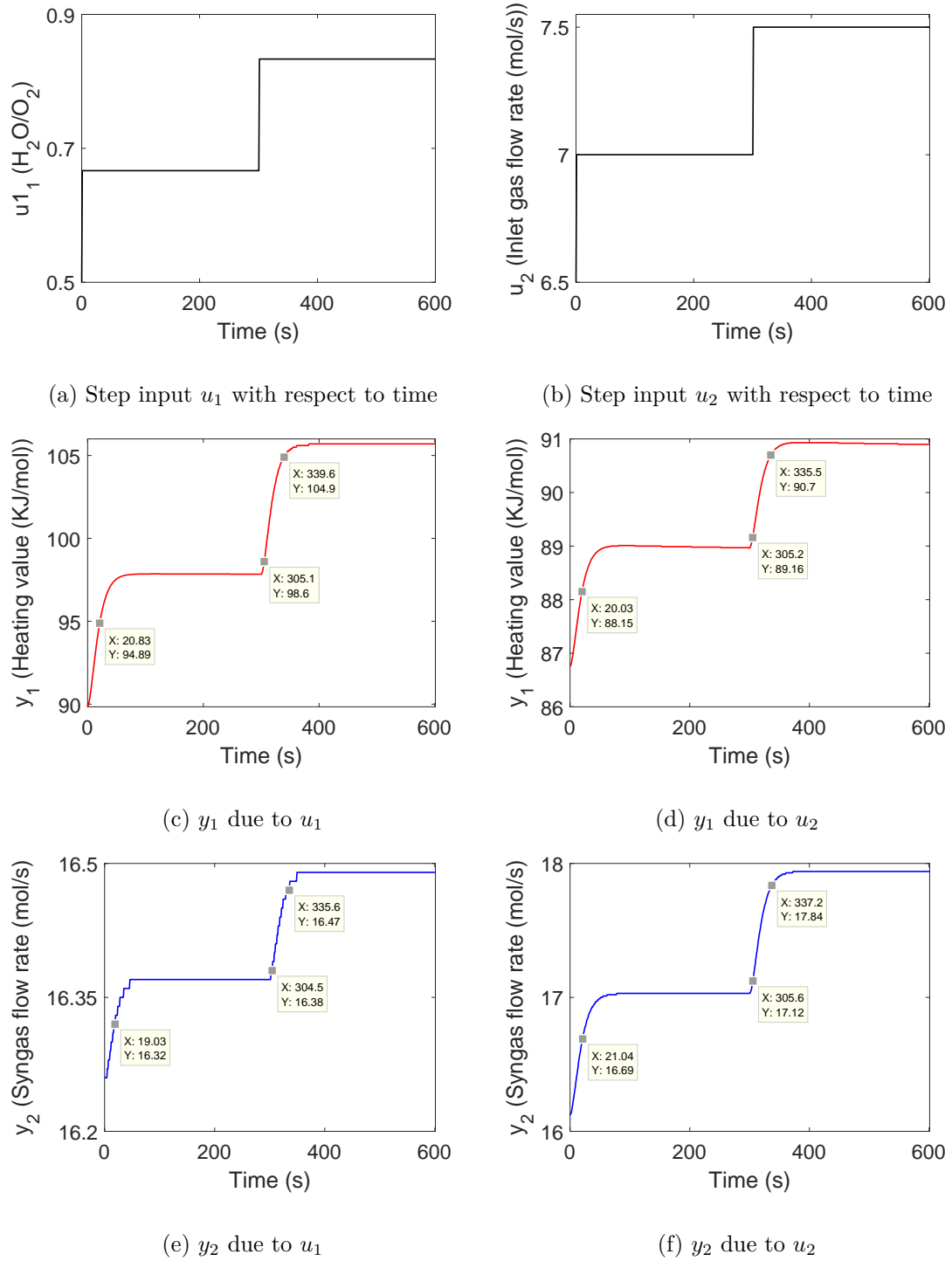


FIGURE 4.3: Step response of UCG

system is defined as

$$\omega_l = \frac{1}{\beta\tau_H} \leq \omega \leq \omega_H = \frac{\xi}{\tau_l}, \quad (4.2)$$

where τ_H and τ_l are the highest and lowest time constants of the process,

TABLE 4.2: Design parameters for PRBS

| Parameters | | Values |
|--|---------------|--------|
| Lowest dominating time constant | $\tau_l(s)$ | 20.03 |
| Highest dominating time constant | $\tau_H(s)$ | 21.04 |
| Number of inputs | p | 1 |
| Closed-loop response parameter | ξ | 2 |
| Settling-time parameter | β | 3 |
| Switching time | $T_{sw}(s)^*$ | 27 |
| Delay time | $t_d(s)^*$ | 3.8 |
| Number of bits in PRBS sequence of length $N_s = 2^{n_r} - 1$ | n^{r^*} | 4 |

*Designed parameters, calculated from (4.3) and (4.4).

respectively, obtained from the step experiment; ξ is the ratio of open-loop to closed-loop time constants; $\beta\tau_H$ is the settling time of open loop system [112]. The number of shift registers (n_r) and the switching time T_{sw} are the important parameters to characterize the generated signal. The sequence repeats itself after $N_s T_{sw}$ units of time, where $N_s = 2^{n_r} - 1$. In [118], authors have presented the guidelines to choose the switching and sampling time of PRBS, and experiment length as

$$\frac{2.8\tau_l}{\xi} \leq T_{sw} \leq \frac{2\pi\beta\tau_H}{N_s}, \quad (4.3)$$

$$N_s = 2^{n_r} - 1 = \max\left(\frac{2\pi\beta\tau_H}{T_{sw}}, pt_d\right), \quad (4.4)$$

$$t_d = \frac{5\tau_H}{T_{sw}}, \quad t_s = T_{sw}/4,$$

where p is the number of inputs, t_s is the sampling time and t_d is the delay time. The input-output data sets required for the system identification of multiple-input, multiple-output (MIMO) system can be generated by applying all input signals simultaneously or separately. When all the input PRBS signals are applied simultaneously then each input must be delayed or shifted relative to the previous input by the delay time t_d in order to ensure that the input signals remain statistically uncorrelated. These types of signals are difficult to generate and make the task of system identification more complex. Thus, in this work separate PRBS is used for each input channel to generate the input-data sets, and are shown in Fig. 4.4. The designed

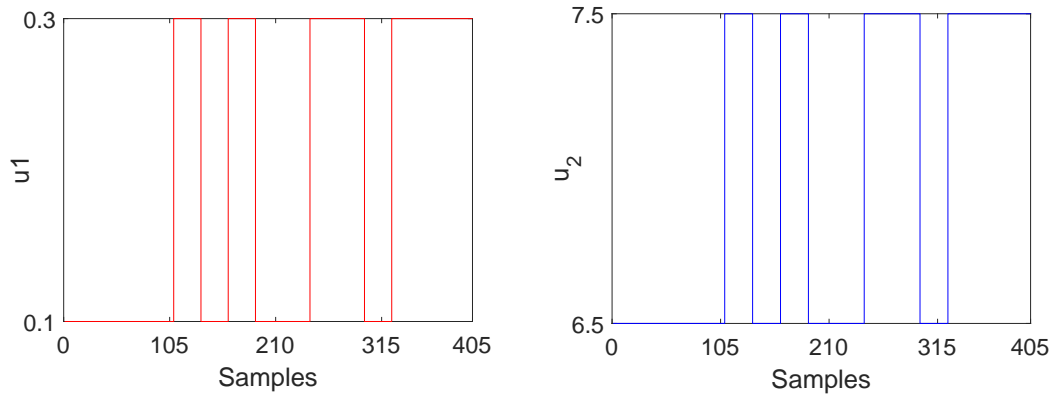
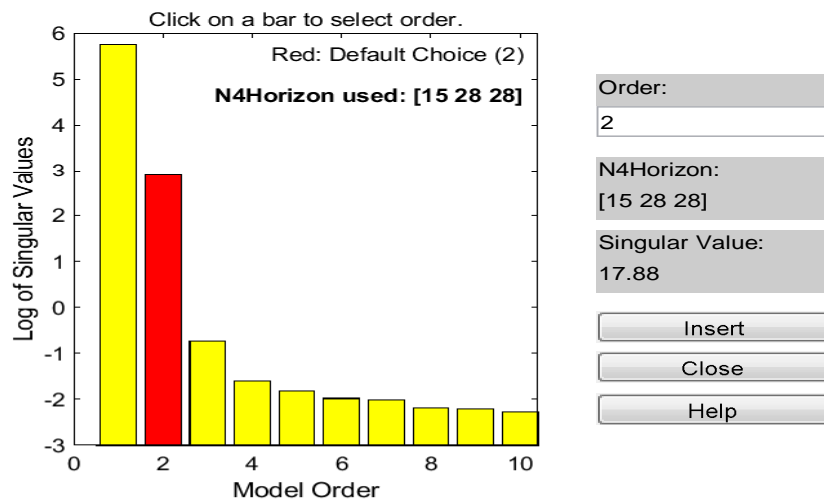


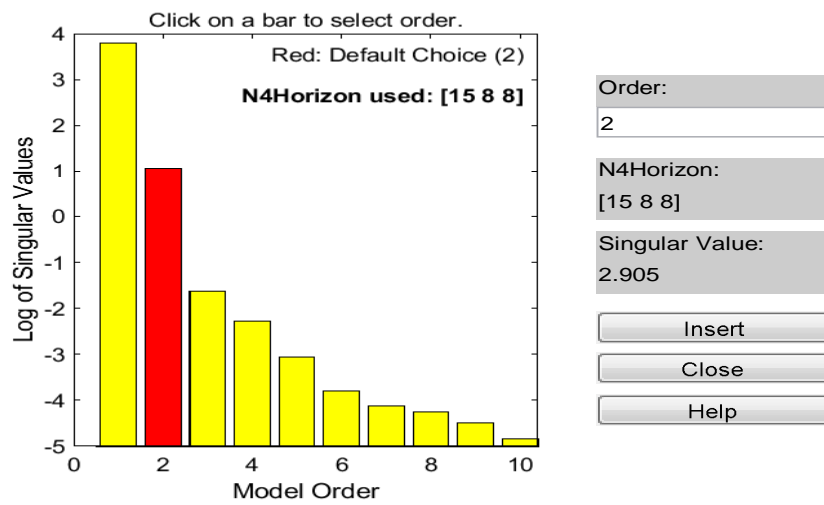
FIGURE 4.4: Designed PRBS signals

PRBS input signals having $T_{sw} = 27s$, $N_s = 15$ and maximum experiment length $N_s T_{sw} = 405$ samples, while the amplitude levels are defined on the basis of allowed linear operating range of each input.

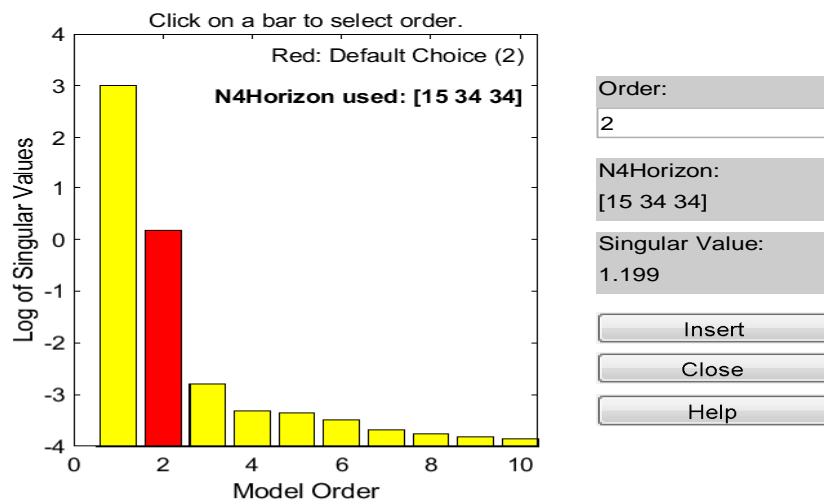
- iii) The data de-trending has been performed as a pre-processing step to estimate the model. The system identification toolbox of MATLAB is used to identify the linear model. A number of different models like transfer function, state-space and process models are tried, and the best fit results are obtained from state-space model structure. The model is estimated by using N4SID estimation method. It is a non-iterative, subspace method and can be used for both time-domain and frequency-domain data. The model order is determined by evaluating a range of orders simultaneously. While the best order of the model is chosen from a Hankel singular value plot, as shown in Fig. 4.5. The plot indicates the relative contribution of each state to the input-output behavior of the model. It can be seen that the states 1 and 2 have significant contribution, therefore, a second order model is selected.
- iv) The model has been validated by using the simulation error and residual analysis methods, which are briefly discussed below.
 - a) **Simulation error:** The independent data sets for estimation and validation is obtained by splitting the data set into two parts. The quality of an identified model is determined by a metric called best fit, and it



(a) Selection of model order for g_{11}



(b) Selection of model order for g_{12}



(c) Selection of model order for g_{22}

FIGURE 4.5: Hankel singular value plots for the selection of models order

is computed as

$$\text{Best fit} = \left(1 - \frac{|y - \hat{y}|}{|y - \bar{y}|} \right) \times 100\%, \quad (4.5)$$

where y is the measured output, \bar{y} is the mean of y and \hat{y} is the model predicted output. As determined earlier, the maximum identification experiment length is about 405 samples. The first 205 samples of input-output data sets are used for the model estimation and remaining 200 samples are used for the model validation. In Fig. 4.6, the outputs of linear model are compared with the validation data for each input. The outputs are denoted by y_{ij} , where $i = 1, 2$ represents the outputs and $j = 1, 2$ denote the corresponding inputs. As it is found in preliminary experiments that u_1 has negligible impact on y_2 , therefore, y_{21} has been ignored. It is found that the best fit results of each $y_{i,j}$ are 92.9%, 96.6% and 97.2%, respectively.

- b) **Residual Analysis:** The residual analysis is another important metric to determine the quality of an identified model, which provides an insight about the model predictions [119]. The residuals are one-step-ahead prediction error, representing the portion of the validation data which is not described by the model. The residual analysis comprises of two tests: the independent test and the whiteness test. In the independent test, a cross-correlation between residuals and input signal is determined. Moreover, it is essential that the residuals of each output must be uncorrelated with the past input signals in order to get better prediction results. Mathematically,

$$R_{\epsilon,u}(\tau_o) = \frac{1}{N} \sum_{t=1}^N \epsilon(t)u(t - \tau_o), \quad (4.6)$$

where $\epsilon(t)$ represents residuals. Large values of cross-correlation indicate that the model fails to describe how the output is formed from the corresponding input. For instance, a peak outside the confidence

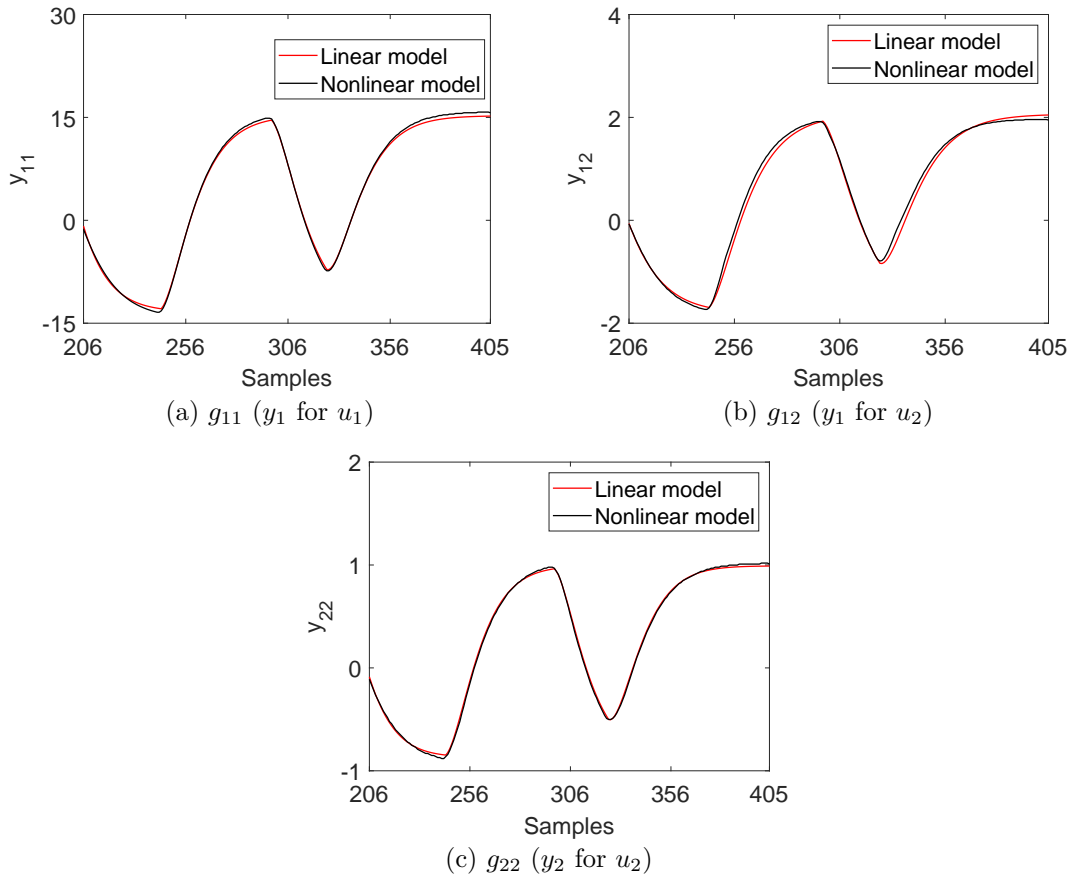


FIGURE 4.6: Comparison of linear and nonlinear models using simulation error method

interval for lag τ_o means that the output $y(t)$ originates from the input $u(t - \tau_o)$ is not properly described by the model. The Gaussian distribution is used to find the confidence interval. In the whiteness test, residual auto-correlation is found and it must be white for a good identified model. The mathematical representation of the whiteness test is given as

$$R_\epsilon(\tau_o) = \frac{1}{N} \sum_{t=1}^N \epsilon(t)\epsilon(t - \tau_o). \quad (4.7)$$

This test is based on the assumption that the $\epsilon(t)$ has a zero-mean white noise. This implies that if $\epsilon(t)$ is white noise then its covariance function is zero except at $\tau_o = 0$. However, a peak outside the confidence interval for a lag ($\tau_o \neq 0$) indicates that the residue has a pattern and it is

not white noise. The residual analysis of each model is illustrated in Fig. 4.7. It can be observed that the autocorrelation of residuals of each output and the cross-correlation between output residuals and each input remain within the confidence interval of corresponding estimates.

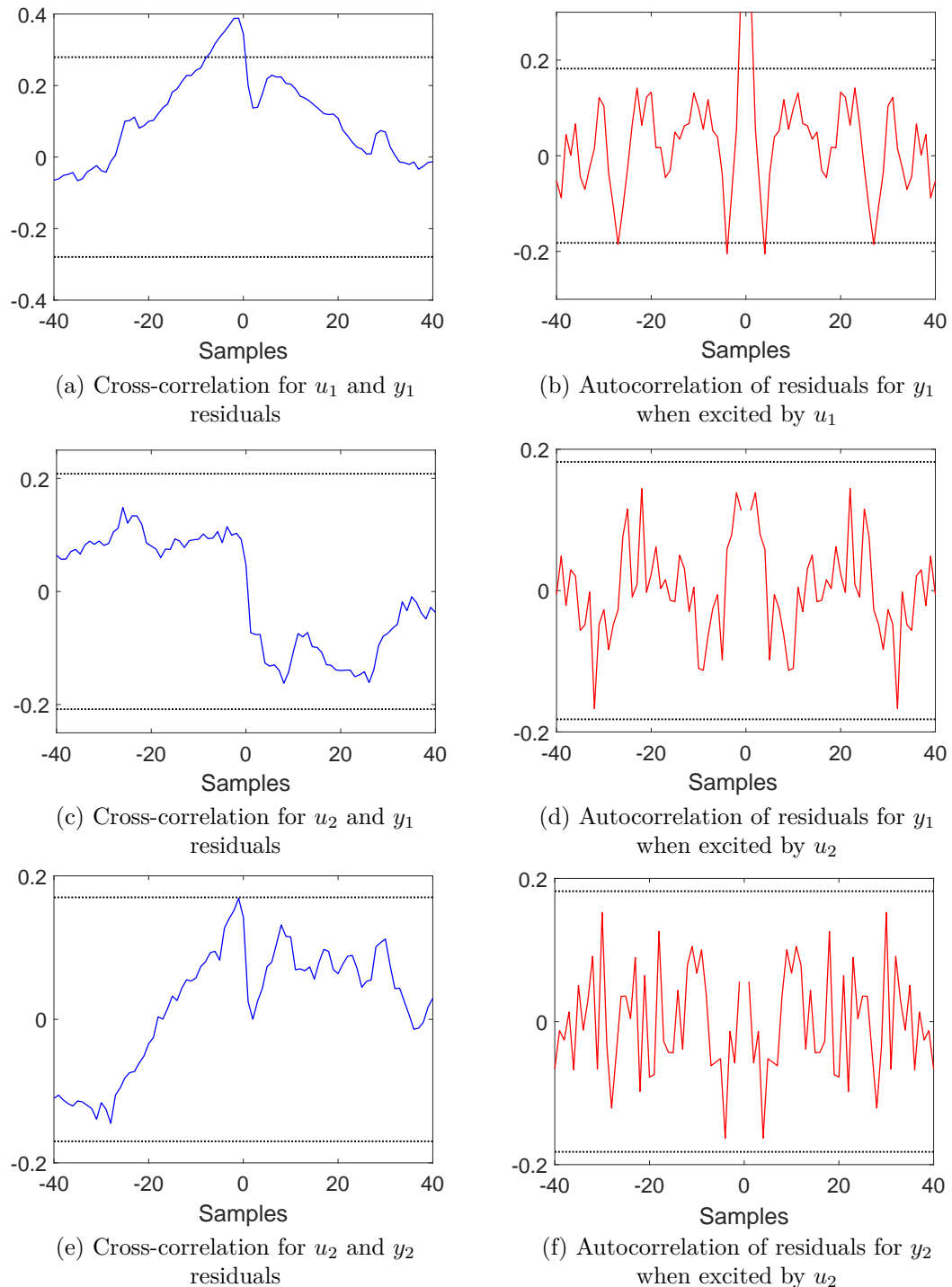


FIGURE 4.7: Comparison of linear and nonlinear models using residual analysis

4.3 Analysis of Linear Model

The identified state-space model with minimum realization of the system is given as

$$\dot{\mathbf{x}} = A\mathbf{x} + B\mathbf{u}, \quad (4.8)$$

$$\mathbf{y} = C\mathbf{x}, \quad (4.9)$$

where $\mathbf{x} \in \mathfrak{R}^{n \times 1}$, $\mathbf{u} \in \mathfrak{R}^{m \times 1}$, $\mathbf{y} \in \mathfrak{R}^{p \times 1}$, $A \in \mathfrak{R}^{n \times n}$, $B \in \mathfrak{R}^{n \times m}$, $C \in \mathfrak{R}^{p \times n}$, and $n = 6, m = p = 2$. As the identification process solely depends on the input-output data sets and not on the physical laws. Therefore, the states in (4.8) and (4.9) do not represent any physical parameter / quantity of the UCG process. The state-space matrices are given as

$$A = \begin{bmatrix} -0.2 & -0.08 & 0 & 0 & 0 & 0 \\ 0.12 & 0 & 0 & 0 & 0 & 0 \\ 0 & 0 & -0.19 & -0.07 & 0 & 0 \\ 0 & 0 & 0.12 & 0 & 0 & 0 \\ 0 & 0 & 0 & 0 & -0.20 & -0.08 \\ 0 & 0 & 0 & 0 & 0.12 & 0 \end{bmatrix}, B = \begin{bmatrix} 4 & 0 \\ 0 & 0 \\ 0 & 0.5 \\ 0 & 0 \\ 0 & 0.5 \\ 0 & 0 \end{bmatrix},$$

$$C = \begin{bmatrix} 0.45 & 2.92 & 0.09 & 0.56 & 0 & 0 \\ 0 & 0 & 0 & 0 & 0.039 & 0.318 \end{bmatrix}.$$

The transfer function matrix of (4.8) and (4.9) is

$$\begin{bmatrix} y_1 \\ y_2 \end{bmatrix} = \begin{bmatrix} g_{11}(s) & g_{12}(s) \\ g_{21}(s) & g_{22}(s) \end{bmatrix} \begin{bmatrix} u_1 \\ u_2 \end{bmatrix}, \quad (4.10)$$

where,

$$g_{11}(s) = \frac{1.799s + 1.458}{s^2 + 0.2s + 0.0102}, \quad g_{12}(s) = \frac{0.04659s + 0.03473}{s^2 + 0.1915s + 0.008979},$$

$$g_{21}(s) = 0, \quad g_{22}(s) = \frac{0.01951s + 0.0199}{s^2 + 0.1993s + 0.01071}.$$

4.3.1 Plant Scaling

Plant scaling has a significant importance in the multi-variable systems which have different physical quantities. It helps the control engineer to make a decision about the desired performance of the system at the onset of controller design [120]. For this purpose, a decision is made about the expected change in magnitudes of external signals like references, disturbance and measurement noise, and maximum allowed deviation of each input and output around the nominal point. The unscaled linear model of the UCG system is given in Eq. 4.11.

$$\tilde{\mathbf{y}} = \tilde{G}\tilde{\mathbf{u}} + \tilde{G}_{d_i}\tilde{\mathbf{d}}_i, \quad \tilde{\mathbf{e}} = \tilde{\mathbf{y}} - \tilde{\mathbf{r}}. \quad (4.11)$$

where $(\tilde{\cdot})$ is used to represent the variables in their actual unscaled units. The scaling is performed by dividing each variable with its maximum allowed variation around the nominal point. Let $\tilde{u}_{j,max}$, $\tilde{d}_{i,max}$, $\tilde{r}_{k,max}$ and $\tilde{e}_{k,max}$ denote the maximum allowed change in input \tilde{u}_j , input disturbance \tilde{d}_i , reference \tilde{r}_k and control error \tilde{e}_k , respectively. As the variables \tilde{y} , \tilde{r} and \tilde{e} have the same units, therefore, same scaling factor i.e. maximum control error (\tilde{e}_{max}) is applied to each variable. The unscaled and scaled quantities such as inputs, disturbances and control error are related by introducing the scaling matrices D_u , D_{d_i} and D_e , respectively.

$$\tilde{\mathbf{u}} = D_u\mathbf{u}, \quad \tilde{\mathbf{d}}_i = D_{d_i}\mathbf{d}_i, \quad \tilde{\mathbf{r}} = D_e\mathbf{r}, \quad \tilde{\mathbf{y}} = D_e\mathbf{y}. \quad (4.12)$$

In (4.1), the nominal values of y_1 , y_2 , u_1 and u_2 are 97, 17, 0.66 and 7.0, respectively. The maximum allowed variation around the nominal points of each output and each input is ± 15 , ± 1 , ± 0.33 and ± 0.5 , respectively. Hence, the elements of scaling matrices become

$$D_u = \begin{bmatrix} 0.33 & 0 \\ 0 & 0.5 \end{bmatrix}, \quad D_{d_i} = \begin{bmatrix} 0.1 & 0 \\ 0 & 0 \end{bmatrix}, \quad D_e = \begin{bmatrix} 15 & 0 \\ 0 & 1 \end{bmatrix}. \quad (4.13)$$

The scaled model given in (4.15) is obtained by introducing the scaled variables into (4.11).

$$G = D_e^{-1}\tilde{G}D_u, \quad G_{d_i} = D_e^{-1}\tilde{G}_{d_i}D_i, \quad (4.14)$$

$$\mathbf{y} = G\mathbf{u} + G_{d_i}\mathbf{d}_i, \quad \mathbf{e} = \mathbf{y} - \mathbf{r}. \quad (4.15)$$

4.3.2 Interaction Analysis

Generally, the multi-variable systems have complicated cross coupling characteristics, which makes the control design task challenging. The interaction in control loops can disrupt the performance of closed-loop system, and may also cause the stability problems [120]. The condition number and relative gain array (RGA) are the most common measures to quantify the directionality and interaction in multi-variable systems.

4.3.2.1 Condition Number

The condition number ($\gamma(G)$) is used to quantify the degree of directionality in multi-variable systems, and also indicates their sensitivity to the uncertainties. It is the ratio of maximum and minimum singular values of the system, and given as

$$\gamma(G) \triangleq \frac{\bar{\sigma}(G)}{\underline{\sigma}(G)}, \quad (4.16)$$

where $\bar{\sigma}(G)$ and $\underline{\sigma}(G)$ are the maximum and minimum singular values of G , respectively. The small condition number indicates that the system is well-conditioned, which means that the uncertainties do not have strong impact in such systems. As $\gamma(G)$ strongly depends on the plant scaling, therefore, proper plant scaling is required to obtain a well-conditioned system. The frequency response of $\gamma(G)$ is shown in Fig. 4.8. It can be seen that the $\gamma(G)$ has been reduced significantly due to scaling, resulting in a well-conditioned system.

4.3.2.2 Relative Gain Array (RGA)

The analysis of RGA is one of the systematic methods to quantify the input–output interactions in multi-variable systems. In an interactive system, the relative gain is used to find the change in gain of one loop when other loops are closed. The degree of interaction is determined by the steady state gains, and the individual RGA elements indicate the impact of a specific input to a particular output.

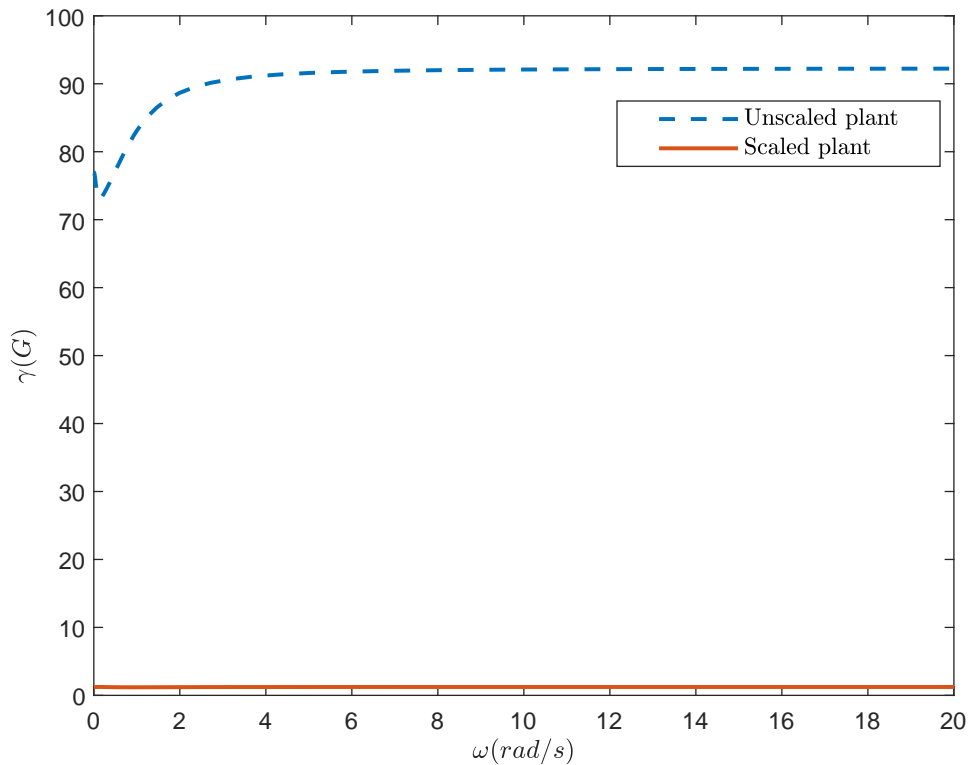


FIGURE 4.8: Frequency response of condition number

Mathematically, RGA is defined as

$$\text{RGA}(G) = \Lambda(G) = G \times (G^{-1})^T, \quad (4.17)$$

where \times represents element-by-element multiplication. Moreover, it can be used to predict the sensitivity to uncertainty and modeling errors. The large RGA-elements around the crossover frequency indicate that the such plants are highly sensitive to the input uncertainties and are difficult to control. These uncertainties may be caused by neglected or uncertain dynamics of the actuators. It is independent of plant scaling, and it also indicates the presence of right-half plane (RHP) zeros in the plant. When any change in the sign of an RGA-elements occurs due to change in frequency, then it implies that the RHP zero in G or any subsystem of G exists. The frequency response of RGA is shown in Fig. 4.9. The off-diagonal elements remain at zero in the entire range of frequency, so $\Lambda(s) = I$. Thus, it is evident that the system has less sensitivity to the input uncertainties

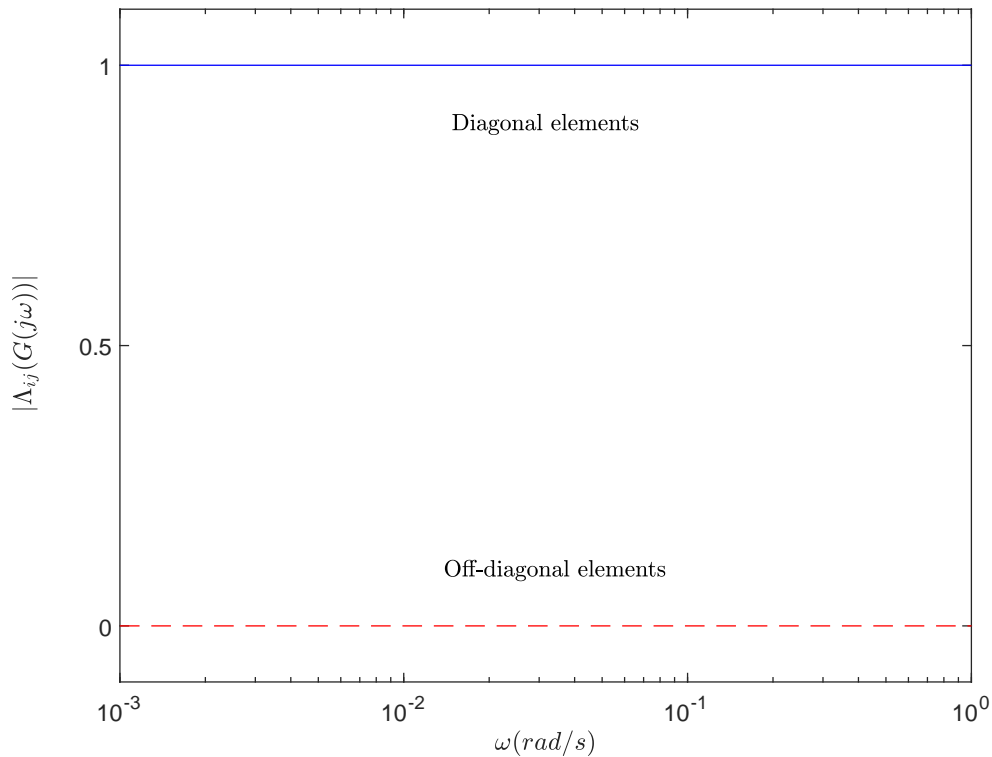


FIGURE 4.9: Frequency response of RGA

and no RHP zero exists in the identified model. Moreover, RGA can be used to pair inputs-outputs in the design of a decentralized control system. The frequency response of RGA elements in Fig. 4.9 depicts the dominance of diagonal elements. Thus, the input u_i can be paired with the corresponding output y_i .

4.3.3 Model Uncertainty

There are numerous sources of model uncertainty, such as the modeling inaccuracies due to linearization, variation in the parameters of linear model due to nonlinearities or changes in the operating parameters, neglected dynamics in modeling and imperfections of measuring devices.

The parameters confidence interval in transient and frequency response of the identified model are used to visualize the modeling uncertainties. The value of parameter confidence interval close to zero indicates that the parameter is too small or equal to zero, which helps in performing model reduction without the loss

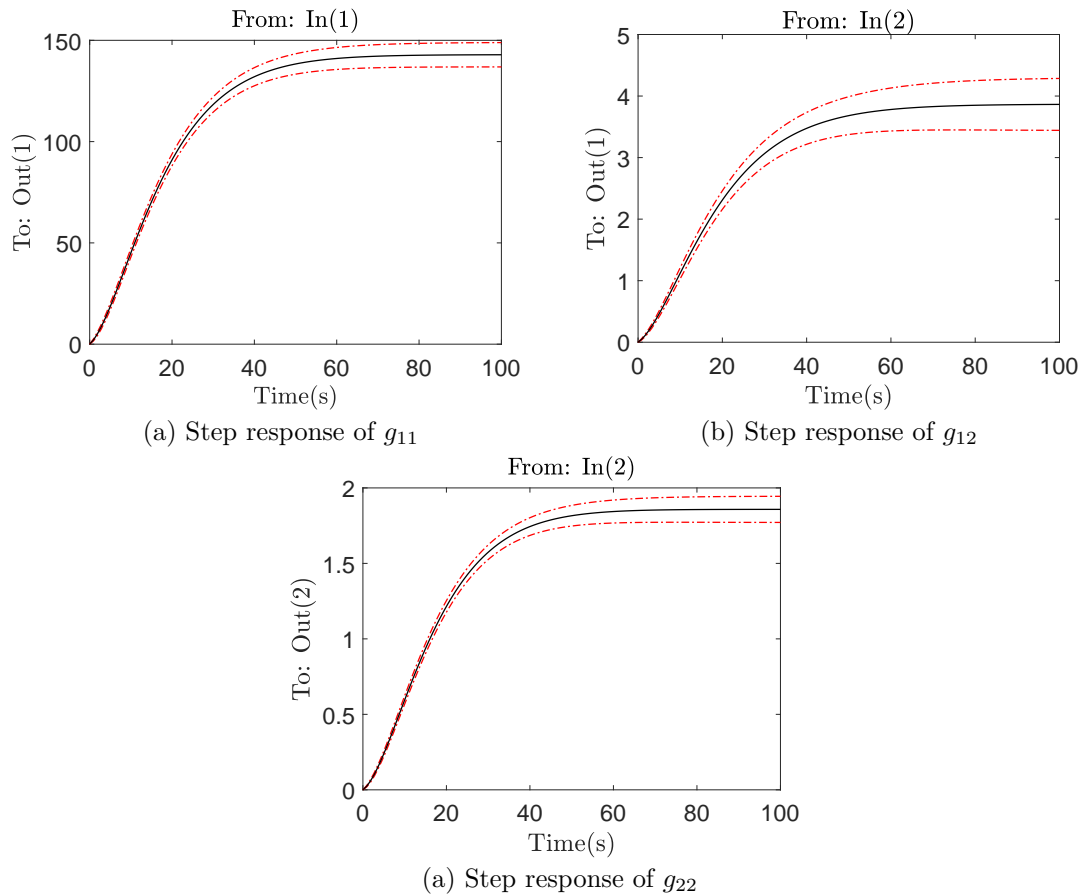


FIGURE 4.10: Step responses with uncertainty bounds

of fundamental dynamics of the model. The step responses of the identified model are shown in Fig. 4.10. The uncertainties are represented as parameters confidence interval, and it is evident in the step responses that the transition stage is more certain than the steady state. The frequency responses with uncertainty bounds of the identified model are shown in Fig. 4.11. It can be seen that the responses are more uncertain at low frequencies. The uncertainties in steady state gain of g_{11} , g_{12} and g_{22} are $\pm 4.2\%$, $\pm 10.8\%$ and $\pm 4.6\%$, respectively. The low values of uncertainties indicate that the identified model is reliable, and can be used for the design of control system.

The insight about dynamic properties of estimated models like response times, delays and static gains are obtained by analyzing transient response of the models. While the frequency response of identified model gives insight about the dynamic parameters like resonances, frequency dependent gains and phase shifts, and stability margins. It also contains information about the bandwidth of the process.

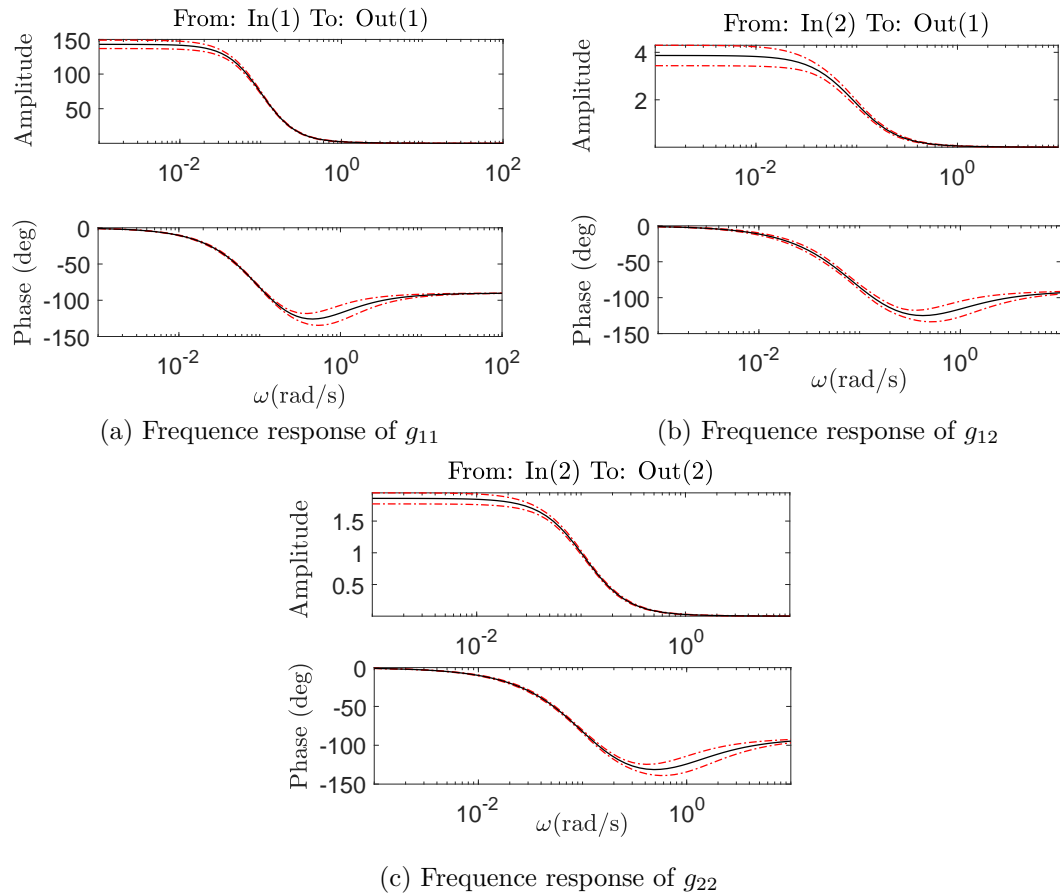


FIGURE 4.11: Frequency responses with uncertainty bounds

TABLE 4.3: Parameters obtained from transient and frequency responses of the estimated model

| System matrix (G) | Transient response | | | Frequency response | | |
|-----------------------|--------------------|-------------------|-------------------|--------------------|----------|-----------------|
| | Rise time (s) | Settling time (s) | Time constant (s) | GM | PM | $\omega(rad/s)$ |
| g_{11} | 32.6 | 55.4 | 20 | ∞ | 135 | 0.045 |
| g_{12} | 35.8 | 61.4 | 21.3 | ∞ | ∞ | - |
| g_{22} | 30.6 | 51.2 | 19 | ∞ | 124 | 0.06 |

The transient and frequency response parameters of the identified model are summarized in Table 4.3.

4.4 Summary

In this chapter, a simple control-oriented, multi-variable linear model for the UPT field has been identified. The essential input-output data sets required for the

system identification have been generated by a benchmark UCG simulator i.e. CAVSIM. In the identification experiment, the PRBS signal has been used as an excitation signal, and its design procedure is presented in detail. A state-space model with an order of 2 is estimated by using the N4SID system identification technique. Moreover, the identified model has been validated with an independent data set by using simulation error and residual analysis methods. Finally, various aspects of the estimated model like interaction, uncertainty, and dynamic properties in time and frequency domains have been analyzed.

It has been observed that the identified model retains the fundamental dynamics of the actual process, therefore, it can be employed to develop a model-based control for the UPT field. A multi-variable H_∞ robust control design based on the identified model is presented in the next chapter.

Chapter 5

Design of Multi-variable H_∞ Controller for the UPT Gasifier

The complexity of CAVSIM is a major limitation in the designing of a model-based control system for the UCG process. Thus, the model identified in chapter 4 is used to design the multi-variable robust control system for the UPT field. In the literature [19, 54, 55, 93, 94, 96–98], the closed-loop UCG system is devised by considering the UCG process as a single input single output (SISO) system. The controllers are designed to maintain the heating value of syngas at a desired level by manipulating the flow rate of inlet gas. However, the flow rate of syngas has not been controlled, which is also important in determining the potential of a UCG site for electricity production. Hence, it is essential to devise a multi-variable, model-based control system for the UCG process. Typically, a robust controller is required when a complex process is manifested by a simple model. For any UCG site, the control system must be robust to cater the process uncertainties, external disturbances, modeling inaccuracies, and parametric uncertainties [96]. The H_∞ is one of the linear robust control techniques commonly used to design linear time-invariant (LTI) model-based control systems. In this chapter, model-based multi-variable H_∞ controller is designed by employing the standard approach.

The overview of standard approach of H_∞ controller is presented in section 5.1. The control problem is stated in section 5.2, which is followed by the design procedure of H_∞ in section 5.3 . The simulation results for the robust stability and robust performance of H_∞ controllers are shown in section 5.4. The implementation of the designed controller is discussed in section 5.5, and finally the chapter is concluded in section 5.6.

5.1 Introduction

In control theory, H_∞ methods are generally used to synthesize controllers to achieve the desired performance and robustness. In H_∞ methods, a standard approach is employed to cast the control problem as an H_∞ optimization problem [120]. The standard configuration is shown in Fig. 5.1a, where \tilde{P} and K represents the generalized plant and controller, respectively. While \mathbf{u} and \mathbf{v} are the vectors of control and measurable variables, respectively. The exogenous inputs like reference commands and disturbances are shown by \mathbf{w} , and \mathbf{z} represents the exogenous output variables. The control objective is to minimize H_∞ norm of the transfer function from \mathbf{w} to \mathbf{z} . The transfer function matrix P from $\begin{bmatrix} \mathbf{w} & \mathbf{u} \end{bmatrix}^T$ to $\begin{bmatrix} \mathbf{z} & \mathbf{v} \end{bmatrix}^T$ is given as

$$\begin{bmatrix} \mathbf{z} \\ \mathbf{v} \end{bmatrix} = \tilde{P}(s) \begin{bmatrix} \mathbf{w} \\ \mathbf{u} \end{bmatrix} = \begin{bmatrix} \tilde{P}_{11}(s) & \tilde{P}_{12}(s) \\ \tilde{P}_{21}(s) & \tilde{P}_{22}(s) \end{bmatrix} \begin{bmatrix} \mathbf{w} \\ \mathbf{u} \end{bmatrix}, \quad (5.1)$$

$$\mathbf{u} = K(s)\mathbf{v}. \quad (5.2)$$

The controller is represented as a separate block in the standard configuration, which is useful in controller synthesis. However, for the closed-loop performance analysis of the designed controller, the system \tilde{N} is obtained by absorbing the designed controller K into the interconnection structure (\tilde{P}), as shown in Fig 5.1b. As $\mathbf{z} = \tilde{N}\mathbf{w}$, where \tilde{N} is a function of K , and it is determined by eliminating \mathbf{u}

and \mathbf{v} from (5.1) and (5.2), and given as

$$\tilde{N} = \tilde{F}_l(\tilde{P}, K) \triangleq \tilde{P}_{11} + \tilde{P}_{12}K(I - \tilde{P}_{22}K)^{-1}\tilde{P}_{21}, \quad (5.3)$$

where $\tilde{F}_l(\tilde{P}, K)$ is the lower linear fractional transformation of \tilde{P} and K . The control objective becomes

$$\min_{K_{stab}} \|\tilde{F}_l(\tilde{P}, K)\|_\infty, \quad (5.4)$$

and it is called the H_∞ optimization problem.

5.1.1 Mixed-sensitivity H_∞ Synthesis

The closed-loop performance within the framework of H_∞ is generally defined by the H_∞ norm of the closed-loop transfer function between the weighted inputs vector (\mathbf{w}) to the weighted outputs vector (\mathbf{z}) [120, 121]. Mixed-sensitivity is one of the methods to design the H_∞ controller in which the singular values of specified transfer functions are shaped over frequency. The sensitivity function $S = (I + GK)^{-1}$ can be shaped along with other transfer functions like complementary sensitivity ($T = GK(I + GK)^{-1} = I - S$) and control sensitivity (KS) transfer

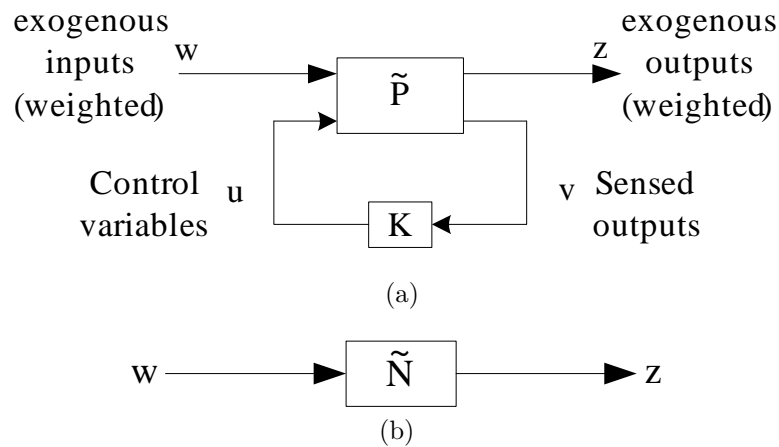


FIGURE 5.1: Standard control configuration without uncertainty for controller (a) synthesis and (b) analysis [120]

functions. The terms S and T follow the identity i.e. $S+T = I$, which implies that both S and T can not be made smaller simultaneously. The desired performance can be achieved by making the tracking errors (\mathbf{e}) small for the desired reference trajectories (\mathbf{r}) and the output disturbances (\mathbf{d}_o). The transfer function from output to the reference (y/r) is defined by T , while the transfer functions \mathbf{e}/\mathbf{r} and \mathbf{y}/\mathbf{d}_o are given by S . Hence, T must be unity at frequencies where the desired tracking performance is required and it should be less than unity at high frequencies to ensure robust stability. Moreover, the weighted sensitivity function ($\|W_p S\|_\infty$) must be small to achieve the perfect tracking and disturbance rejection. However, practically, this cost function is not sufficient, and a weighted transfer function ($W_u K S$) is also considered to limit the control energy, and the resulting cost function is given as

$$\left\| \begin{bmatrix} W_p S \\ W_u K S \end{bmatrix} \right\|_\infty, \quad (5.5)$$

where W_p and W_u are the weight functions associated with the tracking errors and control inputs, respectively. In summary, the closed-loop objectives are to make:

- $\bar{\sigma}(S)$ small for disturbance rejection.
- $\bar{\sigma}(T)$ small for noise attenuation.
- $\bar{\sigma}(T) \approx \underline{\sigma}(T) \approx 1$ for reference tracking
- $\bar{\sigma}(KS)$ small to reduce control energy

5.2 Problem Formulation

The objective is to design a multi-variable robust control system for the UCG process, which maintains the desired levels of heating value and flow rate of syngas by manipulating the concentration of inlet gas flow rate and the steam to oxygen

ratio ($\text{H}_2\text{O}/\text{O}_2$). Moreover, the designed control law must be capable to cater the effect of external disturbance, and the modeling errors caused by the linearization.

5.3 Design of H_∞ Controller for the UPT Field

The standard design structure of H_∞ robust controller is used to formulate the control problem, which is one of the most successful and reliable approaches to design a linear robust controller [120]. The one degree of freedom closed-loop diagram of UCG control system is presented in Fig. 5.2. To model the effect of modeling inaccuracies due to linearization, an unstructured uncertainty–multiplicative input uncertainty is considered. The various sources of uncertainty in many practical applications are represented by the multiplicative input uncertainty because this type of uncertainty often occurs in real system and it also restricts the achievable performance [122]. The uncertain plant with an input multiplicative uncertainty is represented in (5.6).

$$G_{\Pi}(s) = G_{s_{nom}}(s)(I + W_{\Delta}\Delta); \quad \|\Delta\|_{\infty} \leq 1, \quad (5.6)$$

where $G_{\Pi}(s)$ and $G_{s_{nom}}(s)$ represent the perturbed and nominal scaled models, respectively. The unmodeled and neglected dynamics are represented by a complex perturbation Δ and the multiplicative weight W_{Δ} is a diagonal matrix of stable minimum phase transfer functions used to normalize the uncertainties to be less than unity.

The H_∞ controller for the UCG system is designed by incorporating the generalized plant (\tilde{P}) or interconnected system, controller (K) and the uncertainty block (Δ) into the standard configuration of H_∞ controller as shown in Fig. 5.3. The control and all exogenous input signals like reference inputs (\mathbf{r}) and input disturbances (\mathbf{d}_i) are represented by vectors \mathbf{u} and \mathbf{w} , respectively. The steam flow rate is considered as an input disturbance for the system. While the control efforts (\mathbf{e}_u) and tracking errors (\mathbf{e}_y) to be penalized are considered as exogenous outputs and denoted by a vector \mathbf{z} . The measurable quantities such as syngas heating value

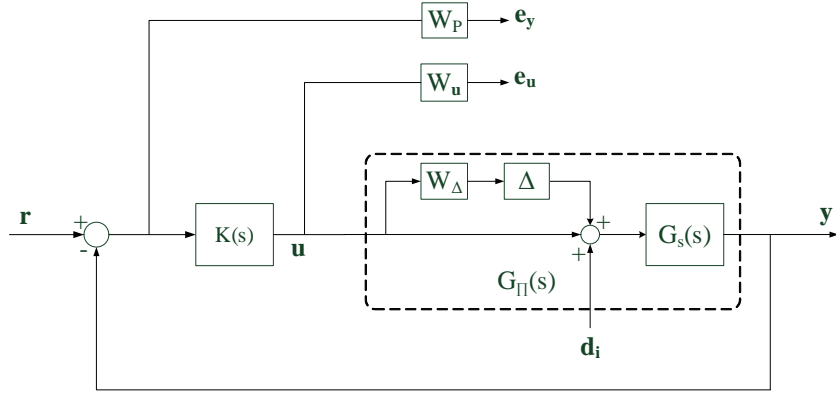


FIGURE 5.2: Block diagram of the closed-loop system with performance specifications

(y_1) and flow rate (y_2) are represented by a vector \mathbf{y} .

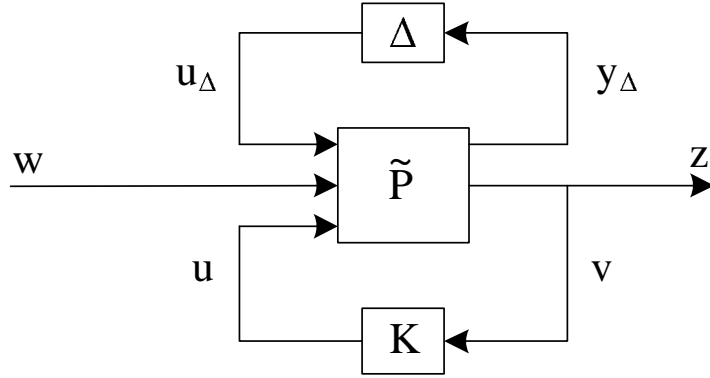


FIGURE 5.3: General configuration for controller synthesis

$$\begin{aligned}
 \mathbf{w} &= \begin{bmatrix} \mathbf{r} & \mathbf{d}_i \end{bmatrix}^T, \\
 \mathbf{z} &= \begin{bmatrix} \mathbf{e}_y & \mathbf{e}_u \end{bmatrix}^T = \begin{bmatrix} W_P(\mathbf{r} - \mathbf{y}) & W_u \mathbf{u} \end{bmatrix}^T = \begin{bmatrix} W_P(\mathbf{r} - G_s \mathbf{u} - G_s \mathbf{d}_i) & W_u \mathbf{u} \end{bmatrix}^T, \\
 \mathbf{v} &= \mathbf{r} - \mathbf{y} = \mathbf{r} - G_s(\mathbf{u} + \mathbf{d}_i).
 \end{aligned} \tag{5.7}$$

The generalized plant (\tilde{P}) from $\begin{bmatrix} \mathbf{w} & \mathbf{u} \end{bmatrix}^T$ to $\begin{bmatrix} \mathbf{z} & \mathbf{v} \end{bmatrix}^T$ is given as

$$\begin{bmatrix} \mathbf{e}_y \\ \mathbf{e}_u \\ \mathbf{v} \end{bmatrix} = \begin{bmatrix} W_P I & -W_P G_s & -W_P G_s \\ 0 & 0 & W_U \\ I & -G_s & -G_s \end{bmatrix} \begin{bmatrix} \mathbf{r} \\ \mathbf{d}_i \\ \mathbf{u} \end{bmatrix}, \tag{5.8}$$

where,

$$\tilde{P} = \left[\begin{array}{cc|c} W_P I & -W_P G_s & -W_P G_s \\ 0 & 0 & W_U I \\ \hline I & -G_s & -G_s \end{array} \right],$$

$$\tilde{P}_{11} = \begin{bmatrix} W_P I & -W_P G_s \\ 0 & 0 \end{bmatrix}, \quad \tilde{P}_{12} = \begin{bmatrix} -W_P G_s \\ W_U I \end{bmatrix}, \quad \tilde{P}_{21} = \begin{bmatrix} I & -G_s \end{bmatrix}, \quad \tilde{P}_{22} = \begin{bmatrix} -G_s \end{bmatrix}.$$

The nominal system (\tilde{N}) shown in Fig. 5.4b is a closed-loop transfer function from \mathbf{w} to \mathbf{z} . It is determined by absorbing K into the interconnection structure. From (5.8)

$$\mathbf{z} = \tilde{P}_{11} \mathbf{w} + \tilde{P}_{12} \mathbf{u}, \quad (5.9a)$$

$$\mathbf{v} = \tilde{P}_{21} \mathbf{w} + \tilde{P}_{22} \mathbf{u}. \quad (5.9b)$$

and

$$\mathbf{u} = K \mathbf{v}. \quad (5.10)$$

By solving (5.9b) and (5.10)

$$\mathbf{u} = K \left(\tilde{P}_{21} \mathbf{w} + \tilde{P}_{22} \mathbf{u} \right),$$

$$\mathbf{u} = K (I - \tilde{P}_{22} K)^{-1} \tilde{P}_{21} \mathbf{w}.$$

Hence, (5.9a) becomes

$$\tilde{N} = \tilde{F}_l(\tilde{P}, K) \triangleq \tilde{P}_{11} + \tilde{P}_{12} K (I - \tilde{P}_{22} K)^{-1} \tilde{P}_{21}, \quad (5.11)$$

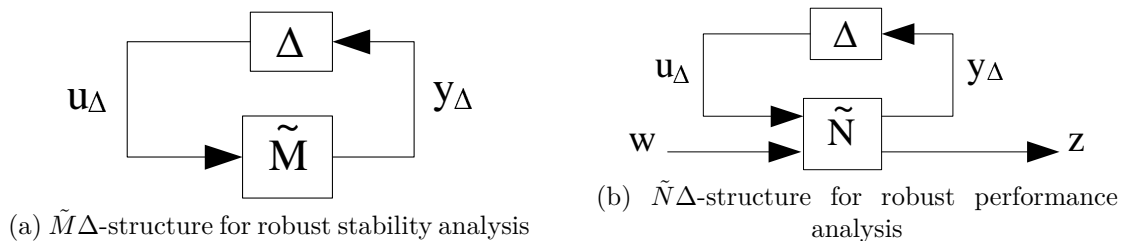


FIGURE 5.4: General configurations for controller analysis

where $\tilde{F}_l(\tilde{P}, K)$ is the lower linear fractional transformation of \tilde{P} and K . After solving (5.11), $\tilde{F}_l(\tilde{P}, K)$ becomes

$$\tilde{N} = \begin{bmatrix} W_P(I - T_o) & W_P G_s(T_o - I) \\ W_U K S_o & -W_U K G_s S_o \end{bmatrix}. \quad (5.12)$$

Similarly, an upper LFT ($\tilde{F}_u(\tilde{N}, \Delta)$) between \tilde{N} and Δ can be used to relate the uncertain closed-loop transfer function from \mathbf{w} to \mathbf{z} , and it is found as

$$\mathbf{y}_\Delta = N_{11}\mathbf{u}_\Delta + N_{12}\mathbf{w}, \quad (5.13a)$$

$$\mathbf{z} = N_{21}\mathbf{u}_\Delta + N_{22}\mathbf{w}. \quad (5.13b)$$

In $\tilde{N}\Delta$ shown in Fig. 5.4b, Δ is a transfer function from the input \mathbf{y}_Δ to the output \mathbf{u}_Δ , therefore,

$$\mathbf{u}_\Delta = \Delta\mathbf{y}_\Delta. \quad (5.14)$$

After solving (5.13a), (5.13b) and (5.14), $\tilde{F}_u(\tilde{N}, \Delta)$ becomes

$$\tilde{F}_u(\tilde{N}, \Delta) \triangleq \tilde{N}_{22} + \tilde{N}_{21}\Delta(I - \tilde{N}_{11}\Delta)^{-1}\tilde{N}_{12}. \quad (5.15)$$

In $\tilde{M}\Delta$ structure shown in Fig. 5.4a, \tilde{M} is the transfer function from \mathbf{y}_Δ to \mathbf{u}_Δ , and by using (5.13a)

$$\tilde{M} = \tilde{N}_{11}.$$

The closed-loop transfer function matrix $\Phi(s)$ from \mathbf{w} to \mathbf{z} is given in (5.16). The H_∞ norm of $\Phi(s)$ must be less than unity for all possible stable perturbations to attain the performance objectives.

$$\begin{bmatrix} \mathbf{e}_Y \\ \mathbf{e}_U \end{bmatrix} = \begin{bmatrix} W_p S_o & W_p G_\Pi S_i \\ W_u S_i K & -W_u K S_o G_\Pi \end{bmatrix} \begin{bmatrix} \mathbf{r} \\ \mathbf{d}_i \end{bmatrix}, \quad (5.16)$$

or it can be written as

$$\begin{bmatrix} \mathbf{e}_Y \\ \mathbf{e}_U \end{bmatrix} = \Phi(s) \begin{bmatrix} \mathbf{r} \\ \mathbf{d}_i \end{bmatrix},$$

where $S_o = (I + G_\Pi K)^{-1}$ and $S_i = (I + KG_\Pi)^{-1}$ are the output and input sensitivity functions, respectively.

5.3.1 Robust Stability and Performance Constraints

The $\tilde{M}\Delta$ and $\tilde{N}\Delta$ configurations shown in Fig. 5.4a and Fig. 5.4b are used to perform the robust stability and performance analysis of an uncertain system, respectively. It is essential to satisfy that the nominal stability (NS) condition i.e. \tilde{N} is internally stable prior to carrying out the robust stability (RS), nominal performance (NP) and robust performance (RP) analysis. When \tilde{N} is stable then it can be seen in (5.15) that the instability may only occur due to the feedback term $(I - \tilde{N}_{11}\Delta)^{-1}$. Therefore, if the system has nominal stability then the stability of $\tilde{N}\Delta$ and $\tilde{M}\Delta$ structures become equivalent to each other. The stability objectives are formulated as:

$$NS \Leftrightarrow \tilde{N} \text{ is internally stable,} \quad (5.17a)$$

$$\begin{aligned} RS &\Leftrightarrow \|\tilde{M} = \tilde{N}_{11}\|_\infty < 1, \forall \omega, \text{ NS and } \Delta \text{ is stable,} & (5.17b) \\ &\Leftrightarrow \|W_U K (I + GK)^{-1}\|_\infty < 1, \forall \omega, \text{ NS and } \Delta \text{ is stable.} \end{aligned}$$

The robust performance analysis of an uncertain system is performed by computing structured singular value (μ) [120]. The standard configuration for μ analysis is shown in Fig. 5.4, and its simplest form is

$$\mu(\tilde{M})^{-1} \triangleq \min_{\Delta} \{\bar{\sigma}(\Delta) | \det(I - \tilde{M}\Delta) = 0 \text{ for structured } \Delta\}, \quad (5.18)$$

where $\Delta = \text{diag}\{\Delta_i\}$ represents a set of complex matrices with a given block diagonal structure in which few blocks may be restricted to be real, and some of them may be repeated. The transfer function from the output to the input of the uncertainties is represented by a matrix $\tilde{M} = \tilde{N}_{11}$, $\det()$ is the determinant, and $\bar{\sigma}()$ is the maximum singular value. The definition of μ given in (5.18) considers varying $\bar{\sigma}(\Delta)$, however, it is preferred to normalize Δ such that $\bar{\sigma}(\Delta) \leq 1$. It can be done by scaling Δ by a factor β_o , and find the smallest β_o at which the matrix

$I - \tilde{M}\Delta$ becomes singular, and it gives $\mu = 1/\beta_o$. The real non-negative function $\mu(\tilde{M})$, called the structured singular value, is defined by

$$\mu(\tilde{M}) \triangleq \frac{1}{\min\{\beta_o | \det(I - \tilde{M}\Delta) = 0 \text{ for structured } \Delta, \bar{\sigma}(\Delta) \leq 1\}}, \quad (5.19)$$

where μ is a measure of smallest possible perturbation which can make the system unstable. When $\mu = 1$, it implies that the perturbation exists in the system having $\bar{\sigma}(\Delta) = 1$ is large enough to make it unstable ($I - \tilde{M}\Delta$ becomes singular). Thus, the smaller value of μ is desired i.e. $\mu(\tilde{M}) \leq 1$ in the designing of robust controller to attain more robustness in the presence of large uncertainty.

The standard $\tilde{N}\Delta$ configuration is used to obtain the nominal and robust performance constraints, which are given as

$$NP \Leftrightarrow \|\tilde{N}_{22}\|_\infty < 1 \Leftrightarrow \|W_P G_s\|_\infty < 1, \text{ and NS}, \quad (5.20a)$$

$$RP \Leftrightarrow \|\tilde{F}_u(\tilde{N}, \Delta)\|_\infty < 1, \forall \|\Delta\|_\infty \leq 1, \quad (5.20b)$$

$$\Leftrightarrow \mu_{\tilde{\Delta}}(\tilde{N}) < 1, \forall \omega, \tilde{\Delta} = \begin{bmatrix} \Delta & 0 \\ 0 & \Delta_P \end{bmatrix}, \text{ and NS},$$

where $\tilde{\Delta}$ is a block diagonal matrix and its detailed structure is described by the represented uncertainty, and Δ_P is used to indicate the H_∞ performance objectives and it is always a full complex matrix.

5.3.2 Selection of Weights

The performance objectives to minimize the tracking error and control effort are closely related to the sensitivity function S . The magnitude of S must be small at the frequency ranges where the small tracking error is required in each of the controlled output. Thus, it can be achieved by introducing an integrator s^{-1} in the weights related with each controlled output. In well posed standard H_∞ control problem, the use of only pure integrator in performance weight is not suitable in a sense that the generalized plant \tilde{P} could not be stabilized by the feedback controller

K . Thus, the typical specifications for S in frequency domain are determined in terms of peak sensitivity (M_s) and bandwidth ω_b .

$$|S(s)| = \left| \frac{s}{s/M_b + \omega_b} \right|, \quad s = j\omega, \quad \forall \omega, \quad (5.21)$$

or equivalently,

$$|w_P S| \leq 1, \quad (5.22)$$

where,

$$w_P = \frac{s/M_b + \omega_b}{s}. \quad (5.23)$$

The weight function given in (5.23) is modified by introducing the maximum steady-state tracking error (ϵ) i.e. $|S(0)| \leq \epsilon$, which satisfies $w_P(0) \leq 1/\epsilon$ such that $|w_P S|_\infty \leq 1$

$$w_P = \frac{s/M_b + \omega_b}{s + \omega_b \epsilon}. \quad (5.24)$$

The parameters ω_b , ϵ and M_b represent the design specifications of closed-loop bandwidth, steady-state error and overshoot, respectively. The integral action with $S(0) \approx 0$ is approximated by choosing the steady state error much smaller than the unity ($\epsilon \ll 1$), and the overshoot is usually selected as $M_b \leq 2$ [120]. A small value of bandwidth is chosen due to the slow dynamics of the UCG process [93]. In the proposed problem, $\omega_b = 0.001 \text{ rad/s}$, $M_b = 1.5$ and $\epsilon = 10^{-4}$ are chosen. For simplicity, equal weights are used for both channels.

$$w_{P_{ii}} = \frac{0.6667s + 0.001}{s + 1e - 07}, \quad i = 1, 2, \quad (5.25)$$

$$W_P = \begin{bmatrix} w_{P_{11}} & 0 \\ 0 & w_{P_{22}} \end{bmatrix}. \quad (5.26)$$

The weight W_U is taken as $0.5I_{2 \times 2}$ at all frequencies to avoid saturation on the control input. A simple stable, minimum phase transfer function shown in (5.27) is used to normalize the multiplicative uncertainty.

$$w_{\Delta_{ii}} = \frac{\alpha s + r_o}{\alpha/r_\infty s + 1}, \quad (5.27)$$

where r_o and r_∞ are the relative uncertainties at steady state and higher frequencies, respectively. While $1/\alpha$ indicates the point at which the relative uncertainty reaches approximately at 100%. In the proposed problem similar uncertainty weights are used for both inputs, having $\alpha = 0.1$, $r_o = 0.2$ and $r_\infty = 3$, and given as

$$w_{\Delta_{ii}} = \frac{0.1s + 0.2}{\frac{0.1}{3}s + 1}, \quad i = 1, 2, \quad (5.28)$$

$$W_\Delta = \begin{bmatrix} w_{\Delta_{11}} & 0 \\ 0 & w_{\Delta_{22}} \end{bmatrix}. \quad (5.29)$$

5.4 Results and Discussion

The MATLAB robust control toolbox is used to determine the H_∞ -optimal controller by employing S/KS mixed sensitivity design method. The controller is synthesized by ignoring the uncertainties and only the nominal plant is considered in controller design. The infinity norm of $F_l(\tilde{P}, K)$ is minimized with respect to K by the S/KS mixed sensitivity controller. While in the given problem $F_l(\tilde{P}, K)$ is the closed-loop transfer matrix ($\Phi(s)$) represented in (5.17). The desired performance specifications are incorporated by the performance weight matrix W_P and the inverse of performance weight matrix defines the upper bound on singular values of S ($\sigma(S)$). The desired bandwidth and upper bound on $\sigma(S)$ at different frequency ranges is shown by the frequency response of inverse performance weight matrix in Fig. 5.5. It can be seen that the $1/|W_P|$ is equal to unity at the frequency $\omega_b = 0.001\text{rad/s}$, which is the desired bandwidth. While it has magnitude equal to $A = 1e^{-4}$ and $M = 1.4$ at low and high frequencies, respectively.

The singular-value plots of S , KS and T for the perturbed plant are shown in Fig. 5.6a, 5.6b and 5.6c, respectively. It can be seen that the magnitude of S is

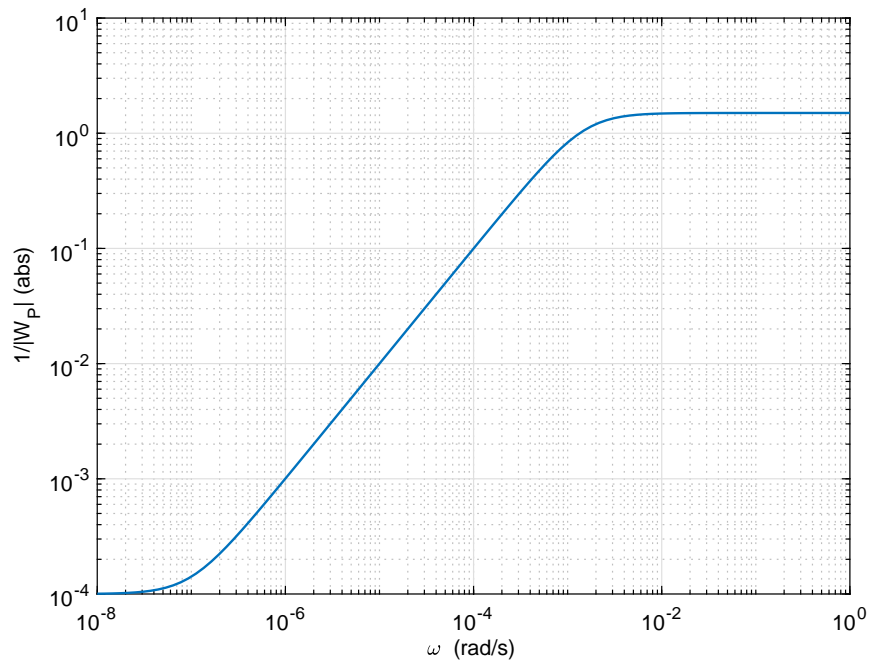


FIGURE 5.5: Inverse of performance weight

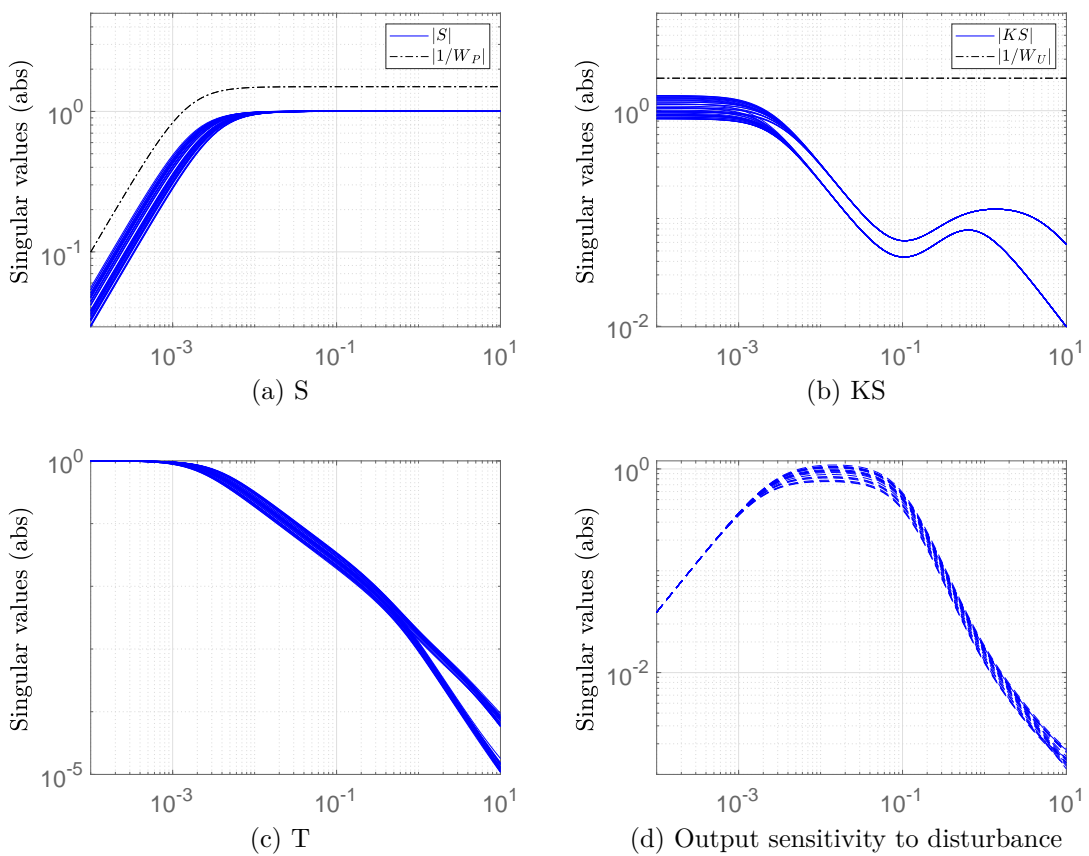


FIGURE 5.6: Frequency response of closed-loop system

lower than the upper bound and the magnitude of T at low frequencies is unity, which conform that the desired performance is achieved. While the singular-values of KS are lower than their upper bounds, which shows that the actuators are not saturated to attain the desired bandwidth. The nominal stability properties of closed-loop transfer functions are same due to the similar internal dynamics. Thus, these results also show that the closed-loop system has achieved the nominal stability. Moreover, the effect of output sensitivity $S_{out} = y/d_i$ to disturbance for perturbed plant is also analyzed in Fig. 5.6d . It can be seen that disturbance has negligible effect at low frequencies, which means that the closed-loop system is not susceptible to disturbance over that frequency range.

The robust stability and nominal performance of the closed-loop system are determined by plotting the singular values of \tilde{M} and \tilde{N}_{22} , as shown in Fig. 5.7 and Fig. 5.8, respectively. The singular values can be seen to be less than unity, which shows that the closed-loop system meets the robust stability and nominal performance constraints. The closed-loop system can tolerate up to 503% of the modeled uncertainty, as given in Table 5.1. In Fig. 5.9, the frequency response of μ is shown to analyze the robust performance of closed-loop system. The controller has achieved the robust performance as μ is less than unity. The performance margins in the form of upper and lower bounds are given in Table 5.2. Moreover, it is observed that the model uncertainty of 115% can lead to input/output gain of 0.871 at 0.00014 rad/seconds.

The closed-loop step response of linear system is shown in Fig. 5.10 The step signal is applied at all exogenous inputs and it can be seen that both the outputs track the desired response in the presence of model uncertainty and input disturbance. In addition, it also meets the desired performance specifications corresponding to the transient characteristics, such as the overshoot, time constant and settling time. The input disturbance is introduced to the framework to assess the controller's success in rejecting the disruption. The optimal amount of water is one of the important parameter for the successful operation of UCG reactor. The excess water can disrupt the operation of UCG gasifier and reduces its temperature due to the endothermicity of the steam gasification reaction. Therefore, an optimal level of

TABLE 5.1: Robust stability margins for H_∞ controllers.

| Controller | Order | Stability margins | | |
|------------|-------|------------------------------|------------------------------|--|
| | | Lower bound ($1/\mu_u$) | Upper bound ($1/\mu_l$) | Destabilizing frequency (rad/s) |
| S/KS1 | 7 | 5.296878 | 5.296881 | 0.001 |

TABLE 5.2: Robust performance margins for H_∞ controllers

| Controller | Order | Performance margins | | |
|------------|-------|------------------------------|------------------------------|--|
| | | Lower bound ($1/\mu_u$) | Upper bound ($1/\mu_l$) | Destabilizing frequency (rad/s) |
| S/KS | 7 | 1.1475 | 1.1478 | 0.00013 |

H_2O is necessary for the successful operation of UCG field [19]. Therefore, the water influx from the surrounding strata acts as an input disturbance in the UCG process, as it increases the H_2O/O_2 . In Fig. 5.11, it can be seen that the controller caters the input disturbance by manipulating the H_2O/O_2 such that it varies the molar fraction of steam and maintains an optimum value of steam.

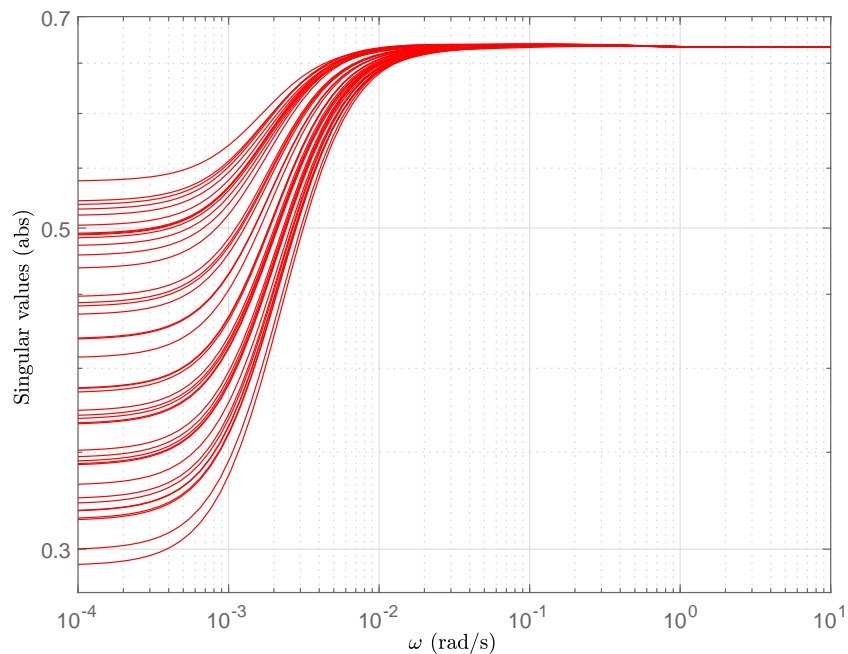


FIGURE 5.7: Robust stability

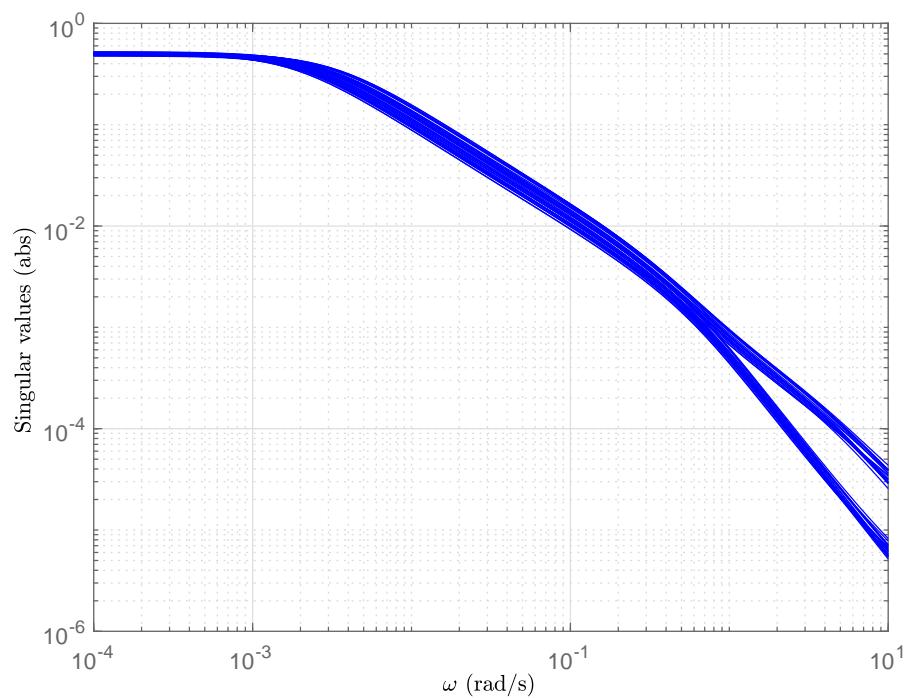


FIGURE 5.8: Nominal performance

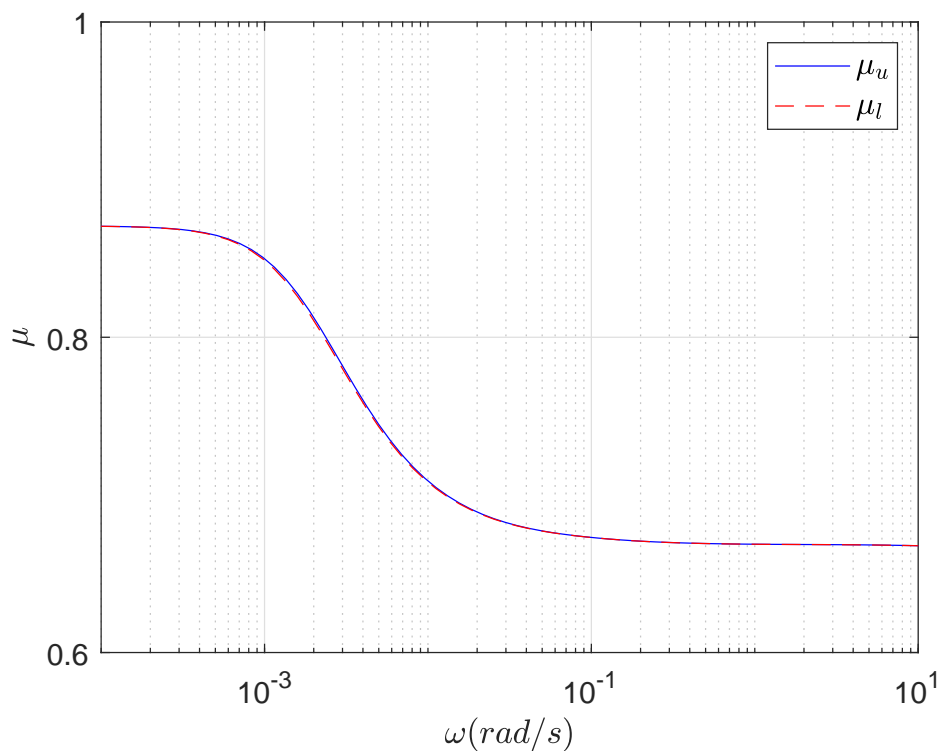


FIGURE 5.9: Robust performance analysis

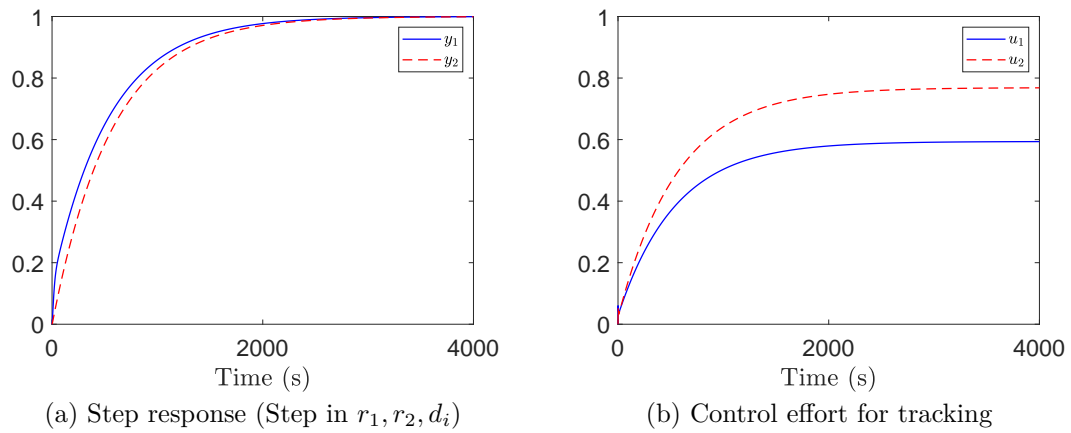


FIGURE 5.10: Closed-loop transient response of scaled-linear system

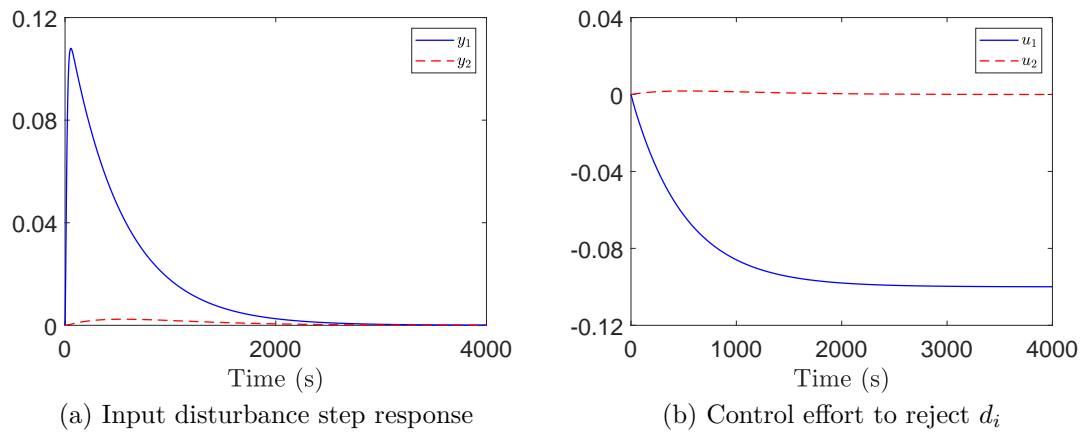


FIGURE 5.11: Closed-loop response to input disturbance

5.5 Implementation of Controller on the CAVSIM

The robust controller designed on the basis of linear model in section 5.3 is discretized and implemented on the actual nonlinear model i.e. CAVSIM in order to assess the robustness and performance of the designed controller. The CAVSIM computer code has been developed by LLNL, and it is written in FORTRAN and a Microsoft Developer Studio is used to run the program [23]. The implementation of designed controller on CAVSIM is a challenging task, and it requires detailed

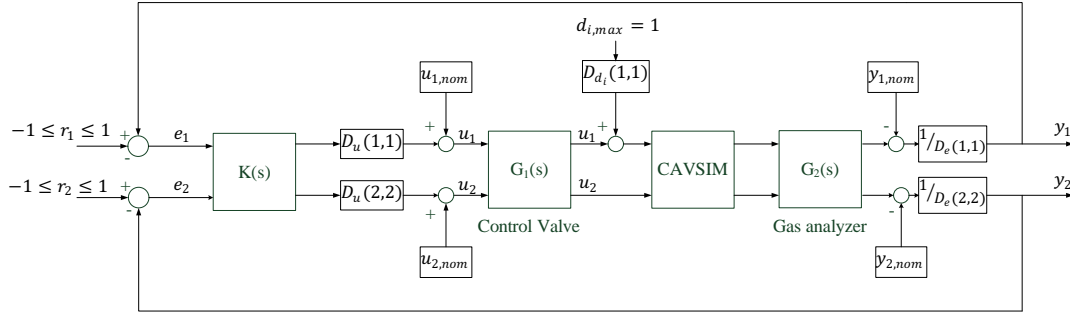


FIGURE 5.12: Controller implementation scheme

understanding of the 3D model and the computer code. The model mechanistically calculates cavity surface recession rates from mass and energy balances, and it is capable to simulate the cavity growth for entire life of UCG. Moreover, the dynamics of control valve and the gas analyzer are modeled with the following transfer functions [96].

$$G_1(s) = \frac{e^{-\tau_{dc}s}}{\tau_c s + 1}, \quad G_2(s) = \frac{e^{-\tau_{dg}s}}{\tau_g s + 1}. \quad (5.30)$$

It has been experimentally found that the control valve and gas analyzer have negligible time delays (τ_{dc} , τ_{dg}) and are therefore ignored in (5.30). While the time constants for the control valve (τ_c) and gas analyzer (τ_g) were found to be about 10s.

The controller implementation scheme on actual system is shown in Fig. 5.12. It is pertinent to mention that the controller has been designed from a scaled model, therefore, it is essential to include the scaling matrices D_u , D_e and D_{d_i} in the actual implementation, which are given in (4.13). Moreover, the nominal operating points of inputs given in (4.1) are included after the inputs scaling matrix in such a way that the inputs feed to CAVSIM are the actual inputs. While in order to create the scaled inputs to the controller, the nominal operating points of outputs are subtracted from the actual outputs of CAVSIM prior to output scaling matrix and feedback. The unscaled controlled inputs are given by

$$\begin{bmatrix} u_1 \\ u_2 \end{bmatrix} = \begin{bmatrix} u_{1,nom} \\ u_{2,nom} \end{bmatrix} + D_u K_d(z) \begin{bmatrix} e_1 \\ e_2 \end{bmatrix}, \quad (5.31)$$

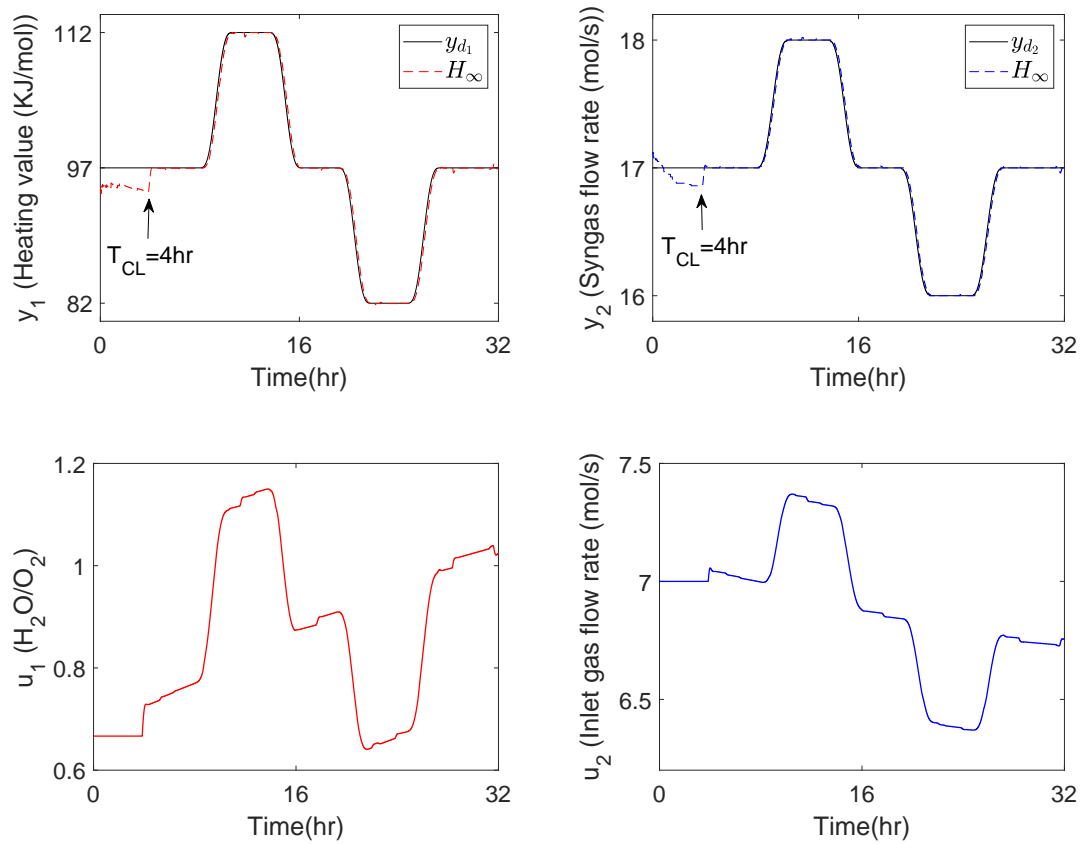


FIGURE 5.13: Closed-loop response of nonlinear model to the reference inputs

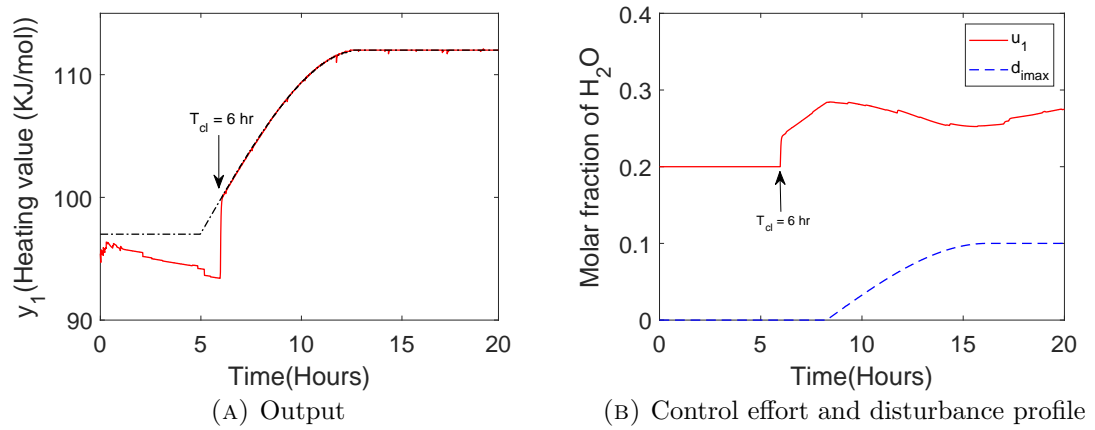


FIGURE 5.14: Close-loop response of nonlinear model to the input disturbance

where $K_d(z)$ is a discretized controller. $K_d(z)$ is obtained by using the tustin method with a sampling time of 10s, and it is given as

$$K_d(z) = \begin{bmatrix} K_{11}(z) & K_{12}(z) \\ K_{21}(z) & K_{22}(z) \end{bmatrix}, \quad (5.32)$$

where,

$$\begin{aligned}
K_{11}(z) &= \frac{0.08z^7 + 0.06z^6 - 0.06z^5 - 0.03z^4 + 0.02z^3 + 0.001z^2 - 0.002z + 0.0003}{z^7 + 0.64z^6 - 1.20z^5 - 0.85z^4 + 0.23z^3 + 0.20z^2 - 0.009z - 0.012}, \\
K_{12}(z) &= \frac{-0.02z^7 - 0.01z^6 + 0.01z^5 + 0.002z^4 - 0.002z^3 - 7.4e^{-4}z^2 + 5.6e^{-4}z}{z^7 + 0.64z^6 - 1.20z^5 - 0.85z^4 + 0.23z^3 + 0.20z^2 - 0.009z - 0.012}, \\
K_{21}(z) &= \frac{-0.01z^7 - 0.002z^6 + 0.007z^5 - 9e^{-4}z^4 - 2.3e^{-5}z^3 - 6.7e^{-4}z^2 + 3.2e^{-4}z}{z^7 + 0.64z^6 - 1.20z^5 - 0.85z^4 + 0.23z^3 + 0.20z^2 - 0.009z - 0.012}, \\
K_{22}(z) &= \frac{0.07z^7 + 0.06z^6 - 0.06z^5 - 0.02z^4 + 0.02z^3 + 1.4e^{-4}z^2 - 0.002z + 3.2e^{-4}}{z^7 + 0.64z^6 - 1.20z^5 - 0.85z^4 + 0.23z^3 + 0.20z^2 - 0.009z - 0.012}.
\end{aligned}$$

The UCG process is operated in open loop with the nominal inputs for 06 hours and the closed-loop process starts afterwards. Fig. 5.13 shows that the controller effectively holds both the outputs to their desired levels by adjusting the control inputs as well as maintaining the control efforts within the allowed range, as given in (4.1). The desired trajectories of the outputs are chosen in such a way that they cover the entire range of operating points for which the controller has been designed. As described earlier in section 6.5, the molar fraction of steam is an input disturbance in the UCG process. Another simulation test is performed to determine the disturbance rejection capability of the designed control law, and it is shown in Fig. 5.14b. The disturbance enters the system at the 8th hour and it can be seen that the controller rejects the input disturbance by varying the inlet molar fraction of H₂O. When the water influx increases the molar fraction of H₂O, the controller maintains the optimal amount of H₂O by reducing the amount of inlet steam.

5.6 Summary

This chapter highlights the significance of the multi-variable closed-loop system for the UCG field. An H_∞ controller is designed using S/KS method. The control problem is formulated by employing the standard control configuration along with the weighting functions. The robust stability and performance analysis have been performed in the presence of modeling inaccuracies. Moreover, it is shown that

the linear closed-loop system meets all the desired transient requirements in the presence of input disturbance and modeling uncertainties. Finally, the controller is discretized and implemented on the CAVSIM to assess the robustness. The implementation scheme is described in detail, and it is shown that the outputs attain their desired values in the presence of an input disturbance and modeling inaccuracies.

After the successful implementation of the linear robust controller, the next task is to develop the nonlinear robust control system for the UCG field. The linear controllers always ensure adequate performance and stability for a limited operating range. As the UCG process is highly complex and nonlinear, therefore, a robust SMC technique is designed and presented in the next chapter. It has been shown that the SMC can control the process over a wide operating range.

Chapter 6

Design of Multi-variable Sliding Mode Controllers for the UPT Gasifier

This chapter presents the design of model-based SMC techniques, which are based on the linear model identified in chapter 4. The SMC technique has various merits over the other robust control techniques due to its distinguished features, such as reduced order sliding mode equations, insensitivity to matched disturbances and uncertainties, and it offers a nonlinear control [123–125]. In this chapter, the linear model of the UCG process is transformed into the regular form, which is subsequently employed to design a conventional SMC and a dynamic SMC (DSMC). As the dynamics of CAVSIM is very complex, and it is not possible to analytically prove the stability of the 3D PDEs. Therefore, a simple 1D packed bed model of the UPT field [54], which preserves the fundamental dynamics of CAVSIM [87], is used to prove the boundedness of the multi-variable UCG process. For this purpose, the model of [54] is slightly modified to represent the MIMO UCG process model. Finally, the simulation results are presented to compare the performance of conventional SMC and DSMC.

The basic theory of SMC is explained in section 6.1. The control design and approximate model of CAVSIM are described in section 6.2 and section 6.3, respectively. The implementation of designed controllers on CAVSIM is explained in section 6.4. In section 6.5, simulation results are discussed, and finally the chapter is concluded in section 6.6.

6.1 Introduction

The SMC has emerged as a preferred robust control technique for the complex high order nonlinear systems operating under external perturbations and uncertainty conditions. The major attributes of this technique are the insensitivity to external disturbances and parametric uncertainties, which eliminates the need for exact modeling. Moreover, it is suitable for multi-variable systems, and the control action can be easily implemented through discontinuous elements like controlled switches or relay [124–126]. In recent developments, the key concerns in SMC technique are the elimination of chattering, improvement in the dynamic performance of the closed-loop system, and adaptability in the uncertain system have been addressed. Owing to the distinguishing features of SMC, it has been employed in numerous applications like industrial process control, robotics, motion control problems, aerospace, electric drives and power electronics applications.

The primary step in the development of SMC based control system is to design a switching surface in order to meet the desired closed-loop performance. In the literature, this switching surface is also called the switching manifold or sliding surface. Then an appropriate control law is selected to keep the system states on sliding surface in the presence of uncertainties and external disturbances. The two phases involved in a SMC are the *Reaching phase* and *Sliding phase* [126]. During the reaching phase, the system states are driven towards the predefined sliding manifold by the discontinuous control law. After reaching the sliding surface, the sliding phase begins in which the feedback loop structure alters adaptively and the same control law forces the system dynamics to slide towards an equilibrium point

along the sliding surface. The constrained motion of SMC during the sliding phase is termed as *sliding mode*. For any m -dimensional system having n -dimensional control inputs, the system evolves with $m - n$ states during the sliding mode. This order reduction provides invariance to the external disturbances and parametric variations. Moreover, it reduces the system complexity by decoupling the system motion into independent components of lower dimension [126]. The design strategy is discussed in the subsequent sections.

6.1.1 SMC Design Procedure

Consider a nonlinear affine control system

$$\dot{x} = f(x, t) + B(x, t)u, \quad (6.1)$$

where $f \in \mathfrak{R}^n$ is a nonlinear function of the states, $x \in \mathfrak{R}^n$ is the system states vector, $B \in \mathfrak{R}^{n \times m}$ is the input matrix, and $u \in \mathfrak{R}^m$ is the inputs vector. A set of switching surfaces φ is defined as

$$\varphi = \{x \in \mathfrak{R}^n : \varphi(x) = [\varphi_1(x), \dots, \varphi_m(x)]^T\}. \quad (6.2)$$

Then the conventional SMC design can be manifested by two sub problems of lower dimensions.

6.1.1.1 Switching Surface Design

The design of switching surface is based on the desired dynamical properties of the closed-loop system. The *sliding mode* is the motion of the system as it slides along the surface, and is defined by [126]

$$\varphi(\mathbf{x}) = Z\mathbf{x} = 0 \quad (6.3)$$

where $Z = \frac{\partial \varphi}{\partial x}$ is an $m \times n$ matrix of gradients of sliding variables. Generally, the choice of sliding surface is application specific.

6.1.1.2 Existence of Sliding Mode

To ensure the existence of sliding mode, the control law is designed such that it drags the system's state to the sliding manifold in a finite time. Moreover, the controller retains the system in the sliding mode in the presence of parametric variations, external disturbances, and modeling uncertainties. For this purpose, a condition is imposed on the control law, known as the reachability condition [125, 126]. The condition for sliding mode to exist is usually determined by performing the quadratic stability analysis in the presence of uncertainties. The convergence of sliding surfaces can be determined by choosing a positive definite Lyapunov functional and its time derivative is computed as

$$V = \frac{1}{2}\varphi^T\varphi, \tag{6.4}$$

$$\dot{V} = \varphi^T\dot{\varphi}. \tag{6.5}$$

The control law is designed to ensure the reachability condition i.e.

$$\varphi^T\dot{\varphi} < 0, \tag{6.6}$$

which guarantees the finite time convergence to the sliding manifold. Generally, the control law \mathbf{u} is given as

$$\mathbf{u} = \mathbf{u}_c + \mathbf{u}_d, \tag{6.7}$$

where u_c is the continuous or equivalent control, and it is found by solving $\dot{\varphi} = Zf + ZBu_c = 0$

$$u_c = -[Z(x)B(x)]^{-1}Z(x)f(x). \tag{6.8}$$

In (6.7), u_d represents the discontinuous term that ensures the finite time convergence to the chosen surface in the presence of disturbances and modeling inaccuracies. It is usually taken as $-M\text{sign}(\varphi)$, where $M \in \mathfrak{R}^+$.

6.1.2 Chattering Problem

The design of conventional SMC exhibits sustained oscillations having finite amplitude and frequency, and this undesired phenomena is known as *chattering*, which is a major hindrance in the implementation of SMC. There are two reasons which cause the chattering phenomena: ignoring fast dynamics in the model and utilization of digital controllers having finite sampling rate. The un-modeled dynamics having small time constants are excited by the fast switching of sliding mode controllers (SMCs), which produces the high frequency sustained oscillations. The chattering phenomena has harmful effects like high wear of moving mechanical parts, low control accuracy, and high heat losses in power circuits. The researchers have developed various techniques to address the chattering issue, such as high order SMC and DSMC.

6.2 Sliding Mode Control Design for the UPT Field

In this section, the linear model identified in (4.8) and (4.9) is employed to design the multi-variable conventional SMC and DSMC for the UPT field. The steps involved in the design of controllers are briefly outlined below.

1. Plant scaling is performed as a preliminary step prior to the controller design for a multi-variable system, which is described in section 4.3.1.
2. The regular form is formulated to design the conventional SMC and DSMC, and it is also used to analyze the zero dynamics of the linear model.
3. The sliding variable vector $\varepsilon^T = \begin{bmatrix} \varepsilon_1 & \varepsilon_2 \end{bmatrix}^T$ is selected such that the sliding mode exhibits the desired properties.
4. The continuous part \mathbf{u}_{eq} is computed by taking the time derivative of ε and putting it equal to zero.

5. The discontinuous control is selected to enforce sliding mode by satisfying the condition: $\varepsilon \dot{\varepsilon} < 0$, which implies $\dot{\mathbf{u}}$ depends on the discontinuous control.
6. The zero dynamics of CAVSIM has been analyzed, and finally the controllers are implemented on CAVSIM.

6.2.1 Formulation of Regular Form

The identified state-space model in (4.8) and (4.9) is given as

$$\dot{\mathbf{x}} = A\mathbf{x} + B\mathbf{u}, \tag{6.9}$$

$$\mathbf{y} = C\mathbf{x}, \tag{6.10}$$

where $\mathbf{x} \in \mathfrak{R}^{n \times 1}$, $\mathbf{u} \in \mathfrak{R}^{m \times 1}$, $\mathbf{y} \in \mathfrak{R}^{p \times 1}$, $A \in \mathfrak{R}^{n \times n}$, $B \in \mathfrak{R}^{n \times m}$, $C \in \mathfrak{R}^{p \times n}$, and $n = 6, m = p = 2$. The eigenvalue placement problem in the framework of sliding mode control is solved by representing the linear system in a regular form, which makes the design simple [127]. The matrix B is partitioned by reordering the state vector components such as $B = \begin{bmatrix} B_1 \\ B_2 \end{bmatrix}$, where $B_1 \in \mathfrak{R}^{(n-m) \times m}$, $B_2 \in \mathfrak{R}^{m \times m}$ with $\det B_2 \neq 0$ and $C = \begin{bmatrix} C_1 & C_2 \end{bmatrix}$, where $C_1 \in \mathfrak{R}^{p \times (n-m)}$, $C_2 \in \mathfrak{R}^{p \times m}$ with $\det C_2 \neq 0$. The reordered states (\mathbf{X}) are decomposed into two vectors $\mathbf{X}_1 = \begin{bmatrix} x_2 & x_3 & x_4 & x_6 \end{bmatrix}^T$ and $\mathbf{X}_2 = \begin{bmatrix} x_1 & x_5 \end{bmatrix}^T$ such that (6.9), and (6.10) become

$$\dot{\mathbf{X}} = \begin{bmatrix} \dot{\mathbf{X}}_1 \\ \dot{\mathbf{X}}_2 \end{bmatrix} = A \begin{bmatrix} \mathbf{X}_1 \\ \mathbf{X}_2 \end{bmatrix} + \begin{bmatrix} B_1 \\ B_2 \end{bmatrix} \mathbf{u}, \tag{6.11}$$

where, $A = \begin{bmatrix} A_{11} & A_{12} \\ A_{21} & A_{22} \end{bmatrix}$ is the reordered system matrix, $A_{11} \in \mathfrak{R}^{(n-m) \times (n-m)}$, $A_{12} \in \mathfrak{R}^{(n-m) \times m}$, $A_{21} \in \mathfrak{R}^{p \times (n-m)}$, and $A_{22} \in \mathfrak{R}^{p \times m}$, and

$$\mathbf{y} = C_1\mathbf{X}_1 + C_2\mathbf{X}_2, \tag{6.12}$$

$$\mathbf{X}_2 = C_2^{-1}(\mathbf{y} - C_1\mathbf{X}_1). \tag{6.13}$$

By differentiating (6.12), and using (6.11) and (6.13), the matrix form of output and state vectors is represented as

$$\begin{bmatrix} \dot{\mathbf{X}}_1 \\ \dot{\mathbf{y}} \end{bmatrix} = \begin{bmatrix} \alpha_{11} & \alpha_{12} \\ \alpha_{21} & \alpha_{22} \end{bmatrix} \begin{bmatrix} \mathbf{X}_1 \\ \mathbf{y} \end{bmatrix} + \begin{bmatrix} B_1 \\ CB \end{bmatrix} u, \quad (6.14)$$

where, $\alpha_{11} \in \mathfrak{R}^{(n-m) \times (n-m)}$, $\alpha_{12} \in \mathfrak{R}^{(n-m) \times m}$, $\alpha_{21} \in \mathfrak{R}^{p \times (n-m)}$, $\alpha_{22} \in \mathfrak{R}^{p \times m}$, and can be represented in a block matrix α as

$$\alpha = \begin{bmatrix} \alpha_{11} & \alpha_{12} \\ \alpha_{21} & \alpha_{22} \end{bmatrix}, \text{ where,}$$

$$\alpha_{11} = \left[A_{11} - A_{12}C_2^{-1}C_1 \right], \quad \alpha_{12} = \left[A_{12}C_2^{-1} \right],$$

$$\alpha_{21} = \left[C_1A_{11} + C_2A_{21} - C_1A_{12}C_2^{-1}C_1 - C_2A_{22}C_2^{-1}C_1 \right],$$

$$\alpha_{22} = \left[C_1A_{12}C_2^{-1} + C_2A_{22}C_2^{-1} \right], \quad CB = C_1B_1 + C_2B_2.$$

The nonsingular coordinate transformation

$$Q = \begin{bmatrix} I_{n-m} & -B_1(CB)^{-1} \\ O_{p \times (n-m)} & I_p \end{bmatrix}, \quad (6.15)$$

is applied on (6.14), and the transformed states become

$$\begin{bmatrix} \mathbf{z} \\ \mathbf{y} \end{bmatrix} = Q \begin{bmatrix} \mathbf{X}_1 \\ \mathbf{y} \end{bmatrix}. \quad (6.16)$$

The regular form is obtained by differentiating the above equation, and it is given as

$$\begin{bmatrix} \dot{\mathbf{z}} \\ \dot{\mathbf{y}} \end{bmatrix} = Q\alpha Q^{-1} \begin{bmatrix} \mathbf{z} \\ \mathbf{y} \end{bmatrix} + Q \begin{bmatrix} B_1 \\ CB \end{bmatrix} \mathbf{u},$$

$$= R \begin{bmatrix} \mathbf{z} \\ \mathbf{y} \end{bmatrix} \begin{bmatrix} 0 \\ CB \end{bmatrix} \mathbf{u},$$

where $R = Q\alpha Q^{-1}$, and the above equation can be expressed as

$$\begin{bmatrix} \dot{\mathbf{z}} \\ \dot{\mathbf{y}} \end{bmatrix} = \begin{bmatrix} R_{11} & R_{12} \\ R_{21} & R_{22} \end{bmatrix} \begin{bmatrix} \mathbf{z} \\ \mathbf{y} \end{bmatrix} + \begin{bmatrix} 0 \\ CB \end{bmatrix} \mathbf{u}, \quad (6.17)$$

where, $R_{11} \in \mathfrak{R}^{(n-m) \times (n-m)}$, $R_{12} \in \mathfrak{R}^{(n-m) \times m}$, $R_{21} \in \mathfrak{R}^{p \times (n-m)}$, and $R_{22} \in \mathfrak{R}^{p \times m}$. The internal dynamics from (6.17) is given as

$$\dot{\mathbf{z}} = R_{11}\mathbf{z} + R_{12}\mathbf{y}, \quad (6.18)$$

where, $R_{11} = \begin{bmatrix} -0.81 & -0.04 & -0.27 & 0 \\ 0 & -0.19 & -0.07 & 1.69 \\ 0 & 0.12 & 0 & 0 \\ 0 & 0 & 0 & -1.02 \end{bmatrix}$.

The matrix R_{11} in (6.18) is Hurwitz which shows that the zero dynamics is stable.

6.2.2 Design of Conventional SMC

The first step in the designing of SMC is to choose an appropriate sliding surface. The sliding variable vector $\varepsilon^T = [\varepsilon_1 \ \varepsilon_2]^T$ is selected to keep the syngas heating value and flow rate at the desired levels i.e. $\mathbf{y}_d^T = [y_{d1} \ y_{d2}]^T$. The desired objectives can be achieved when $\varepsilon \rightarrow 0$, therefore,

$$\varepsilon = \mathbf{y} - \mathbf{y}_d. \quad (6.19)$$

The equivalent control \mathbf{u}_{eq} of SMC is found by computing the time derivative of ε and then solving $\dot{\varepsilon} = 0$, which yields

$$\mathbf{u}_{eq} = (CB)^{-1} (-R_{21}\mathbf{z} - R_{22}\mathbf{y} + \dot{\mathbf{y}}_d), \quad (6.20)$$

$$\mathbf{u} = -M \text{sign}(\varepsilon) + (CB)^{-1} (-R_{21}\mathbf{z} - R_{22}\mathbf{y} + \dot{\mathbf{y}}_d), \quad (6.21)$$

where, $M = \begin{bmatrix} M_1 & 0 \\ 0 & M_2 \end{bmatrix}$ and $M_1, M_2 \in \mathfrak{R}^+$. The sliding variables will converge to zero only iff $\varepsilon^T \dot{\varepsilon} < 0$. A positive definite Lyapunov function is chosen to determine the convergence of sliding surfaces, and its time derivative is calculated as

$$\begin{aligned} V &= \frac{1}{2} \varepsilon^T \varepsilon, \\ \dot{V} &= \varepsilon^T \dot{\varepsilon}, \\ &= \varepsilon^T (\dot{\mathbf{y}} - \dot{\mathbf{y}}_d) = \varepsilon^T (R_{21}\mathbf{z} + R_{22}\mathbf{y} + CB\mathbf{u} - \dot{\mathbf{y}}_d), \\ &= \varepsilon^T (R_{21}\mathbf{z} + R_{22}\mathbf{y} - CBM \text{sign}(\varepsilon) + \mathbf{u}_{eq} - \dot{\mathbf{y}}_d), \\ &= -F_o |\varepsilon|, \end{aligned}$$

where F_o is a non-symmetric matrix and the eigenvalues of $(F_o + F_o^T)/2$ are positive which shows that it is a positive definite matrix. Thus, the derivative of Lyapunov function is negative definite, and hence sliding mode exists. Moreover, when $\varepsilon = \mathbf{0}$, the control law given by (6.21) is reduced to $\mathbf{u} = \mathbf{u}_{eq}$, as $-M \text{sign}(\varepsilon) = 0$, since $\text{sign}(0) = 0$. Thus, it can be inferred from (6.20) that the boundedness of control inputs is a function of \mathbf{z} , \mathbf{y} and \mathbf{y}_d . As the internal dynamics in (6.17) is stable and the desired outputs are also bounded, hence the control inputs are bounded and, therefore, the design of SMC is valid.

6.2.3 Design of DSMC

The conventional SMC is prone to chattering, which causes wear and tear of the actuators, reduces accuracy of the controller and excites the un-modeled dynamics. To reduce chattering DSMC is designed, and the block diagram of closed-loop UCG system with DSMC is shown in Fig 6.1. In DSMC, sliding mode is enforced in the derivative of the control inputs, and an integrator is used to obtain the control inputs. This leads to the continuous control signals, and chattering is reduced significantly. The overall DSMC control law is given as

$$\dot{\mathbf{u}} = \mathbf{v}, \tag{6.22}$$

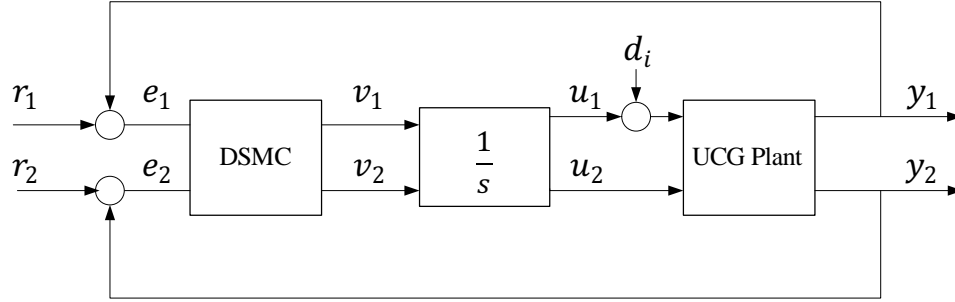


FIGURE 6.1: Block Diagram of closed-loop UCG system with DSMC

where, \mathbf{v} is to be selected. The sliding variable vector φ is selected to maintain the heating value and flow rate of syngas at the desired levels i.e. $\mathbf{y}_d^T = [y_{d1} \ y_{d2}]^T$. The desired objectives are achieved when $\varphi \rightarrow 0$, therefore,

$$\varphi = \dot{\varepsilon} + \kappa_1 \varepsilon, \quad \text{and} \quad \varepsilon = \mathbf{y} - \mathbf{y}_d. \quad (6.23)$$

Now the continuous part of control input vector \mathbf{v} is obtained by taking the time derivative of φ , and by solving $\dot{\varphi} = 0$.

$$\begin{aligned} \dot{\varphi} &= \ddot{\varepsilon} + \kappa_1 \dot{\varepsilon} = 0, \\ &\Rightarrow \Theta_1 \mathbf{z} + \Theta_2 \mathbf{y} + \Theta_3 \mathbf{u} + \Theta_4 + \mathbf{v}_{\text{eq}} = 0, \end{aligned} \quad (6.24)$$

$$\mathbf{v}_{\text{eq}} = (CB)^{-1} (-\Theta_1 \mathbf{z} - \Theta_2 \mathbf{y} - \Theta_3 \mathbf{u} - \Theta_4), \quad (6.25)$$

where, $\mathbf{v}_{\text{eq}} = \dot{\mathbf{u}}_{\text{eq}}$, $\Theta_1 = R_{21}R_{11} + R_{22}R_{21} + \kappa_1 R_{21}$, $\Theta_2 = R_{21}R_{12} + R_{22}^2 + \kappa_1 R_{22}$, $\Theta_3 = CB(R_{22} + \kappa_1)$ and $\Theta_4 = -\ddot{\mathbf{y}}_d - \kappa_1 \dot{\mathbf{y}}_d$. While κ_1 is a positive definite diagonal matrix, and it is given as

$$\kappa_1 = \begin{bmatrix} 0.1 & 0 \\ 0 & 0.3 \end{bmatrix}$$

Hence, the over-all DSMC control law (\mathbf{v}) and $\dot{\varphi}$ becomes

$$\dot{\mathbf{u}} = \mathbf{v} = (CB)^{-1} (-\Theta_1 \mathbf{z} - \Theta_2 \mathbf{y} - \Theta_3 \mathbf{u} - \Theta_4) - N \text{sign}(\varphi) \quad (6.26)$$

$$\dot{\varphi} = -N \text{sign}(\varphi),$$

where $N = \begin{bmatrix} N_1 & 0 \\ 0 & N_2 \end{bmatrix}$ and $N_1, N_2 \in \mathfrak{R}^+$. As $\varphi^T \dot{\varphi} = -N|\varphi| < 0$, hence, the sliding

mode exists.

The control input vector \mathbf{u} is obtained after integrating (6.26), as shown in Fig. 4.1. When the sliding mode is established i.e $\varphi = 0$, then, with positive definite diagonal matrix κ_1 , the tracking error vector given by (6.24) converges to the origin asymptotically, which implies $\mathbf{y} \rightarrow \mathbf{y}_d$. The matrix R_{11} in (6.18) is Hurwitz which shows that the zero dynamics is stable. The boundedness of states show that \mathbf{v} is also bounded, as Θ_3 in (6.22) is Hurwitz and outputs are also bounded. As the zero dynamics and the control inputs are bounded, therefore, the design of DSMC is valid.

6.3 Approximate Model of CAVSIM

The stability and tracking objective of the linear system have been achieved by using the control design given in (6.26). Now, it is desired to implement the controller on the actual CAVSIM and to prove the stability of the zero dynamics of CAVSIM. Due to the complex dynamics of the CAVSIM model, the 1D packed model of [54] is used to approximate CAVSIM. The fundamental dynamics of both the models are based on the laws of mass and energy conservations of solids and gases. However, the model of [54] is simpler but less accurate. In order to prove the stability of the zero dynamics the model of [54] is modified by incorporating the expression for the flow rate of the produced gas (y_2).

6.3.1 Model Equations

The model comprises of two solids coal and char, and eight gases: CO, CH₄, H₂, CO₂, H₂O(g), N₂, O₂ and C_nH_m. The model is simplified by considering only the coal pyrolysis, char oxidation, and steam gasification reactions [55].The fundamental

conservation laws of mass and energy are used to derive the mass and energy balance expressions of solids and gases. The interaction between solids and gases at the point of reaction has been ignored, and the generated heat source of chemical reactions are represented separately for solids and gases. The gases have fast time-domain characteristics as compared to solids, and therefore, a pseudo/quasi steady state approximation is assumed in the model formulation. The gas phase equations are derived in terms of ODEs due to pseudo/quasi steady state approximation.

6.3.1.1 Solid Phase Mass Balance

The rate of change of solid density is determined as a function of different chemical reactions rates, and are given as

$$\frac{\partial \rho_1}{\partial t} = -M_1 R_1, \tag{6.27}$$

$$\rho_1(0, x_o) = \rho_{10}(x_o), \quad 0 \leq x \leq L,$$

$$\frac{\partial \rho_2}{\partial t} = M_2 [|a_{s_2,1}| R_1 - R_2(u) - R_3(u)], \tag{6.28}$$

$$\rho_2(0, x_o) = \rho_{20}(x_o), \quad 0 \leq x_o \leq L,$$

where ρ_j represents the j^{th} solid density (kg/cm³) at point (t, x_o) . While x_o and t are the variables for length (cm) and time (s), respectively. M (kg/mol) is the molecular weight of j^{th} solid, $\rho_j(0, x_o)$ is the initial density distribution of j^{th} solid, and L is the length (cm) of reactor. The stoichiometric coefficient of solid j in reaction i is denoted by $a_{s_2,1}$, and R_i is the reaction rate (mol/cm³/s) of i^{th} chemical reaction.

6.3.1.2 Solid Phase Energy Balance

The variation in solid temperature distribution profile caused by the heat of chemical reactions and heat transfer due to conduction and convection phenomena are shown by a parabolic heat equation, and given as

$$\frac{\partial T_s}{\partial t} = \frac{B \frac{\partial^2 T_s}{\partial x^2} + h(T_o - T_s) - q_1 R_1 - q_2 R_2(u) - q_3 R_3(u)}{(c p_1 \rho_1 + c p_2 \rho_2)}, \quad (6.29)$$

$$T_s(0, x_o) = T_{s_0}(x_o), \quad 0 \leq x_o \leq L,$$

$$\frac{\partial T_s}{\partial x}(t, 0) = \frac{\partial T_s}{\partial x}(t, L) = 0, \quad t \geq 0,$$

where T_s represents the solid temperature (K) at point (t, x_o) , and T_o is gas temperature (K). B is a constant depending on thermal conductivity (cal/cm/s/K) of solids and coal porosity, q_i , c_{p_i} and h represent the heat of reaction i (cal/mol), the heat capacity (cal/g/K) of solids, and the heat transfer coefficient (cal/s/K/cm³), respectively.

6.3.1.3 Gas Phase Mass Balance

The concentration of gas varies along the length of UCG gasifier due to the superficial gas phase velocity and the chemical reactions. The superficial velocity for porous media is defined as a hypothetical velocity of gas phase determined over whole cross sectional area by ignoring the solid phase. The mass balance of gas phase is given by

$$\frac{dC_i}{dx} = \frac{1}{v_g} \left(-C_i \frac{dv_g}{dx} + \sum_{j=1}^3 a_{ij} R_j \right),$$

where C_i , v_g and a_{ij} represent the concentration (mol/cm³) of i^{th} gas, superficial gas velocity (cm/s), and the stoichiometric coefficient of gas i in reaction j , respectively.

6.3.1.4 Gas Phase Energy and Momentum Balance

The heat of water gas shift reaction and convective heat transfer phenomena affects the temperature of gases. Due to quasi-steady state assumption, the accumulation terms are neglected and simplified expression is given as

$$\frac{dT_o}{dx} = -\frac{h}{v_g C_g} (T_o - T_s). \quad (6.30)$$

The momentum balance for solid species is not considered in the model as they are assumed stationary. The momentum balance for gas phase is calculated by Darcy's law, and given as

$$\frac{dP}{dx} = -\frac{v_g \mu}{2K}, \tag{6.31}$$

where P , μ and K are the gas pressure (atm), viscosity ($Pa.s$), and permeability coefficient (cm^2), respectively.

6.3.1.5 Chemical Kinetics

The chemical kinetics of the process are simplified by considering only pyrolysis, char oxidation, and steam gasification chemical reactions, which are presented in Table 6.1. CH_aO_b and $CH_{\bar{a}}O_{\bar{b}}$ represent the molecular formulas for the coal and char, respectively. While a , b , \bar{a} and \bar{b} are determined by the ultimate analysis of coal and char, respectively.

The chemical reaction rates are taken from [19, 96] and given as

- **Coal pyrolysis reaction rate**

$$R_1 = 5 \frac{\rho_1}{M_1} \exp\left(\frac{-6039}{T_s}\right). \tag{6.32}$$

- **Char oxidation reaction rate**

$$R_2 = f_{R_2}(u_1, u_2) R_{C_2}, \tag{6.33}$$

$$f_{R_2}(u_1, u_2) = \frac{1}{u_1 + u_2},$$

$$R_{C_2} = \frac{9.55 \times 10^8 \rho_2 P v_g C_7 \exp\left(\frac{-22142}{T_s}\right) k_y}{M_2 k_y \sqrt{T_s} + 9.55 \times 10^8 \rho_2 P \exp\left(\frac{-22142}{T_s}\right)},$$

$$C_7 = 0.21 \frac{u_2}{v_g} \exp\left(-\frac{|a_{7,2}|}{u_1 + u_2} \int_0^{x_o} R_{C_2} dx_o\right).$$

TABLE 6.1: Chemical reactions considered in the model [96]

| Sr Chemical equations |
|--|
| 1. Pyrolysis |
| $CH_aO_b \rightarrow a_{s2,1} CH_{\bar{a}}O_{\bar{b}} + a_{1,1} CO + a_{2,1} CO_2 + a_{3,1}H_2 + a_{4,1} H_2O + a_{5,1} CH_4 + a_{8,1} C_9H_c$ |
| 2. Char Oxidation |
| $CH_{\bar{a}}O_{\bar{b}} + a_{7,2} O_2 \rightarrow a_{2,2} CO_2 + a_{4,2} H_2O$ |
| 3. Steam gasification |
| $CH_{\bar{a}}O_{\bar{b}} + a_{4,3} H_2O \rightleftharpoons a_{1,3} CO + a_{3,3} H_2$ |

where u_1, u_2 are control inputs, k_y is the mass transfer coefficient (mol/cm³/s), and C_7 represents O_2 concentration (mol/cm³) distribution along x_o .

- **Steam gasification reaction rate**

$$R_3 = f_1(u_1, u_2)R_{C_3}, \quad (6.34)$$

$$f_1(u_1, u_2) = \frac{u_1}{u_1 + u_2},$$

$$R_{C_3} = \frac{k_y P^2 \rho_2 E_1}{P^2 E_1 \rho_2 + k_y M_2 (P + E_2)^2},$$

$$E_1 = \exp\left(5.052 - \frac{12908}{T_s}\right),$$

$$E_2 = \exp\left(-22.216 + \frac{24880}{T_s}\right).$$

6.3.1.6 Outputs Equations

The syngas collected at the production well is sent to the gas analyzer which provides the molar fraction and flow rate of syngas species. The two outputs i.e. the heating value and flow rate of syngas are calculated as

$$y_1 = m_1 H_1 + m_2 H_2 + m_3 H_3 + m_4 H_4, \quad (6.35)$$

$$m_i = 100 \frac{C_i(L)}{\tilde{C}_T(L)}, \quad \tilde{C}_T(L) = \sum_{i=1, i \neq 4}^8 C_i(L),$$

$$y_2 = \tilde{C}_T v_g, \quad (6.36)$$

where y_i with $i = 1, 2$ represents the heating value and flow rate of the syngas, respectively, H_i and m_i are the heat of combustion, molar fraction percentage of syngas species CO, CH₄, H₂ and C_nH_m and total concentration of syngas, respectively. While \tilde{C}_T and v_g represent the total concentration without steam and velocity of syngas.

The solution for CO, CH₄, H₂, CO₂ and C_nH_m at $x_o = L$ with $C_i(0) = 0$ is [96]

$$C_i(L) = \frac{1}{v_g} \sum_{j=1}^3 a_{i,j} \int_0^L R_j dx_o. \tag{6.37}$$

O₂ contributes only in char oxidation reaction and N₂ is an inert gas and it does not participate in any chemical reaction. Therefore, the solution for the concentration of O₂ $C_{O_2}(L)$, with $C_{O_2}(0) = 0.21 \frac{u_2}{v_g}$ and N₂ is

$$\frac{dC_{O_2}}{dx} = -\frac{|a_{7,2}|}{v_g} R_2,$$

$$C_{O_2}(L) = 0.21 \frac{u_2}{v_g} \exp\left(-\frac{|a_{7,2}|}{u_1 + u_2} \int_0^L C R_2 dx_o\right), \tag{6.38}$$

$$C_{N_2}(L) = C_{N_2}(0) = \frac{1}{v_g} (0.79u_2 - 0.21u_1u_2). \tag{6.39}$$

Hence, (6.35) and (6.36) become

$$y_1 = \frac{N_1 + f_1(u_1, u_2)N_2}{D1 + f_1(u_1, u_2)D_2 + f_2(u_1, u_2)}, \tag{6.40}$$

$$y_2 = D1 + f_1(u_1, u_2)D_2 + f_2(u_1, u_2), \tag{6.41}$$

where, $f_1(u_1, u_2) = \frac{u_1}{u_1 + u_2}$, $f_2(u_1, u_2) = \frac{0.79u_2 - 0.21u_1u_2}{v_g}$,

$$N_1 = 100\alpha \int_0^L R_1 dx_o, \quad N_2 = 100\beta \int_0^L R_{C3} dx_o,$$

$$D_1 = \gamma \int_0^L R_1 dx_o + \zeta \int_0^L R_2 dx_o, \quad D_2 = +\eta \int_0^L R_{C3} dx_o,$$

$$\alpha = \frac{1}{v_g} (a_{11}H_1 + a_{31}H_3 + a_{51}H_5 + a_{81}H_8),$$

$$\begin{aligned}\beta &= \frac{1}{v_g} (a_{13}H_1 + a_{33}H_3), \\ \gamma &= \frac{1}{v_g} (a_{11} + a_{21} + a_{31} + a_{51} + a_{81}), \\ \eta &= \frac{1}{v_g} (a_{13} + a_{33}), \quad \zeta = \frac{a_{2,2}}{v_g}.\end{aligned}$$

6.3.2 Stability of Zero Dynamics of CAVSIM

As the DSMC in (6.26) tracks y_1 and y_2 to the desired trajectories given by \mathbf{y}_d . Now it is essential to determine the stability of the zero dynamics for CAVSIM. It is evident from (6.40) and (6.41) that both the outputs are directly dependent on control inputs u_1 and u_2 , hence the relative degree of the system is 0. Therefore, all the solid PDEs given in (6.27)-(6.29) constitute the zero dynamics of the system with $u = u_{DSMC}$ which makes $\varphi = 0$ at $t = t_{ss}$. The states are stable iff the reaction rates and control inputs are bounded. While the reaction rates in (6.32), (6.33) and (6.34) are the functions of control inputs u_1 , u_2 , solid temperature T_s and the densities of coal and char (ρ_1 , ρ_2). As given in [96], the solution of (6.27) is

$$\begin{aligned}\rho_1(t, x_o) &= \rho_1(0, x_o) \exp(-5E_3t), \\ E_3(x_o) &\leq \exp\left\{\frac{-6039}{\max_{t \geq 0} T_s(t, x)}\right\}, \quad 0 < T_{smin} \leq T_s(t, x_o).\end{aligned}\tag{6.42}$$

It is important to note that for $0 < T_{smin} \leq T_s(t, x_o) \leq \infty$, the distribution $\rho_1(0, x_o)$ exponentially decays with time, and ρ_1 is stable. The stability of ρ_2 can also be inferred from the stability of ρ_1 , because ρ_1 is decomposed by coal pyrolysis reaction to yield ρ_2 and product gases, therefore, for law of conservation of mass to hold, ρ_2 is bounded [96].

According to [96], the heat equation in (6.29) can be approximated with the following linear PDE as

$$\begin{aligned} \dot{T}_s &= \frac{1}{\bar{C}_s} [BT_s'' - hT_s + hT(x_o) + \mathcal{G}(t, x_o)], \\ |\mathcal{G}(t, x_o)| &\leq \mathcal{G}_0, \mathcal{G}_0 \in \mathfrak{R}^+, \end{aligned} \tag{6.43}$$

where $\dot{T}_s = \frac{\partial T_s}{\partial t}$, $T_s' = \frac{\partial T_s}{\partial x_o}$, $T_s'' = \frac{\partial^2 T_s}{\partial x_o^2}$ and $\mathcal{G}(t, x_o)$ is a linear function and an upper bound on the heat source term (H_s). The solution of above equation can be represented as

$$T_s = \Delta T_s + T_{sx_o} + T_{sd}, \tag{6.44}$$

where ΔT_s corresponds to the solution without the inputs $T(x_o)$ and \mathcal{G} , T_{sx_o} is the forced component defined by $T(x)$ and T_{sd} is the forced part which depends on the disturbance $\mathcal{G}(t, x_o)$. Now the boundedness of all the solution components in (6.44) is investigated independently. The stability of homogeneous equation is given as

$$\begin{aligned} \bar{C}_s \Delta \dot{T}_s &= B \Delta T_s'' - h \Delta T_s, \\ \Delta T_s(0, x_o) &= \Delta T_{s_0}(x_o), \Delta T_s'(t, 0) = \Delta T_s'(t, L) = 0. \end{aligned}$$

By selecting a positive definite Lyapunov functional as

$$V = \frac{\bar{C}_s}{2} \int_0^L \Delta T_s^2 dx_o > 0 \quad \text{if } s \neq 0.$$

Then taking its time derivative

$$\begin{aligned} \dot{V} &= B \int_0^L \Delta T_s \Delta T_s'' dx_o - h \int_0^L \Delta T_s^2 dx_o, \\ &= -B \int_0^L \Delta T_s'^2 dx_o - \frac{2h}{\bar{C}_s} V. \end{aligned}$$

Now using Poincare Inequality [128]: for any continuously differentiable ΔT_s on $[0, L]$

$$\int_0^L \Delta T_s^2 dx_o \leq 2\Delta T_s^2(L) + 4 \int_0^L \Delta T_s'^2 dx_o.$$

After using $\Delta T_s'(t, L) = 0 \implies \frac{1}{2}\Delta T_s^2(L) = \Omega \in \mathfrak{R}^+$. The expression for \dot{V} becomes

$$\begin{aligned}\dot{V} &\leq -\alpha V + \Omega, \\ V &\leq \frac{\Omega}{\alpha} \left(1 - \exp(-\alpha t)\right), \\ \alpha &= 2 \frac{B+h}{\bar{C}_s}.\end{aligned}$$

The L_2 norm of ΔT_s is defined as

$$\|\Delta T_s(t)\| = \left(\int_0^L \Delta T_s(t, x_o)^2 dx \right).$$

Therefore, L_2 norm of ΔT_s is bounded and given by

$$\begin{aligned}\|\Delta T_s(t)\| &\leq -\zeta \left(1 - \exp\left(\frac{-\alpha}{2}t\right)\right) + \|\Delta T_{s_0}\| \exp\left(\frac{-\alpha}{2}t\right), \\ \zeta &= \sqrt{\frac{2\Omega}{\alpha \bar{C}_s}}, \quad \Delta T_{s_0}(x_o) = \Delta T_s(0, x_o).\end{aligned}$$

The following boundary value problem is solved to obtain T_{sx_o}

$$\begin{aligned}BT_{sx_o}'' - hT_{sx} + hT(x_o) &= 0, \\ T_{sx_o}'(t, 0) = T_{sx}'(t, L) &= 0, \\ T(x_o) &= T(0) \exp(-\lambda x) + \lambda \int_0^{x_o} \exp\{-\lambda(x_o - \mathcal{X})\} T_s(\mathcal{X}) d\mathcal{X}.\end{aligned}$$

As given in [96], the solution is

$$\begin{aligned}T_{sx_o} &= -\frac{\Lambda}{\lambda^2 B - h} \exp(-\lambda x_o), \\ \lambda &= \frac{h}{v_g C_g}, \\ \Lambda &= h [T(0) + T_s(0, 0)].\end{aligned}\tag{6.45}$$

Therefore, the forced response T_{sx_o} due to $T(x_o)$ is also bounded. As the disturbance \mathcal{G} is the linear approximation of heat source term, therefore, T_{sd} is also

bounded. The boundedness of T_{sd} can be shown if it is represented in the modal form. All the solution components of the linear heat equation are bounded, therefore, T_s stays bounded throughout the process of gasification. As described in section 6.2.3 that \mathbf{u} is bounded, the results in (6.42) and the boundedness of T_s show that the zero dynamics of the UCG process is bounded and the design of DSMC is valid.

6.4 Implementation of SMC Controllers on the CAVSIM

The implementation scheme shown in Fig. 5.12 is also used here to implement the sliding mode controllers on actual system. As the SMCs have been designed from a scaled model, therefore, the scaling matrices (D_u, D_e, D_{d_i}) given in (4.13) and the nominal operating points of inputs and outputs in (4.1) must also be included in the implementation scheme, as described for the H_∞ controller.

As described in section 6.2.1, the nonsingular coordinate transformation T in (6.15) is applied on the actual system to design the continuous part of the controllers. Thus, the inverse transformation is applied to obtain the controllers in terms of actual states \mathbf{X}_1 and \mathbf{X}_2 . The SMC and DSMC control laws in terms of actual states are determined in the subsequent sections.

6.4.1 SMC Implementation

By using (6.15), the equivalent control of conventional SMC in terms of actual states is

$$\begin{aligned} \mathbf{u}_{\text{eq}} &= [CB]^{-1} \left(\begin{bmatrix} -R_{21} & -R_{22} \end{bmatrix} \begin{bmatrix} \mathbf{z} \\ \mathbf{y} \end{bmatrix} + \begin{bmatrix} \dot{y}_{d1} \\ \dot{y}_{d2} \end{bmatrix} \right), \\ &= [CB]^{-1} \begin{bmatrix} -R_{21} & -R_{22} \end{bmatrix} Q \begin{bmatrix} \mathbf{X}_1 \\ \mathbf{y} \end{bmatrix} + [CB]^{-1} \begin{bmatrix} \dot{y}_{d1} \\ \dot{y}_{d2} \end{bmatrix}, \end{aligned}$$

$$= H \begin{bmatrix} \mathbf{X}_1 \\ \mathbf{y} \end{bmatrix} + [CB]^{-1} \begin{bmatrix} \dot{y}_{d1} \\ \dot{y}_{d2} \end{bmatrix}, \quad (6.46)$$

$$\text{where, } H = [CB]^{-1} \begin{bmatrix} -R_{21} & -R_{22} \end{bmatrix} Q.$$

By using (6.12), \mathbf{u}_{eq} in terms of actual states are given as

$$\mathbf{u}_{\text{eq}} = H \begin{bmatrix} \mathbf{X}_1 \\ C_1 \mathbf{X}_1 + C_2 \mathbf{X}_2 \end{bmatrix} + [CB]^{-1} \begin{bmatrix} \dot{y}_{d1} \\ \dot{y}_{d2} \end{bmatrix},$$

The over-all control law becomes

$$\mathbf{u} = -M \text{sign}(\epsilon) + H \begin{bmatrix} \mathbf{X}_1 \\ C_1 \mathbf{X}_1 + C_2 \mathbf{X}_2 \end{bmatrix} + [CB]^{-1} \begin{bmatrix} \dot{y}_{d1} \\ \dot{y}_{d2} \end{bmatrix}, \quad (6.47)$$

$$\text{where, } H = \begin{bmatrix} 16.2 & 0.08 & 5.4 & -2.5 & -40.7 & 10.9 \\ 0 & 0 & 0 & 13.6 & 0 & -60.1 \end{bmatrix},$$

$$M = \begin{bmatrix} 0.5 & 0 \\ 0 & 0.7 \end{bmatrix}.$$

6.4.2 DSMC Implementation

Similarly, prior to implement the DSMC control law (6.26), the DSMC control law is derived as a function of the actual states, and given as

$$\mathbf{v} = -N \text{sign}(\varphi) - \Pi \begin{bmatrix} \mathbf{X}_1 \\ \mathbf{y} \end{bmatrix} - [CB]^{-1} (\Theta_3 \mathbf{u} + \Theta_4),$$

$$\begin{aligned} \text{where, } \Pi &= [CB]^{-1} \begin{bmatrix} \Theta_1 & \Theta_2 \end{bmatrix} Q, \\ &= \begin{bmatrix} \Pi_{11} & \Pi_{12} \\ \Pi_{21} & \Pi_{22} \end{bmatrix}. \end{aligned}$$

By using (6.15), the over-all control becomes

$$\mathbf{v} = -N \text{sign}(\varphi) - \Gamma \begin{bmatrix} \mathbf{X}_1 \\ \mathbf{X}_2 \end{bmatrix} - [CB]^{-1} (\Theta_3 \mathbf{u} + \Theta_4), \quad (6.48)$$

where,

$$\Gamma = \begin{bmatrix} \Pi_{11} + \Pi_{12}C_1 & \Pi_{12}C_2 \\ \Pi_{21} + \Pi_{22}C_1 & \Pi_{22}C_2 \end{bmatrix}, \quad (6.49)$$

$$= \begin{bmatrix} -0.23 & -0.09 & -0.07 & 0.03 & -0.28 & -0.03 \\ 0 & 0 & 0 & -0.19 & 0 & 0.14 \end{bmatrix},$$

$$\Theta_1 = \begin{bmatrix} 0.02 & 0 & 0.008 & 0 \\ 0 & 0 & -0.02 & \end{bmatrix}, \quad (6.50)$$

$$\Theta_2 = \begin{bmatrix} -0.07 & 0.002 \\ 0 & 0.07 \end{bmatrix}, \quad (6.51)$$

$$\Theta_3 = \begin{bmatrix} 0.01 & 0.003 \\ 0 & 0.06 \end{bmatrix}, \quad (6.52)$$

$$\Theta_4 = \begin{bmatrix} -1 & 0 & -0.1 & 0 \\ 0 & -1 & 0 & -0.3 \end{bmatrix}. \quad (6.53)$$

Moreover, the time derivative of the tracking error required in the sliding variable equation (6.23) is given as

$$\begin{aligned} \dot{\mathbf{e}} &= \dot{\mathbf{y}} - \dot{\mathbf{y}}_d = \alpha_{21} \mathbf{X}_1 + \alpha_{21} \mathbf{y} + CB\mathbf{u} - \dot{\mathbf{y}}_d, \\ &= (\alpha_{21} + \alpha_{22}C_1) \mathbf{X}_1 + \alpha_{22}C_2 \mathbf{X}_2 + CB\mathbf{u} - \dot{\mathbf{y}}_d. \end{aligned} \quad (6.54)$$

The control law is implemented by employing a finite difference method on (6.48) and (6.54), and the discretized controller is given as

$$\mathbf{u}(k) = \mathbf{u}(k-1) + dt \left(-N \text{sign}(\varphi) - \Gamma \begin{bmatrix} \mathbf{X}_1 \\ \mathbf{X}_2 \end{bmatrix} - [CB]^{-1} (\Theta_3 \mathbf{u} + \Theta_4) \right), \quad (6.55)$$

where, $N = \begin{bmatrix} 0.08 & 0 \\ 0 & 0.09 \end{bmatrix}$ and $dt = 1s$ is the sampling time.

6.5 Results and Discussions

In this section, the performance of H_∞ , SMC and DSMC have been compared and the simulation results are discussed in detail. Initially, the simulation runs in open loop configuration with the nominal inputs and the controller begins operation at 05th hour. Ideally, the controller should maximize the energy output per unit time by keeping both the outputs at their maximum allowed values. However, the peak values of heating value and flow rate drop due to the cavity growth in the UCG reactor. To compare the performance of the designed controllers, the desired trajectories of outputs are chosen in such a way that they also cover the operating points which lie outside the operating range of the linear model i.e. an extended operating range. Moreover, the capability of each controller to reject the disturbance is assessed by introducing an input disturbance around the 07th hour, as shown in Fig. 6.2. In UCG an optimal level of H₂O is required for the successful operation, while an excess water influx from surrounding strata reduces the temperature of a UCG reactor and disrupts its operation. The increase in water favors the endothermic steam gasification reaction and decreases the temperature of UCG reactor. Therefore, water influx from surrounding strata is considered as an input disturbance, as it increases the H₂O/O₂.

In Fig. 6.3, it is observed that all the designed controllers exhibit adequate performance in the presence of modeling inaccuracies and an input disturbance. The control inputs are shown in Fig. 6.4. It can be seen that the controllers maintain an optimal amount of H₂O by varying H₂O/O₂ to reject the input disturbance. The performance of each controller can be easily compared in the plot of tracking errors for the closed-loop operation, as shown in Fig. 6.5. When the controllers operate in the extended operating range, it is worth observing that the tracking error of H_∞ for the heating value of syngas increases. While there is no significant change in the tracking error of the syngas flow rate. This shows that the performance of H_∞ to reject the input disturbance deteriorates when it is operated outside the operating range of the linear model. Moreover, it can be seen that the tracking

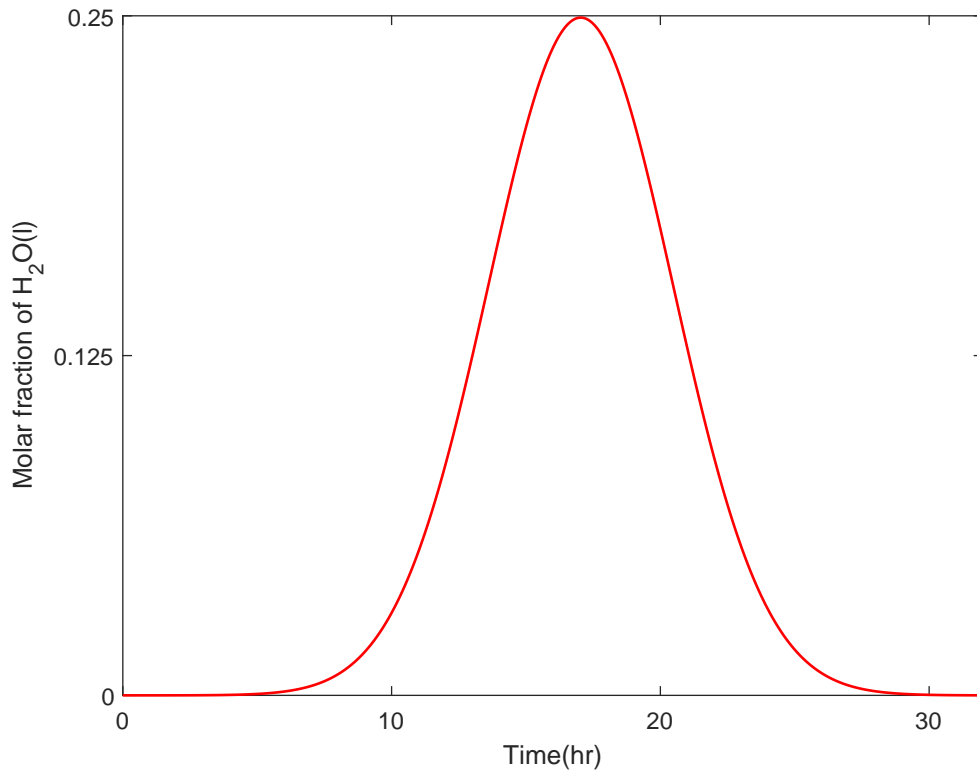


FIGURE 6.2: Input disturbance with time

errors of SMCs remain smaller than the H_∞ during the entire closed-loop operation. As the design of H_∞ completely depends on the linear model parameters, therefore, it is sensitive to the operating range. While in SMCs, the discontinuous inputs are not the functions of the linear model parameters, resulting in a better performance. However, the chattering is prominent in the conventional SMC as shown in Fig. 6.4. It is evident that the DSMC has reduced the chattering significantly due to continuous control inputs. Thus, the DSMC has achieved the desired control objectives by consuming less control efforts as compared to SMC.

A quantitative analysis is performed to compare the performance of SMC and DSMC. The performance of each controller is quantitatively evaluated by computing the root mean square error (RMSE), and given by

$$\text{RMSE} = \sqrt{\frac{1}{N_t} \sum_{n=1}^{N_t} e^2(i)}, \quad (6.56)$$

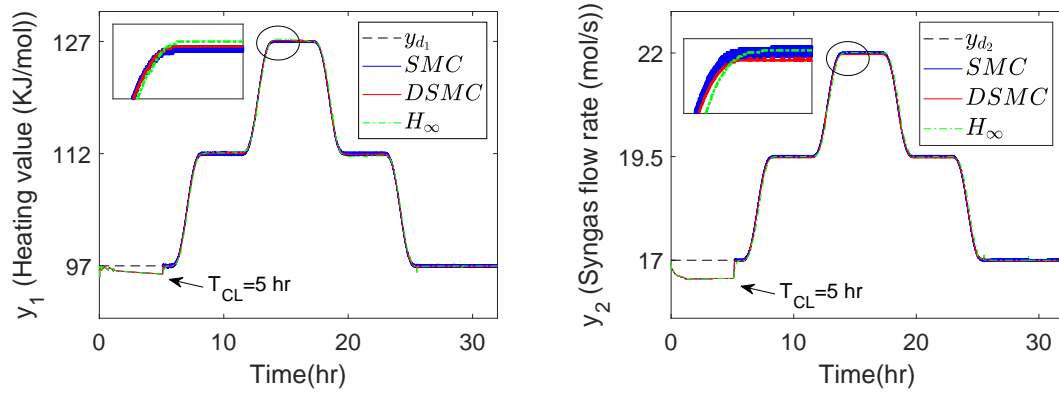


FIGURE 6.3: Outputs of the closed-loop system with time

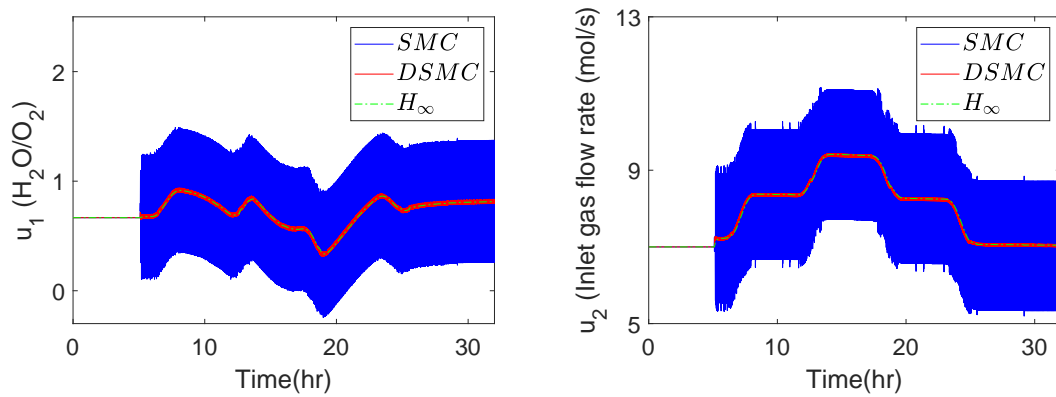


FIGURE 6.4: Control efforts with time

where N_t is the total number of samples. Since the control objectives are to maintain the heating value and flow rate of syngas at desired levels, the error function in RMSE is expressed as

$$\mathbf{e}(\mathbf{i}) = \mathbf{y}_i - \mathbf{y}_{d_i}. \quad (6.57)$$

The RMSE is computed for both the SMCs and summarized in Table 6.2. The tracking error of the heating value of syngas is the smallest for the DSMC design, while SMC performs slightly better than the DSMC for the flow rate of syngas. Although the performance of each controller is reasonably good, but SMC exhibits significant chattering. Thus, the reduction in chattering and continuous control inputs provided by the DSMC highlights its superiority over the SMC.

The time profile of sliding variable vector φ given in (6.23) is shown in Fig. 6.6. During the reaching phase i.e. $\varphi \neq 0$, the DSMC drags the outputs to to sliding

TABLE 6.2: Performance comparison of the SMCs

| Controllers | RMSE(%) | |
|-------------|---------|-------|
| | y_1 | y_2 |
| SMC | 11.0 | 2.1 |
| DSMC | 7.3 | 2.9 |

surface in the presence of modeling uncertainties and input disturbance. While in the sliding phase, the design of φ keeps the outputs to their desired levels. It is also observed that the sliding manifolds and errors remain in the close proximity of zero during the time when the controller is brought into operation.

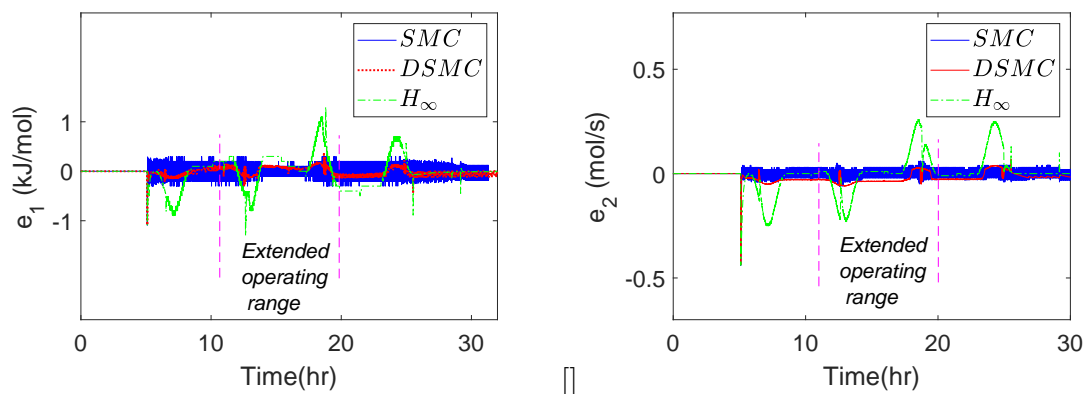


FIGURE 6.5: Tracking errors during closed-loop operation

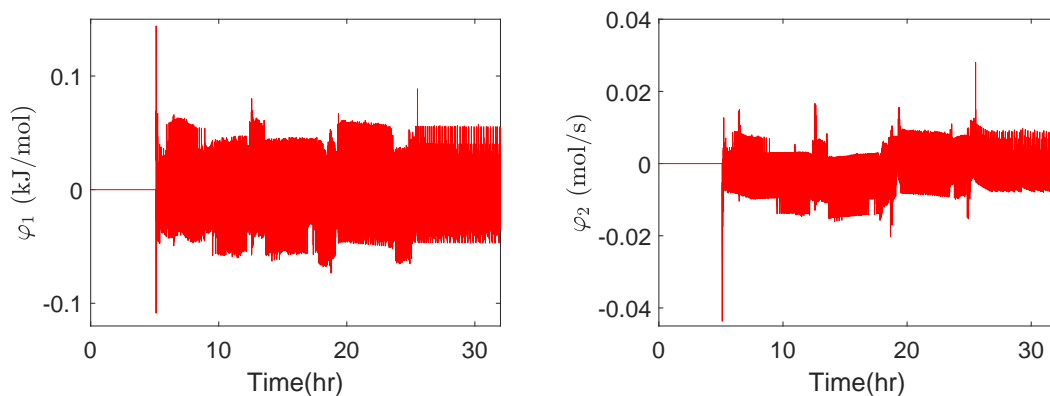


FIGURE 6.6: Sliding manifolds for DSMC

6.6 Summary

In this chapter, the linear model-based nonlinear robust control designs for the UPT have been presented. The regular form of the linear model is formulated to design the model-based conventional SMC and DSMC. Due to the complexity of CAVSIM, the zero dynamics stability is proved by formulating an approximate 1D packed bed model for the MIMO CAVSIM. Finally, the designed controllers are implemented on the CAVSIM, and the simulation results of H_∞ , SMC, and DSMC have been compared. The simulation results show that the performance of each controller is reasonably good in the presence of external disturbance and modeling inaccuracies. However, the performance of H_∞ is degraded in the extended operating range. Moreover, it has been observed that the DSMC utilizes lesser control energy to achieve the desired objectives, and it also reduces the chattering significantly due to the continuous control inputs.

Chapter 7

Conclusion and Future Work

In this chapter, the conclusion drawn from the research work carried out in this dissertation is summarized, and some of the future avenues are explored based on the current study.

7.1 Conclusion

The proposed research work highlights the challenges involved in the development of monitoring and control system for the UCG field. Each of the research contribution is concluded in the subsequent sections.

7.1.1 Cavity Prediction and Parametric Study

The simulation results of CAVSIM and 1D packed bed for the heating value and molar fraction of syngas species have been compared with the UPT field data. The results of CAVSIM have a small relative error as compared to 1D packed bed and show a good match with the field data. After model validation, the CAVSIM has been used to predict cavity growth at different stages of the UCG process. It has been found that the essential UCG phenomena like char production, water

influx and produced species flow rates and heating value of syngas are functions of cavity growth. It has also been observed that the lateral growth of the cavity determines the resource recovery of the process. Meanwhile, the vertical growth of the cavity predicts the hydrological and subsidence response of the overburden. Moreover, a sensitivity analysis on the volumetric cavity growth and heating value of the product gas has been performed to investigate the effect of various operating parameters like inlet gas composition and flow rate, O₂ concentration and steam to oxygen ratio. It has been concluded that the inlet gas with a mixture of O₂ and air is best suited to obtain the high cavity growth rate and heating value of the product gas. It has been noted that the heating value and cavity growth increase with the increase in the concentration of O₂ and the flow rate of inlet gas. Last but not the least, it has been concluded that an optimal value of steam to oxygen ratio is required to obtain the desired heating value of syngas. Hence, the presented model will help in determining and improving the performance of the UPT gasifier before the conduction of any field trial.

7.1.2 Development of a Control-oriented Model

The CAVSIM is a highly complex UCG model, and it can not be used directly to design the model-based control system for the UCG field. Thus, a simple linear multi-variable model has been identified to design model-based robust controllers for the UPT field. The N4SID system identification has been employed to estimate the multi-variable linear model for the UPT field, and the estimation data is generated by using the CAVSIM simulator. In the identification process, it has been found that the information about linear operating range and the parameters of a nonlinear plant such as delays, time constants, static gains and bandwidth is essential before the design of an identification experiment. These parameters have been found by performing staircase and step experiments. Moreover, it has been found that the type of input excitation signal, switching period, sampling time and experiment length are the critical parameters in the designing of an identification experiment. The model has been validated by using the simulation error and the

residual analysis methods. In the simulation error method, it has been observed that the model predictions have more than 90% best fit with the estimated data. Meanwhile, it has been observed that the auto-correlation of residuals of each output and the cross-correlation between output residuals and each input are within the confidence region in the residual analysis. Moreover, various aspects of the estimated model like interaction, uncertainty, and dynamic properties in time and frequency domains have been analyzed. For instance, it has been observed in the interactivity analysis that the identified model has less sensitivity to the input uncertainties and no RHP zero exists in the identified model. Similarly, the modeling uncertainties have been visualized by using the parameters confidence interval in the transient and frequency response of the identified model, and it has been found that the transition stage is more certain than the steady state. However, it has been noted that the values of uncertainties in steady state are low and the model also retains the fundamental dynamics of the actual process. Hence, the identified model has been employed to develop a model-based control for the UPT field.

7.1.3 Design of the Multi-variable Robust Control for the UPT Gasifier

In the current study, the significance of a multi-variable based closed loop system for the UCG field is highlighted. An H_∞ controller is designed using S/KS method, and the control problem is formulated by employing the standard H_∞ control configuration. The robust stability and performance analysis have been performed in the presence of model uncertainty. It is shown that the linear closed loop system meets all the desired transient requirements in the presence of input disturbance and modeling uncertainties. The robustness of controller has been assessed by implementing it on the CAVSIM, and it is shown that the outputs attain their desired values in the presence of an input disturbance and modeling inaccuracies.

The nonlinear SMCs have been also designed for the UPT field. The identified model is converted into the regular form to design SMC based nonlinear robust controllers. An approximated 1D model is also formulated for the MIMO CAVSIM,

and it has been shown that the zero dynamics of the model are stable with the designed controllers. Eventually, the designed controllers are implemented on the CAVSIM, and the performance of both the linear and nonlinear robust control techniques have been compared. The simulation results show that each controller has adequate performance and tracks the desired output trajectories. It is also observed that the performance of H_∞ degrades outside the operating range of the linear model. While the tracking errors of SMCs remain small along with the entire operating range. However, significant chattering is found in SMC, whereas DSMC has reduced the chattering due to continuous control inputs. DSMC utilizes lesser control energy to achieve the desired objectives.

7.2 Future Work

The presented research work can effectively contribute in exploring the potential research avenues in the field of UCG process, and some of which are discussed below.

7.2.1 Improvements in Field Trials

The cavity prediction analysis can be helpful in determining the critical economic and environmental factors of the UCG field trails. The lateral dimensions of the cavity determine the spacing between the inlet and outlet wells, while the upward growth of cavity provides information about the geological and hydrological subsidence behavior of the overburden. Thus, the resource recovery can be maximized, and the cavity collapse can be prevented by using the proposed analysis. It will also help in predicting the life of UCG reactor. Moreover, the insight provided by the parametric analysis can also be useful in the selection of operating parameters to improve the outcomes of the UPT field trails. Moreover, the electricity generation capacity of the UPT gasifier will be improved by the real time implementation of the proposed control system.

7.2.2 Improved Model-based Control Design for the UPT Gasifier

The model-based control design for the UPT gasifier can be improved, and the necessary steps are described as follows.

7.2.2.1 Formulation of First Principle UPT Model

The CAVSIM is a highly complex and accurate UCG model, but it can not be used directly for the model-based control system. Although, in this work a simple approximated control-oriented model of CAVSIM has been identified. As the identified model is not first principle based, and the states of this model have no physical meaning. Hence, the trade off lies in the prediction capabilities of the model and the model-based control design can be mitigated by formulating an approximated 2D PDEs based model. For this purpose, the prediction capabilities of the 1D packed bed model described in section 6.3 can be improved by incorporating the following phenomena.

- The energy and mass balances can be formulated in 2D or 3D.
- The cavity growth phenomena can be incorporated by submodels of wall and roof.
- The water influx from the surrounding strata can be modeled by including the two mechanisms i.e. gravity drainage and pressurizing the coal seam.

7.2.2.2 Parameter Estimation

As it has been seen in chapter 3 that the volumetric cavity growth and the heating value of syngas is a function of the operating parameters and the coal bed properties of the UCG process. As the process occurs in-situ, and most of the process parameters are not possible to measure. Moreover, the installation of such a

monitoring system is in itself a challenging task. Thus, the parameters estimation techniques can be employed to estimate the unknown parameters of the process, and it will help in the control design. The parameters of coal and surrounding strata like density, permeability, and porosity of coal, permeability of ash, coal and rock and thermal coefficients can be estimated. While the unknown parameters of the cavity like temperature, recession rate and water influx can be estimated.

7.2.2.3 Implementation at the UCG Field

Finally, the model-based control system with an estimator design can be implemented at the actual site to improve the performance of the UCG field.

Bibliography

- [1] M. Blinderman and A. Klimenko, “Introduction to underground coal gasification and combustion,” in *Underground Coal Gasification and Combustion*. Elsevier, 2018, pp. 1–8. [Online]. Available: <https://doi.org/10.1016%2Fb978-0-08-100313-8.00001-3>
- [2] *Key World Energy Statistics 2020*. OECD, Sep 2020. [Online]. Available: <https://doi.org/10.1787%2F295f00f5-en>
- [3] *World Energy Outlook 2019*. OECD, Nov 2019. [Online]. Available: <https://doi.org/10.1787%2Fcaf32f3b-en>
- [4] C. Descamps, C. Bouallou, and M. Kanniche, “Efficiency of an integrated gasification combined cycle (IGCC) power plant including CO₂ removal,” *Energy*, vol. 33, no. 6, pp. 874–881, Jun 2008. [Online]. Available: <https://doi.org/10.1016%2Fj.energy.2007.07.013>
- [5] A. W. Bhutto and S. Karim, “Coal gasification for sustainable development of the energy sector in pakistan,” *Energy for Sustainable Development*, vol. 9, no. 4, pp. 60–67, Dec 2005. [Online]. Available: <https://doi.org/10.1016%2Fs0973-0826%2808%2960500-1>
- [6] B. P. Company, *BP Statistical Review of World Energy 2019*, 68th ed., 2019.
- [7] N. V. Gnanapragasam, B. V. Reddy, and M. A. Rosen, “Hydrogen production from coal gasification for effective downstream CO₂ capture,” *International Journal of Hydrogen Energy*, vol. 35, no. 10, pp. 4933–4943,

- May 2010. [Online]. Available: <https://doi.org/10.1016%2Fj.ijhydene.2009.07.114>
- [8] D. A. Bell, B. F. Towler, and M. Fan, “Chapter 5 - underground coal gasification,” in *Coal Gasification and Its Applications*, D. A. Bell, B. F. Towler, and M. Fan, Eds. Boston: William Andrew Publishing, 2011, pp. 101–111. [Online]. Available: <https://www.sciencedirect.com/science/article/pii/B9780815520498100051>
- [9] G. Perkins, “Mathematical modelling of underground coal gasification,” Ph.D. dissertation, The University of New South Wales, Australia, 2005.
- [10] G. Perkins and V. Sahajwalla, “Steady-state model for estimating gas production from underground coal gasification,” *Energy & Fuels*, vol. 22, no. 6, pp. 3902–3914, Sep 2008. [Online]. Available: <https://doi.org/10.1021%2Fef8001444>
- [11] E. Shafirovich and A. Varma, “Underground coal gasification: A brief review of current status,” *Industrial & Engineering Chemistry Research*, vol. 48, no. 17, pp. 7865–7875, Sep 2009. [Online]. Available: <https://doi.org/10.1021%2Fie801569r>
- [12] Z. Luo and M. Agraniotis, *Low-Rank Coals for Power Generation, Fuel and Chemical Production*. Woodhead Publishing, 2017. [Online]. Available: <https://doi.org/10.1016%2Fb978-0-08-100895-9.00029-2>
- [13] D. W. Camp, “A review of underground coal gasification research and development in the united states,” Department of Energy Office of Scientific and Technical Information (OSTI), USA, Tech. Rep., Jun 2017. [Online]. Available: <https://doi.org/10.2172%2F1368032>
- [14] K. Stańczyk, N. Howaniec, A. Smoliński, J. Świądrowski, K. Kapusta, M. Wiatowski, J. Grabowski, and J. Rogut, “Gasification of lignite and hard coal with air and oxygen enriched air in a pilot scale ex situ reactor for underground gasification,” *Fuel*, vol. 90, no. 5, pp. 1953–1962, May 2011. [Online]. Available: <https://doi.org/10.1016%2Fj.fuel.2010.12.007>

- [15] G. Perkins, “Underground coal gasification – part i: Field demonstrations and process performance,” *Progress in Energy and Combustion Science*, vol. 67, pp. 158–187, Jul 2018. [Online]. Available: <https://doi.org/10.1016%2Fj.pecs.2018.02.004>
- [16] G. R. Couch, “Underground coal gasification,” IEA Clean Coal Centre, London (United Kingdom), Tech. Rep. CCC-151, Jul 2009.
- [17] M. S. Blinderman, D. N. Saulov, and A. Y. Klimenko, “Forward and reverse combustion linking in underground coal gasification,” *Energy*, vol. 33, no. 3, pp. 446–454, Mar 2008. [Online]. Available: <https://doi.org/10.1016%2Fj.energy.2007.10.004>
- [18] D. W. Gregg and T. F. Edgar, “Underground coal gasification,” *AIChE Journal*, vol. 24, no. 5, pp. 753–781, Sep 1978. [Online]. Available: <https://doi.org/10.1002%2Faic.690240502>
- [19] A. A. Uppal, “Modeling and control of underground coal gasification,” Ph.D. dissertation, COMSATS Institute of Information Technology, Islamabad, Pakistan, 2016.
- [20] A. Jowkar, F. Sereshki, and M. Najafi, “A new model for evaluation of cavity shape and volume during underground coal gasification process,” *Energy*, vol. 148, pp. 756–765, Apr 2018. [Online]. Available: <https://doi.org/10.1016%2Fj.energy.2018.01.188>
- [21] C. B. Thorsness and J. A. Britten, “Lawrence livermore national laboratory underground coal gasification project:final report,” Lawrence Livermore National Laboratory, CA (USA), UCID-21853, Tech. Rep., 1989.
- [22] —, “Lawrence livermore national laboratory underground coal gasification project: Final report,” Lawrence Livermore National Laboratory, CA (USA), Tech. Rep. UCID-21853, 1989.

- [23] ———, “CAVISM user manual,” Department of Energy Office of Scientific and Technical Information (OSTI), USA, Tech. Rep., Mar 1989. [Online]. Available: <https://doi.org/10.2172%2F6307133>
- [24] G. Samdani, P. Aghalayam, A. Ganesh, and S. Mahajani, “A process model for underground coal gasification – part-III: Parametric studies and UCG process performance,” *Fuel*, vol. 234, pp. 392–405, Dec 2018. [Online]. Available: <https://doi.org/10.1016%2Fj.fuel.2018.07.011>
- [25] G. Samdani, P. Aghalayam, A. Ganesh, R. Sapru, B. Lohar, and S. Mahajani, “A process model for underground coal gasification – part-I: Cavity growth,” *Fuel*, vol. 181, pp. 690–703, Oct 2016. [Online]. Available: <https://doi.org/10.1016%2Fj.fuel.2016.05.020>
- [26] A. Y. Klimenko, “Early developments and inventions in underground coal gasification,” in *Underground Coal Gasification and Combustion*. Elsevier, 2018, pp. 11–24. [Online]. Available: <https://doi.org/10.1016%2Fb978-0-08-100313-8.00002-5>
- [27] Y. Xiao, J. Yin, Y. Hu, J. Wang, H. Yin, and H. Qi, “Monitoring and control in underground coal gasification: Current research status and future perspective,” *Sustainability*, vol. 11, no. 1, p. 217, Jan 2019. [Online]. Available: <https://doi.org/10.3390%2Fsu11010217>
- [28] D. J. Roddy and P. L. Younger, “Underground coal gasification with CCS: a pathway to decarbonising industry,” *Energy & Environmental Science*, vol. 3, no. 4, p. 400, 2010. [Online]. Available: <https://doi.org/10.1039%2Fb921197g>
- [29] V. Sarhosis, K. Kapusta, and S. Lavis, “Underground coal gasification (UCG) in europe: Field trials, laboratory experiments, and EU-funded projects,” in *Underground Coal Gasification and Combustion*. Elsevier, 2018, pp. 129–171. [Online]. Available: <https://doi.org/10.1016%2Fb978-0-08-100313-8.00005-0>

- [30] M. S. Blinderman, "Global development of commercial underground coal gasification," *IOP Conference Series: Earth and Environmental Science*, vol. 76, p. 012003, Jul 2017. [Online]. Available: <https://doi.org/10.1088%2F1755-1315%2F76%2F1%2F012003>
- [31] E. A. W. Finance Division Government of Pakistan Islamabad, "Pakistan economic survey 2018-19," http://www.finance.gov.pk/survey/chapters_19/14-Energy.pdf, 2019.
- [32] A. Mahmood, N. Javaid, A. Zafar, R. A. Riaz, S. Ahmed, and S. Razzaq, "Pakistan's overall energy potential assessment, comparison of lng, tapi and ipi gas projects," *Renewable and sustainable energy reviews*, vol. 31, pp. 182–193, 2014.
- [33] D. Government of Pakistan Planning Commission, Ministry of Planning and S. Initiatives, "Annual plan 2020-21," <http://https://www.pc.gov.pk/uploads/annualplan/AnnualPlan2020-21.pdf>, 2019.
- [34] P. Sindh Coal & Energy Department, Government of Sindh, "Thar coal fields technical specification, block-v," <http://www.sindhcoal.gos.pk/coal-fields/thar-coalfield/>, 2012.
- [35] M. Van der Riet, "Underground coal gasification," in *Proceedings of the SAIEE Generation Conference. Eskom College, Midrand, Nagoya, Japan*, Feb. 2008.
- [36] I. Khurshid, M. A. S. Baig, and J. Choe, "Utilization of coal deposits of thar colliers with underground coal gasification, opportunities and challenges in syngas generation," in *SPE/PAPG Annual Technical Conference*. Society of Petroleum Engineers, 2013. [Online]. Available: <https://doi.org/10.2118%2F169642-ms>
- [37] A. A. Memon, S. A. Shaikh, H. Mahar, M. Uqaili, S. Hussain, A. Palari, and T. Ashraf, "Underground coal gasification and utilization of syngas in various fields," *Journal of Faculty of Engineering & Technology*, vol. 23, no. 1, pp. 75–85, 2016.

- [38] M. Imran, D. Kumar, N. Kumar, A. Qayyum, A. Saeed, and M. S. Bhatti, “Environmental concerns of underground coal gasification,” *Renewable and Sustainable Energy Reviews*, vol. 31, pp. 600–610, Mar 2014. [Online]. Available: <https://doi.org/10.1016%2Fj.rser.2013.12.024>
- [39] V. Prabu and S. Jayanti, “Simulation of cavity formation in underground coal gasification using bore hole combustion experiments,” *Energy*, vol. 36, no. 10, pp. 5854–5864, Oct 2011. [Online]. Available: <https://doi.org/10.1016%2Fj.energy.2011.08.037>
- [40] C. B. Thorsness and J. A. Britten, “A model for cavity growth and resource recovery during underground coal gasification,” Lawrence Livermore National Laboratory, CA (USA), Tech. Rep. UCRL-99987, 1988.
- [41] M. Khan, J. Mmbaga, A. Shirazi, J. Trivedi, Q. Liu, and R. Gupta, “Modelling underground coal gasification—a review,” *Energies*, vol. 8, no. 11, pp. 12 603–12 668, Nov 2015. [Online]. Available: <https://doi.org/10.3390%2Fen81112331>
- [42] A. W. Bhutto, A. A. Bazmi, and G. Zahedi, “Underground coal gasification: From fundamentals to applications,” *Progress in Energy and Combustion Science*, vol. 39, no. 1, pp. 189–214, Feb 2013. [Online]. Available: <https://doi.org/10.1016%2Fj.pecs.2012.09.004>
- [43] D. Yeary and J. Riggs, “Study of small-scale cavity growth mechanisms for ucg,” *In Situ;(United States)*, vol. 11, no. 4, Jan 1987.
- [44] S. Daggupati, R. N. Mandapati, S. M. Mahajani, A. Ganesh, D. Mathur, R. Sharma, and P. Aghalayam, “Laboratory studies on combustion cavity growth in lignite coal blocks in the context of underground coal gasification,” *Energy*, vol. 35, no. 6, pp. 2374–2386, Jun 2010. [Online]. Available: <https://doi.org/10.1016%2Fj.energy.2010.02.015>
- [45] L. YANG, “Study on the method of two-phase underground coal gasification with unfixed pumping points,” *Energy Sources*, vol. 25, no. 9,

- pp. 917–930, Sep 2003. [Online]. Available: <https://doi.org/10.1080%2F00908310390225945>
- [46] G. Perkins, “Underground coal gasification – part II: Fundamental phenomena and modeling,” *Progress in Energy and Combustion Science*, vol. 67, pp. 234–274, Jul 2018. [Online]. Available: <https://doi.org/10.1016%2Fj.pecs.2018.03.002>
- [47] R. D. Gunn and D. L. Whitman, “In situ coal gasification model (forward mode) for feasibility studies and design,” Bureau of Mines, Laramie, Laramie Energy Research Center, Wyo, USA, Tech. Rep. LERC/RI-76/2, 1976.
- [48] C. B. Thorsness and R. B. Rozsa, “In-situ coal gasification: Model calculations and laboratory experiments,” *Society of Petroleum Engineers Journal*, vol. 18, no. 02, pp. 105–116, Apr 1978. [Online]. Available: <https://doi.org/10.2118%2F6182-pa>
- [49] C. B. Thorsness, E. A. Grens, and A. Sherwood, “One-dimensional model for in situ coal gasification,” Lawrence Livermore National Laboratory, CA (USA), Tech. Rep. UCRL-52523, 1978.
- [50] A. Winslow, “Numerical model of coal gasification in a packed bed,” *Symposium (International) on Combustion*, vol. 16, no. 1, pp. 503–513, Jan 1977. [Online]. Available: <https://doi.org/10.1016%2Fs0082-0784%2877%2980347-0>
- [51] C. B. Thorsness and S. W. Kang, “General-purpose, packed-bed model for analysis of underground coal gasification processes,” Lawrence Livermore National Lab., CA (USA), Tech. Rep., 1986.
- [52] E. A. A. Abdel-Hadi and T. R. Hsu, “Computer modeling of fixed bed underground coal gasification using the permeation method,” *Journal of Energy Resources Technology*, vol. 109, no. 1, pp. 11–20, Mar 1987. [Online]. Available: <https://doi.org/10.1115%2F1.3231316>

- [53] A. N. Khadse, M. Qayyumi, S. M. Mahajani, and P. Aghalayam, “Reactor model for the underground coal gasification (UCG) channel,” *International Journal of Chemical Reactor Engineering*, vol. 4, no. 1, Nov 2006. [Online]. Available: <https://doi.org/10.2202%2F1542-6580.1351>
- [54] A. A. Uppal, A. I. Bhatti, E. Aamir, R. Samar, and S. A. Khan, “Control oriented modeling and optimization of one dimensional packed bed model of underground coal gasification,” *Journal of Process Control*, vol. 24, no. 1, pp. 269–277, Jan 2014. [Online]. Available: <https://doi.org/10.1016%2Fj.jprocont.2013.12.001>
- [55] —, “Optimization and control of one dimensional packed bed model of underground coal gasification,” *Journal of Process Control*, vol. 35, pp. 11–20, Nov 2015. [Online]. Available: <https://doi.org/10.1016%2Fj.jprocont.2015.08.002>
- [56] T. H. T. Tsang, “Modeling of heat and mass transfer during coal block gasification,” Ph.D. dissertation, University of Texas at Austi, USA, 1981.
- [57] J. G. Massaquoi and J. B. Riggs, “Mathematical modeling of combustion and gasification of a wet coal slab—I,” *Chemical Engineering Science*, vol. 38, no. 10, pp. 1747–1756, 1983. [Online]. Available: <https://doi.org/10.1016%2F0009-2509%2883%2985031-3>
- [58] —, “Mathematical modeling of combustion and gasification of a wet coal slab—II,” *Chemical Engineering Science*, vol. 38, no. 10, pp. 1757–1766, 1983. [Online]. Available: <https://doi.org/10.1016%2F0009-2509%2883%2985032-5>
- [59] K. Y. Park and T. F. Edgar, “Modeling of early cavity growth for underground coal gasification,” *Industrial & Engineering Chemistry Research*, vol. 26, no. 2, pp. 237–246, Feb 1987. [Online]. Available: <https://doi.org/10.1021%2Fie00062a011>
- [60] G. Perkins and V. Sahajwalla, “A mathematical model for the chemical reaction of a semi-infinite block of coal in underground coal gasification,”

- Energy & Fuels*, vol. 19, no. 4, pp. 1679–1692, Jul 2005. [Online]. Available: <https://doi.org/10.1021%2Fef0496808>
- [61] —, “A numerical study of the effects of operating conditions and coal properties on cavity growth in underground coal gasification,” *Energy & Fuels*, vol. 20, no. 2, pp. 596–608, Mar 2006. [Online]. Available: <https://doi.org/10.1021%2Fef050242q>
- [62] C. Magnani and S. F. Ali, “Mathematical modeling of the stream method of underground coal gasification,” *Society of Petroleum Engineers Journal*, vol. 15, no. 05, pp. 425–436, Oct 1975. [Online]. Available: <https://doi.org/10.2118%2F4996-pa>
- [63] C. F. Magnani and S. F. Ali, “A two-dimensional mathematical model of the underground coal gasification process,” in *Fall Meeting of the Society of Petroleum Engineers of AIME*. Society of Petroleum Engineers, 1975. [Online]. Available: <https://doi.org/10.2118%2F5653-ms>
- [64] M. Pasha, “An advanced numerical model of underground coal gasification by the stream method, using simultaneous solution,” in *SPE Annual Fall Technical Conference and Exhibition*. Society of Petroleum Engineers, 1978. [Online]. Available: <https://doi.org/10.2118%2F7416-ms>
- [65] B. Dinsmoor, J. Galland, and T. Edgar, “The modeling of cavity formation during underground coal gasification,” *Journal of Petroleum Technology*, vol. 30, no. 05, pp. 695–704, May 1978. [Online]. Available: <https://doi.org/10.2118%2F6185-pa>
- [66] R. A. Kuyper, “Transport phenomena in underground coal gasification channels: Transportverschijnselen in ondergrondse kolenvergassingskanalen,” Ph.D. dissertation, Delft University of Technology, Netherlands, 1994.
- [67] G. Perkins and V. Sahajwalla, “Steady-state model for estimating gas production from underground coal gasification,” *Energy & Fuels*, vol. 22, no. 6, pp. 3902–3914, Nov 2008. [Online]. Available: <https://doi.org/10.1021%2Fef8001444>

- [68] M. Seifi, J. Abedi, and Z. Chen, “The analytical modeling of underground coal gasification through the application of a channel method,” *Energy Sources, Part A: Recovery, Utilization, and Environmental Effects*, vol. 35, no. 18, pp. 1717–1727, Sep 2013. [Online]. Available: <https://doi.org/10.1080%2F15567036.2010.531501>
- [69] D. Vanbatenburg and J. Bruining, “The efficiency of filtration gasification,” *IN SITU*, vol. 17, no. 4, pp. 413–437, 1993.
- [70] E. Biezen, J. Bruining, and J. Molenaar, “An integrated 3d model for underground coal gasification,” in *SPE Annual Technical Conference and Exhibition*. Society of Petroleum Engineers, 1995. [Online]. Available: <https://doi.org/10.2118%2F30790-ms>
- [71] C. B. Thorsness and J. A. Britten, “Further development of an axisymmetric global ucg cavity growth simulator,” Lawrence Livermore National Laboratory, CA (USA), Tech. Rep. UCRL-96461, 1987.
- [72] —, “A mechanistic model for axisymmetric ucg cavity growth,” Lawrence Livermore National Laboratory, CA (USA), Tech. Rep. UCRL-94419, 1986.
- [73] A. G. Edward and C. B. Thorsness, “Unconfined flow as a mechanism of water influx to a ucg system,” Lawrence Livermore National Laboratory, CA (USA), Tech. Rep. UCRL-97203, 1987.
- [74] E. A. Grens and C. B. Thorsness, “Wall recession rates in underground cavity growth modeling,” Lawrence Livermore National Laboratory, CA (USA), Tech. Rep. UCRL-90729, 1985.
- [75] —, “The effect of nonuniform bed properties on cavity wall recession,” Lawrence Livermore National Laboratory, CA (USA), Tech. Rep. UCRL-92487, 1986.
- [76] —, “Modeling thermal and material interactions between a reacting char bed and a gasifying/spalling coal roof,” Lawrence Livermore National Laboratory, CA (USA), Tech. Rep. UCRL-92488, 1986.

- [77] J. Nitao, T. Buscheck, S. M. Ezzedine, S. J. Friedmann, and D. W. Camp, “An integrated 3d ucg model for predicting cavity growth, product gas and interactions with the host environment,” Lawrence Livermore National Laboratory, CA (USA), Tech. Rep. CONF-459611, 2017.
- [78] J. J. Nitao, D. W. Camp, T. A. Buscheck, J. A. White, G. C. Burton, J. L. Wagoner, and M. Chen, “Progress on a new integrated 3-d ucg simulator and its initial application,” Lawrence Livermore National Laboratory, CA (USA), Tech. Rep. CONF-500551, 2011.
- [79] C. B. Thorsness and S. W. Kang, “Further development of a general-purpose, packed-bed model for analysis of underground coal gasification processes,” Lawrence Livermore National Laboratory, CA (USA), Tech. Rep. UCRL-92489, 1985.
- [80] T. L. Eddy and S. H. Schwartz, “A side wall burn model for cavity growth in underground coal gasification,” *Journal of Energy Resources Technology*, vol. 105, no. 2, pp. 145–155, Jun 1983. [Online]. Available: <https://doi.org/10.1115%2F1.3230894>
- [81] R. Kuyper, T. V. D. Meer, and C. Hoogendoorn, “Turbulent natural convection flow due to combined buoyancy forces during underground gasification of thin coal layers,” *Chemical Engineering Science*, vol. 49, no. 6, pp. 851–861, 1994. [Online]. Available: <https://doi.org/10.1016%2F0009-2509%2894%2980022-7>
- [82] D. Van Batenburg, “95/03476 a new channel model for underground gasification of thin, deep coal seams,” *Fuel and Energy Abstracts*, vol. 36, no. 4, p. 254, Jul 1995. [Online]. Available: <https://doi.org/10.1016%2F0140-6701%2895%2995130-w>
- [83] P. Pirlot, J. Pirard, A. Coeme, and M. Mostade, “99/01679 a coupling of chemical processes and flow in view of the cavity growth simulation of an underground coal gasifier at great depth,” *Fuel and*

- Energy Abstracts*, vol. 40, no. 2, p. 167, Mar 1999. [Online]. Available: <https://doi.org/10.1016%2Fs0140-6701%2899%2996860-1>
- [84] Y. Luo, M. Coertzen, and S. Dumble, “Comparison of ucg cavity growth with cfd model predictions,” in *7th International Conference on CFD in the Minerals and Process Industries CRISO*, Melbourne, Australia, Dec. 2009.
- [85] G. Samdani, P. Aghalayam, A. Ganesh, R. Sapru, B. Lohar, and S. Mahajani, “A process model for underground coal gasification – part-II growth of outflow channel,” *Fuel*, vol. 181, pp. 587–599, Oct 2016. [Online]. Available: <https://doi.org/10.1016%2Fj.fuel.2016.05.017>
- [86] H. Akbarzadeh and R. J. Chalaturnyk, “Sequentially coupled flow-geomechanical modeling of underground coal gasification for a three-dimensional problem,” *Mitigation and Adaptation Strategies for Global Change*, vol. 21, no. 4, pp. 577–594, Jun 2016. [Online]. Available: <https://doi.org/10.1007%2Fs11027-014-9583-2>
- [87] S. B. Javed, A. A. Uppal, A. I. Bhatti, and R. Samar, “Prediction and parametric analysis of cavity growth for the underground coal gasification project thar,” *Energy*, vol. 172, pp. 1277–1290, Apr 2019. [Online]. Available: <https://doi.org/10.1016%2Fj.energy.2019.02.005>
- [88] J. Kacur, P. Flegner, M. Durdán, and M. Laciak, “Model predictive control of ucg: An experiment and simulation study,” *Information Technology and Control*, Dec 2019. [Online]. Available: <https://doi.org/10.5755/j01.itc.48.4.23303>
- [89] K. Kostur and J. Kacur, “Development of control and monitoring system of UCG by promotiv,” in *2011 12th International Carpathian Control Conference (ICCC)*. IEEE, May 2011. [Online]. Available: <https://doi.org/10.1109%2Fcarpathiancc.2011.5945850>
- [90] K. Kostúr and J. Kačúr, “The monitoring and control of underground coal gasification in laboratory conditions,” *Acta Montanistica Slovaca*, vol. 13, no. 1, pp. 111–117, 2008.

- [91] Instrument society of America Research Triangle Park, NC, 1995.
- [92] K. Kostúr and J. Kačur, “Extremum seeking control of carbon monoxide concentration in underground coal gasification,” *IFAC-PapersOnLine*, vol. 50, no. 1, pp. 13 772–13 777, Jul 2017. [Online]. Available: <https://doi.org/10.1016%2Fj.ifacol.2017.08.2571>
- [93] A. M. Chaudhry, A. A. Uppal, Y. M. Alsmadi, A. I. Bhatti, and V. I. Utkin, “Robust multi-objective control design for underground coal gasification energy conversion process,” *International Journal of Control*, vol. 93, no. 2, pp. 328–335, Sep 2018. [Online]. Available: <https://doi.org/10.1080%2F00207179.2018.1516893>
- [94] A. Arshad, A. I. Bhatti, R. Samar, Q. Ahmed, and E. Aamir, “Model development of UCG and calorific value maintenance via sliding mode control,” in *2012 International Conference on Emerging Technologies*. IEEE, Oct 2012. [Online]. Available: <https://doi.org/10.1109%2Ficet.2012.6375477>
- [95] “Chapter 1: Theory of classical sliding mode control,” in *Advanced and Optimization Based Sliding Mode Control: Theory and Applications*. Society for Industrial and Applied Mathematics, Jan 2019, pp. 3–32. [Online]. Available: <https://doi.org/10.1137%2F1.9781611975840.ch1>
- [96] A. A. Uppal, Y. M. Alsmadi, V. I. Utkin, A. I. Bhatti, and S. A. Khan, “Sliding mode control of underground coal gasification energy conversion process,” *IEEE Transactions on Control Systems Technology*, vol. 26, no. 2, pp. 587–598, Mar 2018. [Online]. Available: <https://doi.org/10.1109%2Ftcst.2017.2692718>
- [97] A. A. Uppal, S. S. Butt, A. I. Bhatti, and H. Aschemann, “Integral sliding mode control and gain-scheduled modified utkin observer for an underground coal gasification energy conversion process,” in *2018 23rd International Conference on Methods & Models in Automation & Robotics (MMAR)*. IEEE, Aug 2018. [Online]. Available: <https://doi.org/10.1109%2Fmmar.2018.8486053>

- [98] A. A. Uppal, S. S. Butt, Q. Khan, and H. Aschemann, “Robust tracking of the heating value in an underground coal gasification process using dynamic integral sliding mode control and a gain-scheduled modified utkin observer,” *Journal of Process Control*, vol. 73, pp. 113–122, Jan 2019. [Online]. Available: <https://doi.org/10.1016%2Fj.jprocont.2018.11.005>
- [99] S. Mei and Y. Ismail, “Stable parallelizable model order reduction for circuits with frequency-dependent elements,” *IEEE Transactions on Circuits and Systems I: Regular Papers*, vol. 56, no. 6, pp. 1214–1220, Jun 2009. [Online]. Available: <https://doi.org/10.1109%2Ftcsi.2008.2008508>
- [100] M. Najafi, S. M. E. Jalali, R. KhaloKakaie, and F. Forouhandeh, “Prediction of cavity growth rate during underground coal gasification using multiple regression analysis,” *International Journal of Coal Science & Technology*, vol. 2, no. 4, pp. 318–324, 2015.
- [101] S. Daggupati, R. N. Mandapati, S. M. Mahajani, A. Ganesh, A. Pal, R. Sharma, and P. Aghalayam, “Compartment modeling for flow characterization of underground coal gasification cavity,” *Industrial & Engineering Chemistry Research*, vol. 50, no. 1, pp. 277–290, 2010.
- [102] C. B. Thorsness and S. W. Kang, “A method-of-line approach to solution of packed-bed flow problems related to underground coal gasification processes,” Lawrence Livermore National Laboratory, CA (USA), Tech. Rep., 1984.
- [103] M. Field, D. Gill, and W. Hawksley, *Combustion of pulverized coal*. Cheney & Sons Ltd., 1967.
- [104] R. Govind and J. Shah, “Modeling and simulation of an entrained flow coal gasifier,” *AIChE Journal*, vol. 30, no. 1, pp. 79–92, 1984.
- [105] J. Bear, *Dynamics of Fluids in Porous Media*. American Elsevier, New York, Ch.8, 1972.

- [106] A. C. Hindmarsh, "Lsode and lsodi, two new initial value ordinary differential equation solvers," *ACM Signum Newsletter*, vol. 15, no. 4, pp. 10–11, 1980.
- [107] C. G. Broyden, "A class of methods for solving nonlinear simultaneous equations," *Mathematics of computation*, vol. 19, no. 92, pp. 577–593, 1965.
- [108] G. EUROPE, "Gas 3100 r coal gas/syngas 19-3u analyser," *Gas Engineering and Instrumentation Technologies Europe, Bunsbeek, Belgium*, 2011.
- [109] O. G. Oyugi, B. Gathitu, and H. Ndiritu, "A review on the effect of feed oxygen, water concentration, temperature and pressure on gasification proce," in *Proceedings of Sustainable Research and Innovation Conference*, Sep. 2017, pp. 134–139.
- [110] A. Hamanaka, F.-q. Su, K.-i. Itakura, K. Takahashi, J.-i. Kodama, and G. Deguchi, "Effect of injection flow rate on product gas quality in underground coal gasification (ucg) based on laboratory scale experiment: development of co-axial ucg system," *Energies*, vol. 10, no. 2, p. 238, 2017.
- [111] L. Ljung, "Perspectives on system identification," *IFAC Proceedings Volumes*, vol. 41, no. 2, pp. 7172–7184, 2008. [Online]. Available: <https://doi.org/10.3182%2F20080706-5-kr-1001.01215>
- [112] R. Ghosh, "Input designs for identification of ill-conditioned multivariable systems," Ph.D. dissertation, Åbo Akademi-Åbo Akademi University, Åbo/-Turku, Finland, 2016.
- [113] L. Ljung, *System Identification Theory for the User*. Switzerland: Prentice Hall PTR, 1999.
- [114] A. I. Bhatti, "Advanced sliding mode controllers for industrial applications," Ph.D. dissertation, University of Leicester, London, 1998.
- [115] R. Pintelon and J. Schoukens, *System identification: a frequency domain approach*. John Wiley & Sons, 2012.

- [116] H. Hjalmarsson, “System identification of complex and structured systems,” in *2009 European Control Conference (ECC)*. IEEE, Aug 2009. [Online]. Available: <https://doi.org/10.23919%2Fecc.2009.7074935>
- [117] S. Gaikwad and D. Rivera, “Control-relevant input signal design for multivariable system identification: Application to high-purity distillation,” *IFAC Proceedings Volumes*, vol. 29, no. 1, pp. 6143–6148, Jun 1996. [Online]. Available: <https://doi.org/10.1016%2Fs1474-6670%2817%2958666-8>
- [118] D. Rivera, S. Gaikwad, and X. Chen, “CONTROL-ID: a demonstration prototype for control-relevant identification,” in *Proceedings of 1994 American Control Conference - ACC '94*. IEEE. [Online]. Available: <https://doi.org/10.1109%2Facc.1994.752438>
- [119] R. P. Pothukuchi and J. Torrellas, “A guide to design mimo controllers for architectures,” University of Illinois at Urbana-Champaign, Tech. Rep., Apr 2016.
- [120] S. Skogestad and I. Postlethwaite, *Multivariable feedback control: analysis and design*. Wiley New York, 2007, vol. 2.
- [121] D.-W. Gu, P. Petkov, and M. M. Konstantinov, *Robust control design with MATLAB®*. Springer Science & Business Media, 2005.
- [122] S. Ghabraei, H. Moradi, and G. Vossoughi, “Design & application of adaptive variable structure & h_∞ robust optimal schemes in nonlinear control of boiler-turbine unit in the presence of various uncertainties,” *Energy*, vol. 142, pp. 1040–1056, Jan 2018. [Online]. Available: <https://doi.org/10.1016%2Fj.energy.2017.10.089>
- [123] S. J. Gambhire, D. R. Kishore, P. S. Londhe, and S. N. Pawar, “Review of sliding mode based control techniques for control system applications,” *International Journal of Dynamics and Control*, May 2020. [Online]. Available: <https://doi.org/10.1007%2Fs40435-020-00638-7>

-
- [124] M. Steinberger, M. Horn, and L. Fridman, Eds., *Variable-Structure Systems and Sliding-Mode Control*. Springer International Publishing, 2020. [Online]. Available: <https://doi.org/10.1007%2F978-3-030-36621-6>
- [125] V. Utkin, A. Poznyak, Y. V. Orlov, and A. Polyakov, *Road Map for Sliding Mode Control Design*. Springer, 2020.
- [126] V. Utkin, “Sliding mode control,” in *Variable Structure Systems: from principles to implementation*. IET, pp. 3–18. [Online]. Available: https://doi.org/10.1049%2Fpbce066e_ch1
- [127] A. A. Agrachev, A. S. Morse, E. D. Sontag, H. J. Sussmann, and V. I. Utkin, *Nonlinear and optimal control theory: lectures given at the CIME Summer School held in Cetraro, Italy, June 19-29, 2004*. Springer Science & Business Media, 2008, vol. 1932.
- [128] M. Krstic and A. Smyshlyaev, *Boundary Control of PDEs*. Society for Industrial and Applied Mathematics, Jan 2008. [Online]. Available: <https://doi.org/10.1137%2F1.9780898718607>